A study in computational fluid dynamics for the determination of convective heat and vapour transfer coefficients

Adam Neale

A thesis

in

The Department

of

Building, Civil and Environmental Engineering

Presented in Partial Fulfillment of the Requirements

for the Degree of Master in Applied Science at

Concordia University

Montreal, Quebec, Canada

August 2006

Your file Votre référence
ISBN: 978-0-494-28889-4
Our file Notre référence
ISBN: 978-0-494-28889-4

ABSTRACT

A study in computational fluid dynamics for the determination of convective heat and vapour transfer coefficients.

Adam Neale, M.A.Sc.

Convective heat and moisture transfer coefficients are required to simulate the performance of building envelope systems, for example, in the simulation of the drying of wood or brick cladding wetted by driving rain. Such coefficients are dependent on the velocity and type of the air flow, the air and material temperature, the moisture content of the material and the relative humidity of the air. Convective heat transfer coefficient correlations are readily available for many geometries and air flow conditions, but primarily for mechanical engineering applications. It is not so for convective mass transfer coefficients. Building physicists must often put up with values from literature that are not entirely adequate or perform measurements for the conditions under study.

The overall goal of this work was to study the feasibility and accuracy of using computational fluid dynamics (CFD) to calculate convective heat and vapour transfer coefficients. The objectives were:

- to validate the CFD simulation results for boundary layer velocity and temperature profiles for laminar and turbulent forced convection, and for turbulent natural convection;
- to simulate vapor transfer between air and a porous material; and
- to compare the calculated convective heat and vapor transfer coefficients with literature experimental data.

Several CFD simulations were performed to calculate the boundary layer velocity and temperature profiles in different configurations. The calculated convective heat transfer coefficients were compared with analytical, semi-empirical and/or experimental results from literature. A grid sensitivity analysis was performed to determine the grid independent solutions for certain cases. The overall conclusion was that CFD accurately predicted the boundary layer velocity and temperature profiles and the convective heat transfer coefficients for the cases studied.

In order to simulate vapour transfer between air and porous materials, a model was developed using CFD coupled with an external vapour transport model. CFD was used to model heat and water vapour transport in the air, including both convective and radiative heat transfer, and heat transport within the material. Vapour transport in the material was calculated externally and coupled with the CFD solution at specific time steps. A transient case of air flow over a drying wood sample was simulated using the developed model. A sensitivity analysis was performed on relevant model parameters, such as the material properties of the wood and flow conditions of the air layer.

ACKNOWLEDGEMENTS

My first set of thanks would have to go to the professor that taught me my first building engineering class. Her class was really what made me realize that building engineering is the field of study for me. Coincidentally, it was the same professor that taught me building envelope design, where I came to realize what my field of interest would be. Finally, it was the same professor who suggested I consider doing a Masters and ended up being my supervisor. I owe a great deal of thanks to Dominique Derome, who is an inspirational teacher that has motivated me to do my best for the six years that I have known her. Thank you!

During the course of my thesis I spent five months as a tourist in Belgium, where I spent most of my time with the locals working on computational fluid dynamics. It all started when one day I was working on a simulation in Montreal and having some problems, and someone suggested that I hop on a plane and go to Leuven for half a year. Two weeks later I was there. The credit for that brilliant idea goes entirely to Bert Blocken, though none of us really expected it to turn out quite that well I think. It turns out that core concepts of CFD are far more easily communicated in person than via e-mail. None of the simulations contained in this thesis would have been possible for me without the help of Bert, and I am truly grateful for all the coaching he has given me.

On the subject of Leuven, I must sincerely thank the people that allowed me to visit their department for such an extended period of time. I felt very welcome in Belgium, and the people there have a way of inspiring good work. In particular I would like to thank Jan Carmeliet for his help modelling vapour diffusion (and other things), and Hans Janssen for his help with my control volume algorithm. Hans also provided me with shelter when there was a fire in my apartment building and I was left homeless for two weeks.

Finally, I must extend my thanks to my friends, simply for being there when I need them and putting up with my random departures to other countries. Of course, my family is last but certainly not the least. My parents and my brother are ever-supporting entities in my existence, and I think I need not say more (they know the rest).

TABLE OF CONTENTS

LIST OF FIGURES

LIST OF TABLES

NOMENCLATURE

Roman Symbols		Units
a	Distance in the x-direction	m
A	Cross-sectional area	m^2
b	Distance in the y-direction	m
C	Coefficient matrix	n/a
C_1 to C_6	Equation coefficients	n/a
C_p	Specific heat	J/kg-K
d	Momentum boundary layer thickness	m
d_h	Thermal boundary layer thickness	m
d_m	Vapour boundary layer thickness	m
D_{eff}	Effective vapour diffusivity	m^2/s
D_H	Hydraulic diameter	m
g	Gravitational acceleration	m/s^2
G	Mass flux	kg/s
Gr	Grashov number	n/a
h_c	Convective heat transfer coefficient	W/m^2K
h_m	Convective vapour transfer coefficient	s/m
h_R	Radiative heat transfer coefficient	W/m^2K
H	Height	m
i	Element number in the x-direction	n/a
j	Element number in the y-direction	n/a
k	Thermal conductivity	W/m-K
k	Turbulent kinetic energy	m^2/s^2
L	Length scale	m
Le	Lewis number	n/a
$\dot{m}$	Mass flow rate	kg/s
Nu	Nusselt number	n/a
p_v	Vapour pressure	Pa
p_{vsat}	Saturation vapour pressure	Pa
P	Heated perimeter	m
Pr	Prandtl number	n/a

Pr_t	Turbulent Prandtl number	n/a
q	Heat flux	W/m^2
Q	Heat flow	W
Ra	Rayleigh number	n/a
Re	Reynolds number	n/a
Sc	Schmidt number	n/a
t	Time scale	s
T	Temperature	K
T^+	Dimensionless temperature	n/a
T^*	Dimensionless temperature	n/a
u	X-component of velocity	m/s
u^*	Friction velocity	m/s
u^+	Dimensionless velocity	n/a
u'	Moisture concentration	kg/kg
U	Instantaneous velocity	m/s
v	Y-component of velocity	m/s
V_0	Buoyancy velocity	m/s
w	Moisture content	kg/m^3
X	Dimensionless length in the x-direction	n/a
X'	Mass fraction	kg/kg
y^+	Dimensionless distance	n/a
Y	Dimensionless length in the y-direction	n/a

Greek Symbols		Units
α	Thermal diffusivity	m^2/s
β	Thermal expansion coefficient	K^{-1}
δ	Vapour permeability	s
ε	Radiative emissivity	n/a
ε	Turbulence dissipation rate	m^2/s^3
ε_h^d	Discretization error	*
ϕ	Relative humidity	n/a
ϕ_h	Finest mesh solution	*
Φ	Grid independent solution	*

κ	von Karman Constant	n/a
μ	Dynamic viscosity	kg/m-s
μ_t	Dynamic turbulent viscosity	kg/m-s
ν	Kinematic viscosity	m^2/s
θ	Temperature	K
ρ	Density	kg/m^3
σ	Stefan-Boltzmann constant	W/m^2K^4
τ_w	Wall shear stress	Pa
ω	Specific dissipation rate	s^{-1}
ξ	Slope of the wood sorption curve	kg/m^3

* Units depend on parameter studied.

Subscripts

b	Bulk
f	Fluid reference
i	Counter
L	Length scale
ref	Reference
s	Surface
t	Turbulent quantity
w	Wall

Superscripts

$t+\Delta t$	Quantity evaluated at the subsequent timestep

Operators

div	Divergence operator
∇^2	Laplacian operator

CHAPTER 1. INTRODUCTION

1.1. PROBLEM STATEMENT

Convective heat and vapour transfer coefficients, also referred to as surface coefficients, are required to simulate the hygrothermal performance of building envelope systems, for example, in the simulation of the drying of wood or brick cladding wetted by driving rain. Such coefficients can theoretically depend on the following variables: velocity and type of the air flow, material temperature, reference temperature of the air, reference relative humidity of the air, porosity at the surface of the material, and moisture content of the material. Convective heat transfer coefficient correlations are readily available for many geometries and air flow conditions. However, when practitioners refer to codes, standards and handbooks for values of convective heat transfer coefficients, the values provided are often not entirely adequate for their particular case of study. Building physicists face the same problem and must often perform experiments to determine surface coefficients applicable to their particular problem.

The information available for the determination of convective vapour transfer coefficients is even more limited even though it has long been a subject of study. Chilton and Colburn (1934) first estimated that the boundary layers were similar for heat and moisture flows and proposed an equivalence relation between the heat and mass surface coefficients, which has since been labelled the Chilton-Colburn analogy. Their results, which were later confirmed by Lewis (1970), are used extensively in literature. However, the Chilton-Colburn analogy was developed for particular circumstances and was then being applied for different situations. Many authors have reported values inconsistent with the analogy (e.g. Masmoudi and Prat 1990, Wadsö 1993, Derome 1999, Hukka and Oksanen 1999, Salin 2003, etc.). For example, in flows above unsaturated porous materials such as wood, overestimation of the mass transfer coefficient can reach 300% (Derome 1999).

In terms of experimentally derived surface coefficients, literature provides some data despite the difficulties involved in experimentally determining convective vapour transfer coefficients. Experimental techniques previously used moisture content gradients, gravimetric samples or relative humidity of air to indirectly measure mass flow. More recent techniques such as Particle Image Velocimetry or Laser Interferometry are expensive but allow for accurate boundary layer velocity profiling. Not all testing facilities can afford such equipment, and therefore the accuracy of experimental results

is often questionable for a parameter that is so highly dependent on the boundary layer air flow.

In summary, the coupled heat and vapour transfer processes within the boundary layer are not yet fully understood. Furthermore, current building physics problems may include radiative exchanges or sources of heat and moisture. The omission of these factors can also result in discrepancies in the determination of the surface coefficients.

As a consequence of the difficulties associated with experimentally measuring surface coefficients and the inadequacy of existing analogies linking convective heat and vapour coefficients, it is desired to find another method to accurately determine convective surface coefficients for general conditions seen in buildings. Computer modelling is a far newer field than coupled heat and vapour transport in the boundary layer, and consequently there has been limited computer modelling work dedicated to this area of research. Different methods are available to simulate heat and vapour transport, and computer modelling, when properly validated, can prove to be a flexible tool for calculating convective heat and vapour transfer coefficients for different conditions. Thus, the focus of this research was on computer modelling used for the purpose of calculating surface coefficients.

1.2. Scope of the Work

The overall goal of this work was to study the feasibility and accuracy of using computational fluid dynamics (CFD) to calculate convective heat and vapour transfer coefficients for conditions required in hygrothermal studies of building envelopes. Specifically, the CFD commercial software *Fluent 6.2.16* was selected to be used for all simulations. The determination of surface coefficients requires the proper resolution of boundary layer profiles, and CFD has been shown in the past to properly resolve air flow for a multitude of problems. In addition, CFD also has the capability to model heat transfer within solid and fluid materials, though the vapour transport models are generally limited to fluid regions. Due to these reasons, CFD was selected as the computer modelling tool for this research.

There were several objectives related to calculating the convective heat and vapour transfer coefficients with CFD. First, it was desired to validate the boundary layer velocity and temperature profiles calculated with CFD for enough different flow conditions to ensure the accuracy of the models within *Fluent*. Laminar forced convection, turbulent forced convection, and turbulent natural convection were selected

as the primary flow conditions to be studied. Laminar natural convection was not chosen as a part of the scope of the research, nor was combined forced and natural convection.

The second objective was to simulate vapour transfer between air and a porous material. Due to certain limitations in the CFD software that was used, a separate computer model was developed to complete the requirements for coupled heat and vapour transport.

Finally, the third objective was to compare the calculated convective heat and vapour transfer coefficients with literature experimental data, correlations and other computer model data.

Due to the extensive computer modelling required to complete the three objectives stated above, experimental work was not included in the scope of the research. Sufficient experimental data and analytical results were found in literature for validation.

1.3. METHODOLOGY

CFD simulations were performed to calculate the boundary layer velocity and temperature profiles for a number of flow conditions. Depending on the nature of the air flow, the calculated convective heat transfer coefficients were compared with analytical, semi-empirical and/or experimental results from literature. For example, the laminar forced convection simulations were compared with analytical solutions for the convective heat transfer coefficients. The turbulent forced convection boundary layer velocity and temperature profiles were compared with semi-empirical equations based on both analytical solutions and experimental data. The natural convection simulation data was compared to velocity and temperature profiles taken from experimental data from literature. A grid sensitivity analysis was performed and the grid independent solutions were determined for certain cases. Once CFD had been proven to resolve heat transport for a variety of flow conditions and cases with sufficient accuracy, the next step was to use CFD to solve vapour transport between air and porous materials.

In order to simulate vapour transfer between air and porous materials, a model was developed using CFD coupled with an external vapour transport model. CFD was used to model heat and water vapour transport in the air, including both convective and radiative heat transfer, and heat transport within the material. Vapour transport in the material was calculated externally and coupled with the CFD solution at specific time steps. A transient case of air flow over a drying wood sample was simulated using the

developed model. The calculated convective vapour transfer coefficients were compared to experimentally determined values and coefficients calculated from the Chilton-Colburn analogy.

1.4. OUTLINE

Chapter 2 is a review of the literature related to the subject of this research. Some general theory related to relevant subjects is included to clarify parts of the thesis or to provide a background for the methodology of the research. In addition, some key terms that are used extensively throughout the thesis are defined.

Chapter 3 describes the simulations and results for laminar forced convection. The concept of a reference temperature for convective heat transfer coefficients is defined. The validation method for the simulations is described and results are presented. The concept of a grid sensitivity analysis is introduced and executed for the laminar forced convection cases.

In Chapter 4, the results for the turbulent forced convection are presented. Near-wall modelling is introduced in this chapter and put into context for the cases studied. The validation method is explained and the results for the turbulent forced convection simulations are analyzed.

In Chapter 5, the turbulent natural convection simulations are described. The particular problems associated with performing natural convection simulations using CFD are explained. Experimental natural convection data are presented and used for validation of the simulations.

Chapter 6 contains the theory and other relevant information for the coupled heat and vapour transfer model developed for this research. The model results are presented and qualitatively compared with experimental data.

Chapter 7 contains general conclusions and recommendations for future work.

CHAPTER 2. LITERATURE REVIEW

This chapter represents the state of the art and a literature review concerning convective heat and vapour transfer coefficients and computational fluid dynamics. Firstly, convective surface coefficients will be outlined in Section 2.1 with some general theory provided to accompany the later chapters. Convective heat and vapour transfer coefficients are defined, and the difficulties associated with experimental and analytical determination are explained. Second, Section 2.2 defines forced and natural convection, and previous works involving CFD and these topics are outlined. Numerical modelling and computational fluid dynamics are described in Section 2.3, in addition to the governing equations for fluid flow and general information on turbulence modelling. Finally, Section 2.4 explains coupled heat and vapour transfer and provides some examples of modelling and experimental work performed in that field of research.

2.1. SURFACE COEFFICIENTS

Convective heat transfer can be defined as the heat exchange mechanism caused by fluid flow over a surface (Hutcheon and Handegord 1995). Similarly, convective vapour transfer would be the vapour exchange mechanism resulting from fluid flow over a surface. Both transfer processes are analogous, and the magnitude of the heat or vapour transferred due to convection is generally expressed by means of surface coefficients. The convective heat and vapour transfer coefficients are defined in Sections 2.1.1 and 2.1.2, respectively.

2.1.1. CONVECTIVE HEAT TRANSFER COEFFICIENT

Heat transfer is generally defined as having three major transfer processes: conduction, convection and radiation (Kreith and Bohn 2001). While the topic of this thesis is related primarily to convection, it will be shown that conduction and radiation play a very important role in defining convection. Consequently, conduction and radiation must be defined before convection can be properly discussed.

Fourier's law of heat conduction is well accepted as the defining relationship for conductive heat transfer within a material (Hutcheon and Handegord 1995):

$$Q = -kA\frac{\partial T}{\partial x} \tag{2.1}$$

where Q is the heat flux in the x-direction (W), k is the thermal conductivity of the material (W/m-K), A is the area perpendicular to the heat transfer (m^2), and $(\partial T/\partial x)$ is the temperature gradient within the material in the x-direction (K/m) (Kreith and Bohn 2001).

Radiative heat transfer can be defined in its simplest form as the following:

$$Q_R = A_1 \varepsilon_1 \sigma \left(T_1^4 - T_2^4\right) \tag{2.2}$$

where Q_R is the heat radiated from Body 1 to Body 2 (W), A_1 is the area of the body emitting the heat (m^2), ε_1 is the emissivity of Body 1 (dimensionless), σ is the Stefan-Boltzmann constant (=5.67x10^{-8} W/m^{2}K^4), T_1 is the temperature of Body 1 (K), and T_2 is the temperature of Body 2 (K). Other parameters such as view factors may be introduced to reduce the magnitude of heat transferred (Kreith and Bohn 2001). Radiation is also often expressed in terms of a radiative heat transfer coefficient, defined as:

$$h_R = \frac{\varepsilon \sigma \left(T_1^4 - T_2^4\right)}{\left(T_1 - T_2\right)} \tag{2.3}$$

where h_R is the radiative heat transfer coefficient (W/m^{2}K). An example of an application using h_R would be to combine the effects of solar radiation and convective heat transfer into one film coefficient for outdoor heat transfer. The importance of h_R for the scope of this thesis will become evident once convective heat transfer is defined.

When considering a fluid flowing over a surface and heat is exchanged, virtually any heat transfer textbook will define the convective heat transfer in the following manner (see e.g. Kreith and Bohn 2001):

$$q = -k \left.\frac{\partial T}{\partial y}\right|_{y=0} = h_c \left(T_s - T_f\right) \tag{2.4}$$

where q is the heat flux per unit area (W/m^2), k is the thermal conductivity of the fluid (W/m-K), (∂T/∂y) is the temperature gradient at the surface (K/m), h_c is the convective heat transfer coefficient (W/m^{2}K), T_s is the surface temperature (K) and T_f is the fluid reference temperature.

The Nusselt number is a commonly used dimensionless parameter that is defined as the ratio of convection heat transfer to conduction heat transfer for a given reference length. In equation form, the Nusselt number can be expressed as:

$$Nu_L = \frac{h_c L}{k} \tag{2.5}$$

where Nu_L is the Nusselt number, and L is the reference length (m). The Nusselt number is often used to correlate experimental data for convective heat transfer.

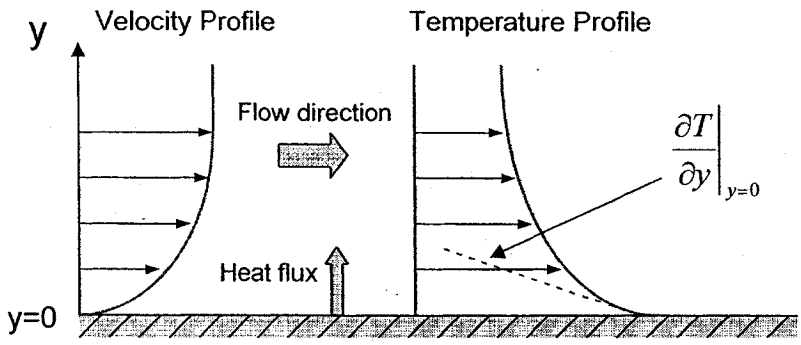

Figure 2.1. Velocity and temperature profiles for convective heat transfer

Figure 2.1 illustrates the convective heat transfer process defined in Equation 2.4 (adapted from Kreith and Bohn, 2001). For now, the exact shape of the velocity and temperature profiles are not considered (refer to Section 2.2 for more information). Fluid in contact with a surface (i.e. at y = 0 in Figure 2.1) has a zero velocity component (no-slip condition) and therefore is assumed to behave via conduction and not convection within that infinitesimally thin layer. Therefore, an energy balance at that location would generally result in Equation 2.4 governing the heat transfer. However, if radiation is also present, an energy balance would show that Equation 2.4 is no longer applicable and that the convective heat transfer coefficient must be combined with the radiative heat transfer coefficient. The result is aptly named the combined heat transfer coefficient, which is usually defined by the following relationship:

$$h = h_c + h_R \tag{2.6}$$

The effect of radiation on the convective heat transfer will be shown to be an important factor later in the coupled heat and vapour transfer section. Before the two processes may be discussed in combination, convective vapour transfer must be defined.

2.1.2. *Convective Vapour Transfer Coefficient*

Vapour transport is considered to be an analogous process to heat transfer for both conduction (i.e. vapour diffusion) and convection. The analogue to Fourier's law of heat conduction for vapour can be expressed with the following equation:

$$G = -\delta A \frac{\partial p_v}{\partial x} \tag{2.7}$$

where G is the mass flux (kg/s), δ is the vapour permeability of the medium (s, or ng/[m^{2}sPa] in Canada), A is the area perpendicular to the flux (m^2), $(\partial p_v / \partial x)$ is the vapour pressure gradient within the transport medium in the x-direction (Pa/m). Vapour permeability is a material property similar to thermal conductivity that is dependent on temperature. For example, at 20 °C the vapour permeability of air is approximately 1.95×10^{-10} seconds. The vapour pressure is also a temperature dependent property, which will become important when considering combined heat and vapour transport.

Unlike the thermal diffusion equation that is always in terms of a temperature gradient, Equation 2.7 can be expressed in terms of a number of different driving potentials. Since water vapour can be considered an ideal gas for most applications, Equation 2.7 can be transformed to be in terms of vapour concentration, mass fraction, relative humidity, capillary pressure, and a number of other driving potentials. Derivations are available in most heat and mass transfer textbooks.

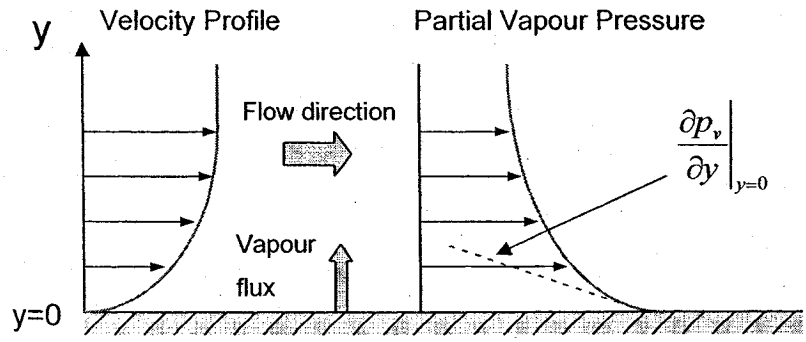

Figure 2.2. Velocity and partial vapour pressure profiles for convective vapour transfer

The convective vapour transfer process illustrated in Figure 2.2 can be defined using an analogous equation to the one presented earlier for heat transfer in Equation 2.4:

$$g = -\delta \left.\frac{\partial p_v}{\partial y}\right|_{y=0} = h_m \left(p_{vs} - p_{vf}\right) \tag{2.8}$$

where g is the mass flux per unit area (kg/m^{2}s), δ is the vapour permeability of the material (s), $(\partial p_v / \partial y)$ is the vapour pressure gradient in the y-direction (Pa/m), p_{vs} and p_{vf} are, respectively, the partial vapour pressure for the surface and the fluid reference vapour pressure (Pa), and h_m is the convective vapour transfer coefficient, which in this case is derived with vapour pressure as the driving potential (s/m).

2.1.3. *Experimental Determination of Surface Coefficients*

Experimental determination of convective heat transfer coefficients is, by nature, easier to accomplish than for vapour transfer. This is primarily due to the fact that instruments exist, such as thermocouples, which measure temperature quite accurately at virtually any location in an experiment. Other methods, such as infrared thermography, can determine the temperature distribution for an entire surface in a completely non-intrusive way. Regrettably, there are no equivalent sensors or equipment for vapour transport quantities. For example, in order to measure partial vapour pressure, both the temperature and the relative humidity must be measured at a given point, and the vapour pressure calculated based upon the data. While this is a feasible method for air (depending on the experiment), determining the partial vapour pressure for the surface of a material is significantly more complex. In order to shed some light on experimental techniques that determine the convective heat and vapour transfer coefficients, this section will focus on experiments described in literature, starting with convective heat transfer.

Experiments designed to determine heat transfer coefficients can often be divided into two categories: 1) specific applications and 2) general data. An experiment designed for a specific application would include, for example, experimentally determined heat transfer coefficients for natural convection in window cavities (Gustavsen 2001). An example from this category would be when De Paepe *et al* (2005) performed experiments on full-scale heat exchangers with the intent to verify correlations developed for a variety of heat exchanger fin types. The results were presented in the form of a correlation and were compared to previous experimental work with good agreement.

An example of an experiment under the "general data" category would be the experiment performed by Tian and Karayiannis (2000), which focused entirely on turbulent natural convection. The focus of their work was to provide an experiment that could be used as a benchmark for CFD model validation. Consequently, a high degree of accuracy in their measurements (particularly within the boundary layer) was considered most important. Instead of having a direct practical application such as the experiment by De Paepe *et al*, the data from the Tian and Karayiannis experiment could be applied in a more general fashion to a number of applications.

Despite the difficulty in experimentally determining convective vapour transfer coefficients, some work has been done in this area. Combined heat and vapour

transport has not been defined in this thesis yet, and therefore only isothermal experiments designed to measure convective vapour transfer will be described here.

An experimental setup called the Transient Moisture Transfer (TMT) facility developed at the University of Saskatchewan is used to determine convective mass transfer coefficients (Olutimayin and Simonson 2004). The experimental set-up is designed to be used for isothermal and non-isothermal experiments for air flowing over a given material. However, the same limitations mentioned earlier for measuring moisture quantities in materials apply. Also, there is limited information provided regarding the nature of the flow over the material surface and/or boundary layer air flow measurements.

Tremblay *et al* (2000) provides a table summarizing convective vapour transfer coefficients from a variety of sources, both experimental and empirical, for a number of different driving potentials. The values shown in Table 2.1 are a testament to the variability seen in literature for the convective vapour transfer coefficients.

Table 2.1. Surface coefficients from literature (taken from Tremblay *et al* 2000)

Authors	h_m	Driving Force	h_c	Drying conditions	Origin
Ferguson and Turner (1994)	0.02 m/s	Molar fraction of vap.	20 W/m^{2}K	$T_{d.b.}$ 120-180 °C, $T_{w.b.}$ 80 °C, v_{air} 6 m/s	
Sutherland *et al* (1992)	0.02 m/s	Vapour density kg/m^3	17 W/m^{2}K	$T_{d.b.}$ 90 °C, $T_{w.b.}$ 70 °C, v_{air} 3 m/s	
	0.02 m/s		17 W/m^{2}K	$T_{d.b.}$ 125 °C, $T_{w.b.}$ 70 °C, v_{air} 3 m/s	h_h: Salin (1988)
	0.04 m/s	Vapour pressure Pa	32 W/m^{2}K	$T_{d.b.}$ 122 °C, $T_{w.b.}$ 70 °C, v_{air} 8 m/s	h_m: Analogy from h_h
	0.04 m/s		32 W/m^{2}K	$T_{d.b.}$ 152 °C, $T_{w.b.}$ 67 °C, v_{air} 8 m/s	
Stanish *et al* (1986)			58 W/m^{2}K	$T_{d.b.}$ 75 °C, v_{air} 7 m/s	
			29 W/m^{2}K	$T_{d.b.}$ 125 °C, v_{air} 2 m/s	
Kawai *et al* (1978)	0.943 x 10^{-6} g/cm^{2}s-mmHg	Vapour pressure mmHg		$T_{d.b.}$ 40 °C	experiments
Bonneau and Puiggali (1993)	0.0313 m/s	Vapour concentration kg/kg$_{humid\ air}$	33 W/m^{2}K	$T_{d.b.}$ 49 °C, $T_{w.b.}$ 38 °C	

Table 2.1 (Cont'd). Surface coefficients from literature (taken from Tremblay *et al* 2000)

Authors	h_m	Driving Force	h_c	Drying conditions	Origin
Cloutier *et al* (1992)	9.36×10^{-10} kg^2/m^2s-J	Water potential J/kg		$T_{d.b.}$ 40 °C, $T_{w.b.}$ 42.5 °C, v_{air} 1 m/s	Experiments
Thomas *et al* (1980)	2.5×10^{-6} Kg/m^2s-°M	Moisture potential °M	22.5 W/m²K	$T_{d.b.}$ 110 °C, $T_{w.b.}$ 87 °C	Keylworth (1952)
Liu and Cheng (1989)	2.5×10^{-6} Kg/m^2s-°M	Moisture potential °M	22.5 W/m²K	$T_{d.b.}$ 110 °C	Thomas *et al* (1980)
Irudayaraj *et al* (1990)	1.67×10^{-6} Kg/m^2s-°M	Moisture potential °M	22.5 W/m²K	$T_{d.b.}$ 60 °C	Thomas *et al* (1980)
	1.67×10^{-6} Kg/m^2s-°M	Moisture potential °M	22.5 W/m²K	$T_{d.b.}$ 121 °C	Beard *et al* (1983)
Gui *et al* (1994)	2.4×10^{-6} to 9.4×10^{-6} Kg/m^2s-°M	Moisture potential °M	61.4 to 0.5 W/m²K	$T_{d.b.}$ 110 °C, $T_{w.b.}$ 87 °C	
	0.1×10^{-5} to 4.0×10^{-5} Kg/m^2s-°M	Moisture potential °M		$T_{d.b.}$ 115.6 °C, $T_{w.b.}$ 71.1 °C	
Perré (1987)	0.02 m/s	Vapour density kg/m^3	15 W/m²K	$T_{d.b.}$ 80 °C, $T_{w.b.}$ 68 °C, v_{air} 2 m/s	h_h: Moyne (1982)
	0.02 m/s	Vapour density kg/m^3	23 W/m²K	$T_{d.b.}$ 80 °C, $T_{w.b.}$ 68 °C, v_{air} 5 m/s	h_m: analogy from h_h
Ben Nasrallah and Perré (1988)	0.02 m/s	Vapour density kg/m^3	23 W/m²K	$T_{d.b.}$ 80 °C, $T_{w.b.}$ 68 °C	
Perré and Maillet (1989)	0.014 m/s	Vapour density kg/m^3	14 W/m²K	$T_{d.b.}$ 50 °C, $T_{w.b.}$ 30 °C	
	0.014 m/s	Vapour density kg/m^3	14 W/m²K	$T_{d.b.}$ 120 °C, $T_{w.b.}$ 80 °C	
	0.025 m/s	Vapour density kg/m^3	25 W/m²K	$T_{d.b.}$ 60 °C, $T_{w.b.}$ 30 °C	
Perré and Degiovanni (1990)	0.014 m/s	Molar fraction of vap.	14 W/m²K	$T_{d.b.}$ 50 °C, $T_{w.b.}$ 30 °C	h_m: analogy from h_h
	0.014 m/s	Molar fraction of vap.	14 W/m²K	$T_{d.b.}$ 120 °C, $T_{w.b.}$ 80 °C	

2.2. CONVECTION PROCESSES

Convection has been defined as the heat or vapour transfer due to a fluid moving over a surface. There are two general categories of convection: forced convection and natural convection. Combined forced and natural convection exists (it is also called mixed convection), but is not within the scope of this research project.

Figure 2.1 of the previous section illustrates that the convective heat transfer process involves a fluid moving over a surface and that heat is exchanged due to the temperature difference. In simpler terms, the velocity and temperature gradients directly result in convective heat transfer; both gradients must be present for heat to be transferred via convection. If the fluid is stationary, the heat transfer process will be entirely due to conduction and/or radiation, and, if the temperature gradient is zero, there is simply no heat transferred. The shape of the velocity profile will be determined largely by the nature of the flow, which can generally be divided into two categories: laminar and turbulent flow. There is a transition region also, but it is not treated within the scope of this thesis. The description of laminar and turbulent flows will differ for forced and natural convection.

2.2.1. FORCED CONVECTION

Forced convection is the heat transfer process resulting from a fluid being driven by an outside force over a body. Examples of forced convection include air flow resulting from mechanical ventilation, wind, pressure differences due to stack effect, and many others. Forced convection can also result from a body moving through a fluid, but in general the principles remain the same.

Forced convection, as a principle, is easy to describe but not as easily defined mathematically or solved analytically. Lienhard and Lienhard (2006) summarize the problems associated with forced convection as follows:

> *"If the fluid properties vary significantly with temperature, we cannot predict the velocity without knowing the temperature, and vice versa. The problems of predicting velocity and temperature become intertwined and harder to solve.*
>
> *Either the fluid flow solution or the temperature solution can, itself, become prohibitively hard to find. When that happens, we resort to the correlation of experimental data with the help of dimensional analysis."*

The statement by Lienhard and Lienhard is also applicable to natural convection. Luckily, the material properties for air do not vary significantly for the range of temperatures found in the cases studied during this research. However, the flow conditions (and, according to Lienhard and Lienhard, the temperature conditions) can become complex given a sufficiently high level of turbulence. In order to describe the

regime of a particular flow, be it laminar, transitional, or turbulent, the Reynolds number must be defined.

The Reynolds number is a dimensionless term that is defined as the ratio between the inertial and viscous forces in a fluid problem (Lienhard and Lienhard 2006). In equation form, the Reynolds number is:

$$\mathrm{Re} \equiv \frac{UL}{\nu} \tag{2.9a}$$

where Re is the Reynolds number, U is a characteristic velocity scale (m/s), L is a characteristic length scale (m), and ν is the kinematic viscosity of the fluid (m^2/s). For flow over a flat plate, the Reynolds number can be expressed as:

$$\mathrm{Re}_x \equiv \frac{U_\infty x}{\nu} \tag{2.9b}$$

where Re_x is the Reynolds number at a given point, U_∞ is the fluid reference velocity (m/s) and x is the distance from the start of flow development to a given point (m).

The Reynolds number is often used to describe the regime of a particular flow: laminar, transitional, or turbulent. For example, Lienhard and Lienhard (2006) suggest that for air flowing over a flat plate with a leading edge, at zero incidence, the transitional region would begin at roughly $\mathrm{Re}_x = 3.5\times10^5$, and that full turbulence would be reached at roughly $\mathrm{Re}_x = 4.0\times10^6$. However, there are a number of other factors that can affect the exact point of transition from one region to another, such as surface roughness, acoustic or structural vibrations, or the shape of the leading edge. In addition, in practice, the lengths L (from Equation 2.9a) and x (from Equation 2.9b) are often arbitrary quantities, and it is often difficult to determine what characteristic length should be used for a given problem (Blocken 2004).

Another important dimensionless parameter is the Prandtl number, which is used to describe the relationship between the thermal and flow conditions. Specifically, the Prandtl number is the ratio of the molecular momentum diffusivity to the thermal diffusivity. In equation form, the Prandtl number is:

$$Pr \equiv \frac{\nu}{\alpha} \tag{2.10}$$

where ν is the kinematic viscosity (m^2/s), and α is the thermal diffusivity (m^2/s). Analytical solutions for boundary layer flow over a flat plate show that the Nusselt number described in Equation 2.5 can also be expressed as a function of the Reynolds

and Prandtl numbers (Kreith and Bohn 2001). For this reason, most equations correlating experimental data are presented in the following form:

$$Nu = f_1(\mathrm{Re}) * f_2(\mathrm{Pr}) \tag{2.11}$$

where f_1 and f_2 are empirical functions.

2.2.2. *NATURAL CONVECTION*

When a fluid is in contact with a body that is at higher or lower temperature, the density of the fluid will change close to the surface of the body. As the buoyancy force overcomes the viscous force, the change in density will result in fluid movement (and heat transfer) at the surface, which is described as natural convection (Kreith and Bohn 2001). Unlike forced convection, the effect of gravity on natural convection is very important. This is factored into the Grashov number (Gr), which is the ratio between the buoyancy and viscous forces:

$$Gr_L \equiv \frac{g\beta(T_s - T_{ref})L^3}{\nu^2} \tag{2.12}$$

where g is the gravitational constant (=9.81 m/s^2), β is the thermal expansion coefficient (K^{-1}), T_s and T_{ref} are the surface and fluid reference temperatures (K), and L is the characteristic length scale (m).

The Grashov number is often combined with the Prandtl number to form the Rayleigh number (Ra), which is a very commonly used parameter for natural convection problems.

$$Ra \equiv Gr_L Pr \equiv \frac{g\beta(T_s - T_{ref})L^3}{\nu\alpha} \tag{2.13}$$

In general, the magnitude of the Rayleigh number will describe whether the natural convection is laminar or turbulent. Rayleigh numbers below 10^8 are indicative of buoyancy driven laminar natural convection, while values in the range of $10^8 < Ra < 10^{10}$ are indicative of the transition to turbulent flow (Fluent Inc. 2003).

Nusselt number correlations for natural convection are typically expressed as functions of the Grashov and Prandtl numbers, or in equation form (Lienhard and Lienhard 2006):

$$Nu = f_1(Gr) * f_2(Pr) \tag{2.14}$$

where f_1 and f_2 are empirical functions. Since the product of the Grashov and the Prandlt numbers has already been defined as the Rayleigh number, Equation 2.14 can be altered slightly to be a function of the Rayleigh and Prandtl numbers:

$$Nu = f(Ra, Pr) \tag{2.15}$$

Many correlations in the form of Equation 2.15 exist in literature for a wide variety of applications. One particular natural convection correlation that is used for comparison in the context of this thesis is presented later in Chapter 5.

2.3. Numerical Modelling and Computational Fluid Dynamics

Numerical modelling is generally less expensive, less time-consuming and more flexible than experimental work. While experimental data can often be limited to where a sensor can be physically placed, data can be obtained for literally any location in a numerical simulation. However, the accuracy of numerical modelling is dependent on the degree of complexity of the model and the simplifications used to solve the governing equations. This section will focus primarily on the governing equations of fluid flow and on the turbulence models that are used in the commercial CFD code *Fluent 6.2.16*.

2.3.1. Governing Equations

There are four fundamental principles in physics that define how a physical problem must behave: 1) mass must be conserved, 2) Newton's second law must be obeyed, 3) energy must be conserved, and 4) the 2nd law of thermodynamics must be obeyed (see e.g. Kreith and Bohn 2001). Based on these four principles, three governing equations may be defined. Since the scope of this research pertains only to two-dimensional flows, the equations that follow shall be expressed only in two dimensions.

The first governing equation is the continuity equation, which describes how conservation of mass is maintained in a calculation. In a given two-dimensionally moving fluid, the velocity vector at a given point at a given moment in time can be expressed as the following equation (Lienhard and Lienhard, 2006):

$$\vec{V} = u\vec{i} + v\vec{j} \tag{2.16}$$

where $\vec{V}$ is the instantaneous velocity vector, u and v are the instantaneous x- and y-components of the velocity (m/s), and $\vec{i}$ and $\vec{j}$ are the unit vectors in the x- and y-directions.

For incompressible flows, the two-dimensional equation that expresses mathematically that a flow is continuous through a given control volume can be expressed as (Lienhard and Lienhard 2006):

$$div(\vec{V}) = \frac{\partial u}{\partial x} + \frac{\partial v}{\partial y} = 0 \tag{2.17}$$

where *div* is the divergence operator.

For two-dimensional problems, conservation of momentum can be described by two scalar formulae called the Navier-Stokes equations (Lienhard and Lienhard 2006). For CFD modelling, the continuity, momentum and energy equations are lumped together under the "Navier-Stokes" title as a general rule (Blocken 2004). The Navier-Stokes equations relevant to this research are presented below in Equations 2.18a to 2.18d (see e.g. Blocken 2004, Lienhard and Lienhard 2006).

Continuity: $$div(\vec{V}) = 0 \tag{2.18a}$$

Momentum: $$\rho\frac{\partial u}{\partial t} + \rho\, div(u\vec{V}) = -\frac{\partial p}{\partial x} + div(\mu\, grad(u)) \tag{2.18b}$$

$$\rho\frac{\partial v}{\partial t} + \rho\, div(v\vec{V}) = -\frac{\partial p}{\partial y} + div(\mu\, grad(v)) \tag{2.18c}$$

Energy: $$\rho C_p\left(\frac{\partial T}{\partial t} + \vec{V}\cdot grad(T)\right) = k\nabla^2 T + \dot{q} \tag{2.18d}$$

where t is the time coordinate (s), p is the instantaneous pressure (Pa), *grad* is the gradient operator, ∇^2 is the Laplacian operator, and $\dot{q}$ is the heat generated (W/m^3). Equations 2.18a to 2.18d are valid for any incompressible, two-dimensional, viscous flow of a Newtonian fluid (Blocken 2004).

2.3.2. *MODELLING OF TURBULENT FLOWS*

Turbulence is characterized by the fluctuation that occurs within a velocity field (Fluent Inc. 2003). Velocities are no longer simple vectors with scalar magnitudes; they have mean values and fluctuation components. In equation form, an instantaneous velocity vector would be expressed as (Blocken 2004):

$$\vec{a} = \vec{A} + \vec{a}' \tag{2.19}$$

where $\vec{a}$ is an instantaneous velocity vector, $\vec{A}$ is the mean component, and $\vec{a}'$ is the fluctuation component. Note that the expression from Equation 2.19 can also be applied to scalar quantities such as pressure, temperature or species concentration. As an example, the fluctuating nature of the velocity vector in stationary conditions is shown below in Figure 2.3 (Kreith and Bohn 2001).

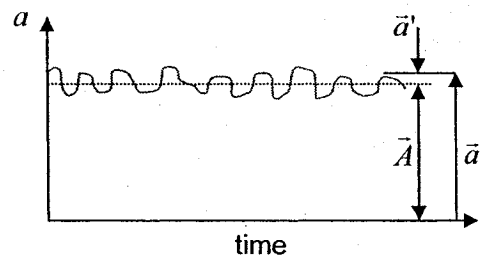

Figure 2.3. Time variation of instantaneous velocity

In order to account for the fluctuating aspect of turbulent flow, the governing equations must be manipulated to solve for the mean flow of the problem. If the fluctuating velocity components were to be individually solved in a simulation, it would quickly become too computationally expensive to calculate (Fluent Inc. 2003). In order to simplify the solution procedure, there are several methods that exist, including Reynolds-averaged Navier-Stokes (RANS) and Large Eddy Simulation (LES) (Fluent Inc. 2003, Blocken 2004). Only RANS equations will be used within the scope of this research.

According to CFD documentation, a complete direct numerical solution (DNS) of the Navier-Stokes equations for turbulent flows around complex geometries is not possible at this point in time (Fluent Inc. 2003). In order to significantly reduce the complexity of a problem, the RANS equations take into account the effect of velocity fluctuations on the mean flow through the use of turbulence models. The equations can either be time-averaged for steady-state problems, or ensemble-averaged for transient problems (Blocken 2004).

To obtain the so-called RANS equations, the mean and fluctuating components of the velocity are inserted into the governing equations from Equation 2.18 (Blocken 2004):

$$div(\vec{V}) = 0 \qquad (2.20)$$

$$\rho\frac{\partial U}{\partial t}+\rho\, div(U\vec{V})=-\frac{\partial p}{\partial x}+div(\mu\, grad(U))+\left[-\frac{\partial\rho\overline{u'^2}}{\partial x}-\frac{\partial\rho\overline{u'v'}}{\partial y}\right] \quad (2.21a)$$

$$\rho\frac{\partial V}{\partial t}+\rho\, div(V\vec{V})=-\frac{\partial p}{\partial y}+div(\mu\, grad(V))+\left[-\frac{\partial\rho\overline{u'v'}}{\partial x}-\frac{\partial\rho\overline{v'^2}}{\partial y}\right] \quad (2.21b)$$

where $\overline{u'^2}$, $\overline{v'^2}$ and $\overline{u'v'}$ are called the Reynolds stresses.

Due to the addition of the Reynolds stresses in Equation 2.21a and 2.21b, the governing equations for turbulent flow contain more variables than the number of equations. The Boussinesq hypothesis states that the Reynolds stresses can be expressed as a function of the mean velocity components, for example (Fluent Inc. 2003):

$$-\rho\overline{u'v'}=\mu_t\left(\frac{\partial U}{\partial y}+\frac{\partial V}{\partial x}\right)-\frac{2}{3}\left(\rho k+\mu_t\frac{\partial U}{\partial x}\right)\delta_{ij} \quad (2.22)$$

The turbulent viscosity μ_t is the principal unknown in Equation 2.22, and is obtained differently depending on the turbulence model. Specific details for each model are presented in Section 2.3.4. All of the turbulence models used in this thesis are used for the RANS equations, while the Boussinesq approach is applicable to all of the turbulence models except the Reynolds Stress Model, which has a unique method of determining the Reynolds stresses. The energy equations are described for each individual turbulence model in Section 2.3.4.

In order to understand some of the differences between the turbulence models, the concept of near-wall modelling is presented.

2.3.3. *NEAR-WALL MODELLING*

Boundary layer (BL) velocity and temperature profiles are generally described using dimensionless parameters. Before the BL regions can be discussed in proper detail, some dimensionless terms must be introduced:

$$y^+\equiv\frac{yu^*}{\nu} \quad (2.23)$$

where y^+ is the dimensionless distance from the wall, y is the distance from the wall (m), and u^* is the friction velocity (m/s) defined as:

$$u^*\equiv\sqrt{\frac{\tau_w}{\rho}} \quad (2.24)$$

where τ_w is the wall shear stress (Pa). The wall shear stress is based on the velocity gradient in the direction normal to the surface of the wall, or in equation form:

$$\tau_w \equiv \mu \left. \frac{\partial U}{\partial y} \right|_{y=0} \tag{2.25}$$

where U is the fluid velocity along the wall (m/s). The fluid velocity tangential to the wall can be described in a dimensionless form as a function of the fluid velocity and the friction velocity:

$$u^+ \equiv \frac{U}{u^*} \tag{2.26}$$

For cases with heat transfer, the dimensionless temperature may be calculated using the following equation:

$$T^+ \equiv \frac{T_w - T_f}{T'} \tag{2.27}$$

where T_w is the wall temperature at a certain point (K), T_f is the fluid temperature (K), and T' is defined as

$$T' \equiv \frac{\alpha q_w}{k u^*} \tag{2.28}$$

where q_w is the wall heat flux (W/m^2).

There are two common near-wall modelling techniques employed in CFD: Low-Reynolds-number modelling and Wall function theory.

Low-Reynolds-number modelling (Low-Re)

If the boundary layer is meshed sufficiently fine so that the first cell is placed entirely in the laminar sublayer of the BL, the approach used is generally referred to as Low-Re modelling. In Low-Re modelling, the governing equations of fluid flow are solved in all regions of the BL. It is more time consuming but generally more accurate than the wall-function approach. In dimensionless units, the height of the first cell is generally taken to be approximately $y^+ = 1$, though the laminar sublayer is valid up to $y^+ < 5$ (Blocken 2004). In the range of $5 < y^+ < 30$, there exists a buffer region between the laminar sublayer and the log-law region of the boundary layer. It is generally not advisable to have meshes where the first cell lies within the buffer region, though often it is unavoidable in CFD. For meshes where the first cell center is located at $y^+ > 30$, wall function theory may be applied.

Wall function theory

Fluid flow over a smooth flat plate is referred to as the simplest case for analytical fluid dynamics (Schetz 1993). There has been a significant amount of work done in experiments for boundary layer flow evaluation (which was later summarized in Bejan 1984, Schlichting 1987, Schetz 1993, Chen and Jaw 1998, etc). That work was transformed into the *wall function* concept (e.g. Spalding 1961). Wall functions allow CFD models to interpret behaviour near a wall without the need for a very fine mesh that also discretises the generally quite thin laminar sublayer at the surface of the wall. The wall function equations are based on an analytical solution of the transport equations in combination with experimental data fitting. The result is a reduction in computation time and a relatively accurate representation of what happens within the BL, at least under the conditions for which the wall functions were derived. Wall functions are recommended for high Reynolds number flows where the domain is complex or large enough that it would require an extremely elaborate mesh leading to a long computation time. On the other hand, wall functions may cease to be valid in complex situations. Nevertheless, they are often used – even when not valid – for complex calculations, which can be responsible for considerable errors in near-wall flow and the related convective heat transfer coefficients (Blocken 2004).

Wall functions are generally described as having two regions: the laminar sublayer and the log-law layer. It is commonly accepted in CFD that the laminar sublayer is said to be valid in the region where $y^+ <$ (5 to 10) (Chen and Jaw 1998). The equations for the dimensionless velocity and temperature within this region are (Fluent Inc. 2003):

$$u^+ = y^+ \tag{2.29}$$

$$T^+ = Pry^+ \tag{2.30}$$

The region above the laminar sublayer ($y^+ > 30$) is the log-law layer, which is generally described in the form of:

$$n^+ = A \ln y^+ + B \tag{2.31}$$

where n is either the dimensionless velocity or dimensionless temperature. The constants A and B in Equation 2.31 are usually fitted to experimental data, and are consistent throughout the literature. For the purpose of this thesis, the following equations will be used (Fluent Inc. 2003):

$$u^+ = 2.5 \ln y^+ + 5.45 \tag{2.32}$$

$$T^+ = \mathrm{Pr}_t \left[\frac{1}{\kappa} \ln(Ey^+) + P \right] \tag{2.33}$$

where Pr_t is the turbulent Prandtl number (= 0.85 for air), E is an experimentally determined constant (= 9.793), and P is described by the following equation:

$$P = 9.24 \left[\left(\frac{\mathrm{Pr}}{\mathrm{Pr}_t} \right)^{3/4} - 1 \right] \left[1 + 0.28 e^{-0.007 \left(\frac{\mathrm{Pr}}{\mathrm{Pr}_t} \right)} \right] \tag{2.34}$$

Spalding (1961) suggests an equation that will cover the entire y^+ range of values for the dimensionless velocity u^+ (including the buffer region):

$$y^+ = u^+ + C \left[\exp Du^+ - 1 - Du^+ - \frac{1}{2}(Du^+)^2 - \frac{1}{6}(Du^+)^3 - \frac{1}{24}(Du^+)^4 \right] \tag{2.35}$$

where $C=0.1108$ and $D=0.4$. The equations for the dimensionless velocity and temperature are illustrated in Figure 2.4.

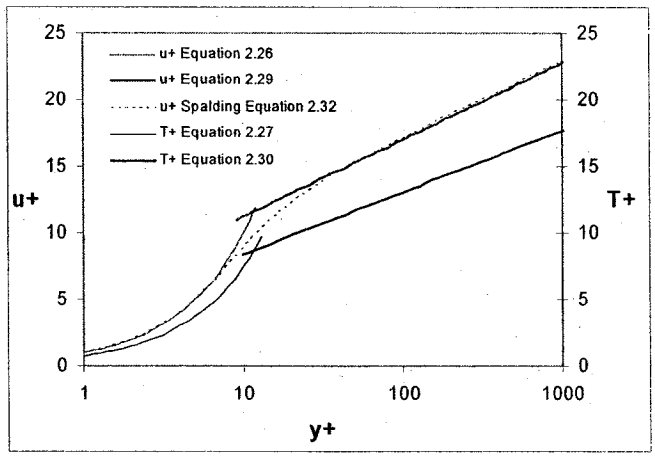

Figure 2.4. Wall function dimensionless velocity and temperature distributions

It is important to note that *Fluent* uses a slightly different dimensionless height y^*, but, for the cases that were examined here, the values of y^+ and y^* are equivalent (Fluent Inc. 2003).

2.3.4. *Turbulence Models*

There are a number of turbulence models that will be used throughout this thesis for turbulent simulations. CFD literature states that there is no single turbulence model that is ideal for all problems. Each model has been developed for one or more practical

applications and is either more or less adequate for other applications (Fluent Inc. 2003). For CFD simulations, the documentation accompanying the software will generally provide a very good description of the differences between the turbulence models. In order to facilitate comparison between the models, they are briefly outlined below (Fluent Inc. 2003).

As mentioned earlier, all of the turbulence models described below are used in combination with RANS equations, and all but the Reynolds Stress Model use the Boussinesq approach for modelling the Reynolds stresses. The focus of this section will be primarily on the specific differences between the turbulence models. In the interest of conciseness, some terms in the equations to follow are only defined in general terms. For exact equations and/or definitions, it is recommended to refer to the references provided for the equations. In general, all of the turbulence model equations and information have been obtained from Fluent Inc. (2003) unless otherwise specified.

The Spalart-Allmaras Model

The Spalart-Allmaras (SA) model was developed for aerospace applications and is also commonly used for turbomachinery applications. Originally, the SA model was intended for Low-Re modelling only, since it required the proper resolution of the laminar sublayer region of the boundary layer. In *Fluent* however, the model was adapted to include wall function capabilities. The model itself is considered to be relatively simple due to the single additional transport equation. The transported variable, $\tilde{\upsilon}$, is essentially the turbulent kinematic viscosity with some slight differences within the laminar sublayer that are outlined below.

$$\frac{\partial}{\partial t}(\rho\tilde{\upsilon})+\frac{\partial}{\partial x_i}(\rho\tilde{\upsilon}U_i)=G_{\tilde{\upsilon}}+\frac{1}{\sigma_{\tilde{\upsilon}}}\left[\frac{\partial}{\partial x_j}\left\{(\mu+\rho\tilde{\upsilon})\frac{\partial\tilde{\upsilon}}{\partial x_j}\right\}+C_{b2}\rho\left(\frac{\partial\tilde{\upsilon}}{\partial x_j}\right)^2\right]-Y_{\upsilon}+S_{\tilde{\upsilon}} \quad (2.36)$$

where $G_{\tilde{\upsilon}}$ is the production of turbulent viscosity, Y_{υ} is the destruction of turbulent viscosity due to viscous damping in the near-wall region, $\sigma_{\tilde{\upsilon}}$ and C_{b2} are constants, and $S_{\tilde{\upsilon}}$ is a user-defined source term.

For Low-Re modelling, the wall shear stress is resolved using Equation 2.37, and Equation 2.38 is used for wall function meshes where the center of the first cell is located within the log-law layer.

$$\frac{U}{u_\tau} = \frac{\rho u_\tau y}{\mu} \tag{2.37}$$

$$\frac{U}{u_\tau} = \frac{1}{\kappa} \ln E\left(\frac{\rho u_\tau y}{\mu}\right) \tag{2.38}$$

where U is the velocity parallel to the wall surface, μ_τ is the shear velocity, y is the distance from the wall, κ is the von Kármán constant (=0.4187), and E is an experimentally determined constant (=9.783).

For problems in which there is heat transfer, the energy equation is given by:

$$\frac{\partial}{\partial t}(\rho E) + \frac{\partial}{\partial x_i}[U_i(\rho E + p)] = \frac{\partial}{\partial x_j}\left[\left(k + \frac{c_p \mu_t}{\mathrm{Pr}_t}\right)\frac{\partial T}{\partial x_j} + U_i(\tau_{ij})_{eff}\right] + S_h \tag{2.39}$$

where k is thermal conductivity, E is total energy (different from the constant previously described), and $(\tau_{ij})_{eff}$ is the deviatoric stress tensor, which represents viscous heating. Viscous heating was not considered for the simulations performed for this thesis.

The Standard k-ε Model

The standard k-ε model is only valid for fully turbulent flows, which is due to the way it was originally developed by Launder and Spalding (1972). The "k" represents turbulent kinetic energy and the "ε" is the dissipation rate. The corresponding transport equations to describe these two parameters are, respectively:

$$\frac{\partial}{\partial t}(\rho k) + \frac{\partial}{\partial x_i}(\rho k U_i) = \frac{\partial}{\partial x_j}\left[\left(\mu + \frac{\mu_t}{\sigma_k}\right)\frac{\partial k}{\partial x_j}\right] + G_k + G_b - \rho\varepsilon - Y_M + S_K \tag{2.40}$$

$$\frac{\partial}{\partial t}(\rho \varepsilon) + \frac{\partial}{\partial x_i}(\rho \varepsilon U_i) = \frac{\partial}{\partial x_j}\left[\left(\mu + \frac{\mu_t}{\sigma_\varepsilon}\right)\frac{\partial \varepsilon}{\partial x_j}\right] + C_{1\varepsilon}\frac{\varepsilon}{k}(G_k + C_{3\varepsilon}G_b) - C_{2\varepsilon}\rho\frac{\varepsilon^2}{k} + S_\varepsilon \tag{2.41}$$

where G_k is the generation of turbulent kinetic energy due to mean velocity gradients, G_b is the generation of turbulent kinetic energy due to buoyancy effects, Y_M is the contribution of fluctuating dilatation in compressible turbulence to the overall dissipation rate, $C_{1\varepsilon}$, $C_{2\varepsilon}$ and $C_{3\varepsilon}$ are constants, σ_k and σ_ε are the turbulent Prandtl numbers for k and ε, and S_k and S_ε are user-defined source terms.

The turbulent viscosity, which is required to compute the Reynolds stresses according to the Boussinesq approach, is defined by the following equation for the k-ε model:

$$\mu_t = \rho C_\mu \frac{k^2}{\varepsilon} \tag{2.42}$$

where C_μ is a constant.

The effects of buoyancy will become important for the simulations of natural convection. The generation of turbulence due to buoyancy can be expressed as:

$$G_b = \beta g_i \frac{\mu_t}{\mathrm{Pr}_t} \frac{\partial T}{\partial x_i} \tag{2.43}$$

where β is the thermal expansion coefficient, g_i is the component of gravity in the direction of *i*. It is important to note that the buoyancy effects for the turbulent dissipation rate ε are neglected within Fluent (as a default setting). This is accomplished by setting the term G_b to be equal to zero in Equation 2.41.

The energy equation for the standard k-ε model is described by the following formula:

$$\frac{\partial}{\partial t}(\rho E) + \frac{\partial}{\partial x_i}\left[U_i(\rho E + p)\right] = \frac{\partial}{\partial x_j}\left(k_{eff}\frac{\partial T}{\partial x_i} + U_i\left(\tau_{ij}\right)_{eff}\right) + S_h \tag{2.44}$$

where k_{eff} is effective thermal conductivity, *E* is total energy, and $\left(\tau_{ij}\right)_{eff}$ is the deviatoric stress tensor, which represents viscous heating. The effective thermal conductivity is expressed as:

$$k_{eff} = k + \frac{c_p \mu_t}{\mathrm{Pr}_t} \tag{2.45}$$

where *k* refers to the thermal conductivity and not the turbulent kinetic energy.

The RNG k-ε Model

RNG is an abbreviation for Renormalization Group, which is a statistical technique used to develop the turbulence model from the instantaneous Navier-Stokes equations. The RNG k-ε Model will henceforth be referred to as the RNG model for simplicity. In general there are many similarities between the RNG and Standard k-ε models, and therefore only the differences are outlined below. The RNG model has an additional term in the dissipation rate equation, which is intended to improve the

accuracy for rapidly strained turbulent flows. The effect of swirl on turbulence is included in the RNG model, and the turbulent Prandtl numbers are modelled using an analytical formula instead of by user-defined constant values. In general, the RNG model is said to be more accurate and more reliable for more flows than the Standard k-ε model (Fluent Inc. 2003).

The transport equations for the RNG model are as follows:

$$\frac{\partial}{\partial t}(\rho k)+\frac{\partial}{\partial x_i}(\rho k U_i)=\frac{\partial}{\partial x_j}\left(\alpha_k \mu_{eff}\frac{\partial k}{\partial x_j}\right)+G_k+G_b-\rho\varepsilon-Y_M+S_K \quad (2.46)$$

$$\frac{\partial}{\partial t}(\rho \varepsilon)+\frac{\partial}{\partial x_i}(\rho \varepsilon U_i)=\frac{\partial}{\partial x_j}\left(\alpha_\varepsilon \mu_{eff}\frac{\partial \varepsilon}{\partial x_j}\right)+C_{1\varepsilon}\frac{\varepsilon}{k}(G_k+C_{3\varepsilon}G_b)-C_{2\varepsilon}\rho\frac{\varepsilon^2}{k}-R_\varepsilon+S_\varepsilon \quad (2.47)$$

where α_k and α_ε are the inverse Prandtl numbers for k and ε, μ_{eff} is the effective turbulent viscosity, and R_ε is a term used to modify the turbulent dissipation rate for rapidly constrained flows. The inverse Prandtl number α is defined as:

$$\left|\frac{\alpha-1.3929}{\alpha_0-1.3929}\right|^{0.6321}\left|\frac{\alpha+2.3929}{\alpha_0+2.3929}\right|^{0.3679}=\frac{\mu_{mol}}{\mu_{eff}} \quad (2.48)$$

where α_0 generally equals 1.0.

For the RNG model, energy is solved using the same equation as the Standard k-ε model (Equation 2.44). The difference between the two models arises due to the way the effective conductivity is calculated:

$$k_{eff}=\alpha c_p \mu_{eff} \quad (2.49)$$

where α is the inverse Prandtl number calculated from Equation 2.45 but with α_0=1/Pr.

The Realizable k-ε Model

The Realizable k-ε model is named due to the fact that the model satisfies certain mathematical constraints on the normal Reynolds stresses that are consistent with the physics describing turbulent flows. The primary differences between the Realizable and Standard k-ε models are an additional formula describing the parameter C_μ, which is no longer considered constant, and a new equation for the turbulence dissipation rate. The transport equations for k and ε are given by:

$$\frac{\partial}{\partial t}(\rho k)+\frac{\partial}{\partial x_i}(\rho k U_j)=\frac{\partial}{\partial x_j}\left[\left(\mu+\frac{\mu_t}{\sigma_k}\right)\frac{\partial k}{\partial x_j}\right]+G_k+G_b-\rho\varepsilon-Y_M+S_K \quad (2.50)$$

$$\frac{\partial}{\partial t}(\rho \varepsilon)+\frac{\partial}{\partial x_i}(\rho \varepsilon U_j)=\frac{\partial}{\partial x_j}\left[\left(\mu+\frac{\mu_t}{\sigma_\varepsilon}\right)\frac{\partial \varepsilon}{\partial x_j}\right]+\rho C_1 S_\varepsilon-\rho C_2\frac{\varepsilon^2}{k+\sqrt{\nu\varepsilon}}+C_{1\varepsilon}\frac{\varepsilon}{k}C_{3\varepsilon}G_b+S_\varepsilon \quad (2.51)$$

The equation for the turbulent kinetic energy is the same as for the Standard k-ε model. The primary difference for the Realizable model is that the production term in the turbulence dissipation rate equation is no longer a function of the turbulent kinetic energy. In previous models, the equation for ε contained the production term G_k. Also, the destruction term no longer contains a potential singularity that could arise with the Standard and RNG k-ε models when turbulent kinetic energy tends towards zero.

The eddy viscosity is calculated with Equation 2.42, with the notable difference that the parameter C_μ is no longer a constant but is determined with the equation:

$$C_\mu=\frac{1}{A_0+A_s\dfrac{kU^*}{\varepsilon}} \quad (2.52)$$

Equation 2.52 is a function of the mean strain and rotation rates, the angular velocity of the system rotation and the turbulence kinetic energy and dissipation rates. Details on the exact parameters may be found in Fluent Inc. (2003).

For the Realizable k-ε model, the energy equation has the same form as the Standard k-ε model described in Equations 2.44 and 2.45.

The Standard k-ω Model

The k-ω model is described by transport equations for the turbulent kinetic energy k and the specific dissipation rate ω. The specific dissipation rate is effectively a ratio between the turbulence dissipation rate ε and the turbulent kinetic energy *k*:

$$\omega=\frac{\varepsilon}{kC_\mu} \quad (2.53)$$

The k-ω model is effective for modelling wall-bounded and free shear flows, and is essentially a low Reynolds number model. The transport equations are as follows:

$$\frac{\partial}{\partial t}(\rho k)+\frac{\partial}{\partial x_i}(\rho k U_i)=\frac{\partial}{\partial x_j}\left(\Gamma_k\frac{\partial k}{\partial x_j}\right)+G_k-Y_k+S_k \quad (2.54)$$

$$\frac{\partial}{\partial t}(\rho\omega)+\frac{\partial}{\partial x_i}(\rho\omega U_i)=\frac{\partial}{\partial x_j}\left(\Gamma_\omega\frac{\partial\omega}{\partial x_j}\right)+G_\omega-Y_\omega+S_\omega \tag{2.55}$$

where Γ_k and Γ_ω are effective diffusivity terms for k and ω, G_k and G_ω are generation terms, Y_k and Y_ω are turbulence dissipation terms, and S_k and S_ω are user-defined source terms.

The effective diffusivity values are calculated based on the turbulent Prandtl numbers and the turbulent viscosity:

$$\Gamma_k=\mu+\frac{\mu_t}{\sigma_k} \tag{2.56}$$

$$\Gamma_\omega=\mu+\frac{\mu_t}{\sigma_\omega} \tag{2.57}$$

where the turbulent viscosity μ_t is expressed as:

$$\mu_t=\alpha^*\frac{\rho k}{\omega} \tag{2.58}$$

where α^* is a correction factor for damping the turbulent viscosity for Low-Re flows. For high Reynolds number flows, α^* would be equal to 1.

For all intents and purposes, the energy equation for the Standard k-ω model is the same as Equation 2.44 used for the Standard k-ε model.

The SST k-ω Model

The Shear-Stress Transport (SST) version of the k-ω model differs from the standard model in a number of ways. First of all, it is effectively a combination of the Standard k-ω model and the Standard k-ε model. The k-ω model is applied to near-wall regions and the k-ε model is applied to far-field regions, and the two models are combined using a blending function. In addition, the turbulent viscosity is modified to account for the transport of the turbulent shear stress, and some of the constants from the transport equations are slightly different. Finally, the specific dissipation transport equation contains an additional damped cross-diffusion derivative term.

$$\frac{\partial}{\partial t}(\rho k)+\frac{\partial}{\partial x_i}(\rho k U_i)=\frac{\partial}{\partial x_j}\left(\Gamma_k\frac{\partial k}{\partial x_j}\right)+G_k-Y_k+S_k \tag{2.59}$$

$$\frac{\partial}{\partial t}(\rho\omega)+\frac{\partial}{\partial x_i}(\rho\omega U_i)=\frac{\partial}{\partial x_j}\left(\Gamma_\omega\frac{\partial\omega}{\partial x_j}\right)+G_\omega-Y_\omega+D_\omega+S_\omega \tag{2.60}$$

where D_ω is the cross-diffusion derivative term, defined as:

$$D_\omega=2(1-F_1)\rho\sigma_{2,\omega}\frac{1}{\omega}\frac{\partial k}{\partial x_j}\frac{\partial\omega}{\partial x_j} \tag{2.61}$$

where F_1 is a blending function, and $\sigma_{2,\omega}$ is a constant. The effective diffusivity terms Γ_k and Γ_ω are calculated as described in Equations 2.56 and 2.57. The primary difference arises from the turbulent viscosity, μ_t, which is calculated using the following equation:

$$\mu_t=\frac{\rho k}{\omega}\frac{1}{\max\left[\frac{1}{\alpha^*},\frac{\Omega F_2}{a_1\omega}\right]} \tag{2.62}$$

where α^* is the correction factor described for Equation 2.57, Ω is a function of the mean rate-of-rotation tensor, F_2 is a blending function, and a_1 is a constant.

For all intents and purposes, the energy equation for the SST k-ω model is the same as Equation 2.44 used for the Standard k-ε model.

The Reynolds Stress Model

The Reynolds Stress Model (RSM) closes the RANS equations by solving transport equations for the Reynolds stresses instead of using the Boussinesq approach described earlier. It is the most complex RANS turbulence model included in the *Fluent* commercial CFD code used for this research. In addition, the dissipation rate is also solved with a transport equation, which results in a total of five transport equations for two-dimensional flow problems. The complexity of the model yields a greater potential to model complex flows, but, in the end, it is still limited due to the approximations and assumptions used in the transport equations for the Reynolds stresses. For very complex flow problems, which are not the focus of this research, the RSM is considered particularly appropriate. It is included in the results for the sake of completeness, but in general the extra computational requirements would not be justified for the relatively simple flow cases described in this thesis.

The transport equation for the Reynolds stresses is expressed as:

$$\frac{\partial}{\partial t}\left(\rho\overline{u_i'u_j'}\right)+\frac{\partial}{\partial x_k}\left(\rho U_k\overline{u_i'u_j'}\right)=-\frac{\partial}{\partial x_k}\left[\rho\overline{u_i'u_j'u_k'}+\overline{p\left(\delta_{kj}u_i'+\delta_{ik}u_j'\right)}\right]+\frac{\partial}{\partial x_k}\left[\mu\frac{\partial}{\partial x_k}\left(\overline{u_i'u_j'}\right)\right]$$
$$-\rho\left(\overline{u_i'u_k'}\frac{\partial u_j}{\partial x_k}+\overline{u_j'u_k'}\frac{\partial u_i}{\partial x_k}\right)-\rho\beta\left(g_i\overline{u_j'\theta}+g_j\overline{u_i'\theta}\right)+\overline{p\left(\frac{\partial u_i'}{\partial x_j}+\frac{\partial u_j'}{\partial x_i}\right)}-2\mu\overline{\frac{\partial u_i'}{\partial x_k}\frac{\partial u_j'}{\partial x_k}} \qquad (2.63)$$
$$-2\rho\Omega_k\left(\overline{u_j'u_m'}\varepsilon_{ikm}+\overline{u_i'u_m'}\varepsilon_{jkm}\right)+S_{user}$$

The left hand side of Equation 2.63 represents the local time derivative and the convection terms. On the right hand side, the terms represent (in order): turbulent diffusion, molecular diffusion, stress production, buoyancy production, pressure strain, dissipation, system rotation production, and a user-defined source term. The details for each part of the equation are not presented here, but more information can be found in Fluent Inc. 2003.

For all intents and purposes, the energy equation for the RSM is the same as Equation 2.44 used for the Standard k-ε model.

2.3.5. *RADIATION MODELLING*

Some equations for radiation have been presented earlier in Section 2.1.1. For CFD, there are a number of ways to model radiation that are applicable to different problems. For example, in *Fluent* there are five different radiation models, one of which was selected for the cases simulated during this research: the Discrete Transfer Radiation Model (DTRM). The DTRM states that radiation can be modelled as a finite number of rays that represent the heat transferred from one point to all other (visible) points in the domain. The number of rays in a given domain is based upon the number of grid cells that exist along an emitting material surface and based on the user-defined number of rays that are emitted from a given point. In addition, the cells along a surface can be clustered together to improve the computational efficiency of the calculation at the expense of accuracy. Figure 2.5 illustrates the relevant radiation modelling principles.

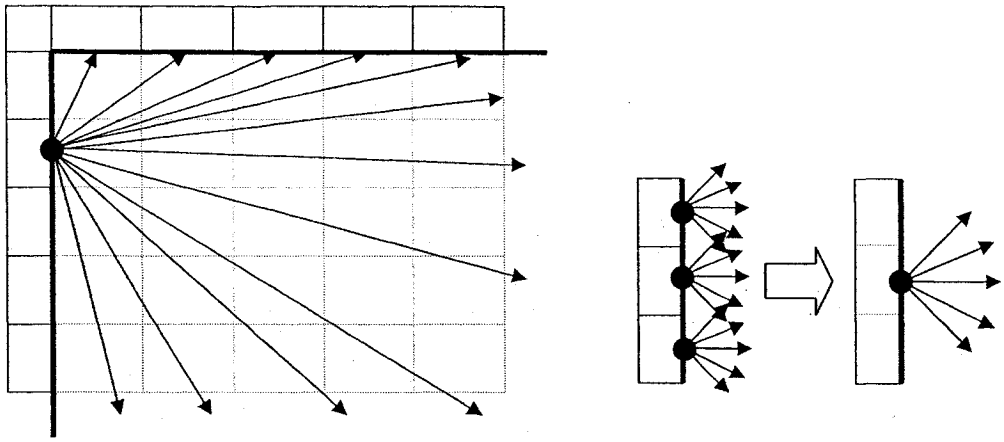

Figure 2.5. Radiation modelling principles

Fluent Inc. (2003) states a number of advantages for the Discrete Transfer Radiation Model. First of all, the DTRM is considered to be relatively simple when compared with other radiation models, and therefore better suited for cases that are not overly complex. Also, the accuracy of the model can be increased or decreased by modifying the number of rays from each point or the degree of clustering of the surface mesh. Finally, the model applies to a variety of optical thicknesses, which is a measure of the absorption coefficient and characteristic length of a problem. Also, the boundary conditions for the DTRM are rather simple, which require only the emissivity of the surface material. More importantly, the cases studied in this thesis all satisfy the requirements for the DTRM that are outlined in Fluent Inc. (2003).

2.4. COUPLED HEAT AND VAPOUR TRANSFER

The convective processes for heat and vapour transfer were previously defined in Sections 2.1.1 and 2.1.2, respectively. Heat and vapour transfer have been described previously as analogous processes, and the implication of the term "analogous" will be defined in this section. Previous work in coupled heat and vapour transfer for experiments and modelling are presented.

As a support for the description of the combined heat and vapour transfer processes, an example is presented. If one considers flow over a flat plate with a sharp leading edge, an analytical solution can be obtained for laminar flow. The derivation of

the analytical solution can be found in most fluid mechanics or heat transfer textbooks. The momentum equation for such a case can be derived to be (Kreith and Bohn 2001):

$$U\frac{\partial U}{\partial x}+V\frac{\partial U}{\partial y}=\nu\left(\frac{\partial^2 U}{\partial y^2}\right) \tag{2.64}$$

where U is the streamwise velocity (m/s), V is the velocity perpendicular to the plate (m/s), and ν is the kinematic viscosity (m^2/s). A similar derivation can be performed for temperature and mass concentration, which are presented below in Equation 2.65 and 2.66, respectively.

$$U\frac{\partial T}{\partial x}+V\frac{\partial T}{\partial y}=\alpha\left(\frac{\partial^2 T}{\partial y^2}\right) \tag{2.65}$$

$$U\frac{\partial C}{\partial x}+V\frac{\partial C}{\partial y}=D_{eff}\left(\frac{\partial^2 C}{\partial y^2}\right) \tag{2.66}$$

where C is vapour concentration ($kg_{moisture}/m^3_{air}$), and D_{eff} is the effective vapour diffusivity (m^2/s). It should be noted that, while vapour concentration is used in Equation 2.66, it can be transformed into partial vapour pressure by using the ideal gas law.

The units for the kinematic viscosity, thermal diffusivity, and effective vapour diffusivity are all the same. This uniformity highlights the similarities between the three equations presented above. The Prandtl number has already been defined as the ratio of the kinematic viscosity (ν) to the thermal diffusivity (α). If the Prandtl number were to be equal to 1, the solutions to the momentum and energy equations would be identical. This leads to the conclusion that the Prandtl number describes the relationship between the velocity and temperature distributions (Kreith and Bohn 2001).

The analogue to the Prandtl number for vapour transport is called the Schmidt number, which is the ratio of the kinematic viscosity to the effective vapour diffusivity. In equation form, the Schmidt number is:

$$Sc\equiv\frac{\nu}{D_{eff}} \tag{2.67}$$

The same conclusion can be drawn for the Schmidt number as for the Prandtl number. Since the solution to the momentum and mass concentration equation would be the same if ν were equal to D_{eff}, the Schmidt number must describe the relationship between the velocity and concentration distributions (De Paepe and Steeman 2005).

Another relevant dimensionless term is the Lewis number, which relates the Schmidt and Prandtl numbers. The Lewis number relates the thermal and mass diffusion processes, which can be described in equation form as:

$$Le \equiv \frac{Sc}{Pr} \equiv \frac{\alpha}{D_{eff}} \tag{2.68}$$

The Lewis number describes the last remaining relationship between the three diffusivity terms, namely the ratio between the thermal and vapour concentration distributions.

In order to visualize the significance of the Prandtl, Schmidt and Lewis numbers, an example of laminar flow over a flat plate with a sharp leading edge is presented in Figure 2.6.

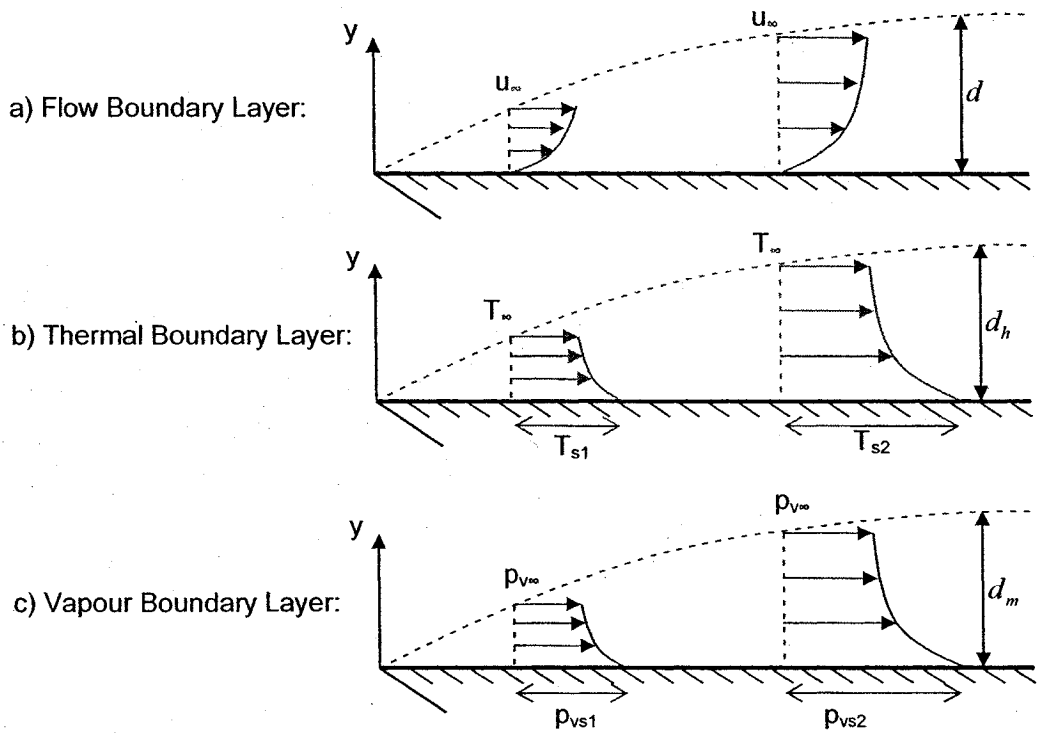

Figure 2.6. Sample boundary layer profiles

The three curves shown in Figure 2.6 represent typical boundary layer profiles for velocity, temperature, and vapour pressure (Kreith and Bohn 2001, De Paepe and Steeman 2005). The case shown above represents heat and vapour being transferred via convection from the wall surface to the air layer. The magnitudes of the profiles are not to a particular scale. The values of d, d_h and d_m represent the boundary layer thicknesses for, respectively, the velocity, temperature and vapour pressure curves.

Equations are available to determine the boundary layer thicknesses, but they are not relevant for the work presented in this thesis (see e.g. Schlichting 1987). The boundary layer profiles in Figure 2.6 have been plotted on three separate graphs for clarity, but in reality they are all interdependent, as shown in Figure 2.7.

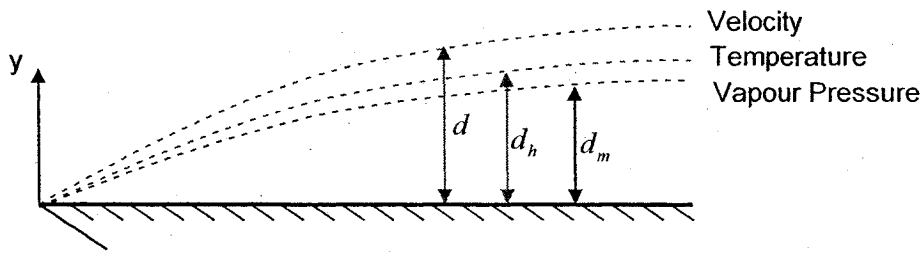

Figure 2.7. Superimposed boundary layer profiles

The example shown in Figure 2.7 illustrates the relative difference between the three profiles. The temperature boundary layer is a function of the velocity boundary layer (via the Prandtl number), the vapour pressure curve is a function of the velocity profile (via the Schmidt number), and finally, it follows that the temperature profile can be related to the vapour pressure profile. Note that the temperature and vapour pressure curves could also appear above the velocity curve if the Prandtl or Schmidt numbers are greater than unity. Another example of this type of boundary layer relationship was shown in the section on near-wall modelling. The velocity and temperature curves shown in Figure 2.4 are the same shape, and, in fact, the dimensionless temperature profile is proportional to the Prandtl number.

What has been briefly described as the relationship between velocity, temperature and vapour pressure, has been transformed into a well known analogy between the convective heat and vapour transfer coefficients (Chilton and Colburn 1934):

$$h_m = \frac{h_c}{\rho c_p Le^{2/3}} \tag{2.69}$$

where h_m is the convective vapour transfer coefficient (m/s), h_c is the convective heat transfer coefficient (W/m^{2}K), c_p is the specific heat (J/kg-K) and *Le* is the Lewis number. Equation 2.69 is often referred to as the Chilton-Colburn analogy. The analogy itself has been the subject of many research projects that prove and disprove the accuracy of the results for a variety of conditions. Note that the units of the convective vapour transfer coefficient are in *m/s*, which are not the same units as for a surface coefficient calculated

with vapour pressure as the driving potential. An alternative way of calculating the Chilton-Colburn analogy is to use the following equation:

$$h'_m = \frac{\delta_a}{k_a} h_c \tag{2.70}$$

where h'_m is the convective vapour transfer coefficient (s/m), δ_a is the vapour permeability of air (=1.87x10^{-10} s at 20 °C), and k_a is the conductivity of air.

Some experiments and modelling related to coupled heat and vapour transfer are presented in Section 2.4.1 and 2.4.2, respectively.

2.4.1. *Experiments in Coupled Heat and Vapour Transport*

A number of experiments have been performed in the past related to the determination of coupled heat and vapour transfer surface coefficients. Often, the goal of the work is to compare the results to the Chilton-Colburn analogy, either to prove or disprove the accuracy of Equation 2.69. A few examples of experiments are provided to demonstrate the discrepancy found in literature in results for the Chilton-Colburn analogy.

For example, Lewis (1970) performed mass transfer measurements around a single cylinder in cross flow for the purpose of using the Chilton-Colburn analogy to calculate heat transfer coefficients. His results showed that the error from the analogy was much less than the error due to free stream turbulence and wind tunnel blockage.

Wadsö (1993) presented experimental results that indicate that the Chilton-Colburn analogy is not applicable for vapour transport over wood surfaces, likely due to the non-Fickian behaviour of wood.

Derome (1999) performed a tunnel experiment that yielded convective mass transfer coefficients that differed with analogy values by up to 300%. Tremblay *et al* (2000) had a similar experimental setup and reported experimental values 150% larger than those calculated with the analogy. Subsequent work by Nabhani *et al* (2003) used an improved version of the experiment by Tremblay, and reported very large differences at high temperatures (90 °C) but had good agreement for lower temperatures.

2.4.2. *Modelling in Coupled Heat and Vapour Transport*

In addition to experimental work, some modelling of coupled heat and vapour transport has been performed. Given the difficulties associated with experimental measurements for vapour transport, validating numerical data for coupled models can be

challenging. Despite that fact, some numerical models and CFD simulations have been performed, and a few examples are provided below.

Ben Nasrallah and Perré (1987) developed a coupled heat and mass transfer model for forced convection over a porous medium. Their model predicted the drying rates for brick at a variety of temperatures, and included a sensitivity study for several parameters. The authors discussed the accuracy of the Chilton-Colburn analogy and stated that it was found to be valid when the vapour pressure of air is negligible with respect to the total pressure. At higher temperatures (60 to 95 °C), they found convective vapour transfer coefficients were up to five times the heat transfer coefficients, which corresponds well with the results from Nabhani *et al* (2003). The model was not compared to experimental data.

Derome *et al* (2003) developed a numerical model to simulate moisture transfer for wood planks in non-vented flat roofs. A sensitivity analysis on the model showed that large variations on the heat transfer coefficients did not result in significant changes in the drying curve for wood. However, when convective moisture transfer coefficients were varied, a larger impact could be seen on the drying process, particularly in the initial stages of drying.

Trujillo *et al* (2003) performed CFD calculations of heat and mass transfer during the evaporation of water from a cylinder for turbulent flow. The simulations did not model vapour transport within the material, only in the air around the cylinder. The results indicated a minimum discrepancy of 19% between the simulated convective heat and vapour transfer coefficients and Chilton-Colburn analogy coefficients. Heat of vaporization was included, and moisture transfer at the surface was modelled using a user-defined function for the moisture concentration. The authors conclude that, at low Reynolds numbers, the Chilton-Colburn analogy is not consistent around the cylinder when the effects of radiation are included.

Hedegaard *et al* (2004) used CFD to simulate moisture transport in both the air and the walls of a room. The walls were modelled as highly viscous fluids due to the inability of the CFD code to model vapour transport in solid materials. Different material properties and viscosities were tested for the viscous wall regions. A number of difficulties were found to be associated with implementing an immobile (yet fluid) region, particularly with turbulence enabled. Finally, the simulation proved to be too computationally expensive to perform as a transient simulation, and therefore only steady-state simulations were performed.

CHAPTER 3. LAMINAR FORCED CONVECTION

Laminar forced convection between parallel plates was selected as the first case for study because it is the simplest form of fluid flow, for which an analytical solution can be compared directly with simulation results. The cases studied in this chapter, which are illustrated in Figure 3.1, are intended to show whether CFD can accurately determine convective heat transfer coefficients for laminar flow.

The cases shown in Figure 3.1 assume that the velocity field has become fully developed before the heated region. This assumption is valid when

$$\frac{\partial U}{\partial x} = 0 \tag{3.1}$$

where U is the streamwise component of the velocity at any given height in the flow field (for horizontal plates) (m/s). Aerodynamically developed flow is a requirement for analytical solution of the thermal boundary layer (Lienhard and Lienhard 2006).

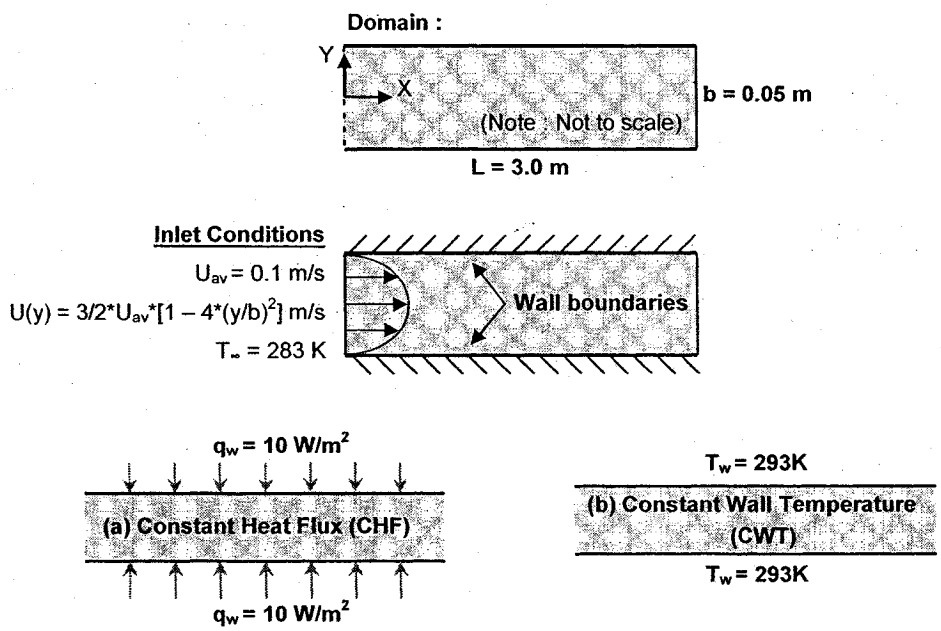

Figure 3.1. Schematic representation of the laminar case studies with (a) constant heat flux or (b) constant wall temperature

The properties of air used in the simulations and the analytical solutions are shown in Table 3.1.

Table 3.1. Laminar forced convection - Material properties of air

Density	**ρ**	1.225 kg/m^3
Dynamic Viscosity	**μ**	1.7894 x 10^{-5} kg/m•s
Thermal Conductivity	**k**	0.0242 W/m•K
Heat Capacity	**c_p**	1006.43 J/kg•K

3.1. REFERENCE TEMPERATURE

The goal of the heat transfer simulations is to find the convective heat transfer coefficient h_{cx} at a particular location x. This relationship is defined as:

$$q_{wx} = h_{cx}\left(T_{wx} - T_f\right) \tag{3.2}$$

where q_{wx} is the heat flux at the wall at x (W/m^2), T_{wx} is the temperature of the wall at x (K), and T_f is a reference temperature within the fluid (K). The actual value used for T_f depends largely on the geometry of the problem. An improperly assigned reference temperature can yield a significant error, as will be shown in the case studies presented. Three reference temperatures are used in a comparison exercise to show the effects on the calculation of h_c: a constant reference temperature (as used in Fluent to report h_c values), the centerline temperature (taken at y=0 on Figure 3.1), and a bulk temperature which is defined as (Lienhard and Lienhard 2006):

$$T_b = \frac{\int_y \rho c_p U T dy}{\dot{m} c_p} \tag{3.3}$$

where ρ is the fluid density (kg/m^3), c_p is the specific heat (J/kg-K), U is the streamwise velocity component (m/s), T is the temperature (K) and $\dot{m}$ is the mass flow rate (kg/s). Equation 3.3 is derived from the rate of flow of enthalpy through a given cross section divided by the rate of heat flow through the same cross section. For the cases shown in this paper, the material properties may be considered constant, and Equation 3.3 can be simplified to the following discrete form:

$$T_b = \frac{\sum_{i=1}^{n}\left(U_i b_i T_i\right)}{U_{av} b} \tag{3.4}$$

where U_i is the velocity of air in the centre of a control volume (CV) (m/s), b_i is the height of the CV (m), T_i the temperature in the CV (K), U_{av} is the velocity averaged over the height of the domain (m/s), b is the height of the domain (m), and the summation extends over the height of the channel.

It can be shown that the energy balance through any given cross-section with a thickness *dx* can be derived to be, (Lienhard and Lienhard 2006):

$$q_w P dx = \dot{m} c_p dT_b$$

which can be rearranged as:

$$\frac{dT_b}{dx} = \frac{q_w P}{\dot{m} c_p} \tag{3.5}$$

where *P* is the heated perimeter (m). Using the conditions specified in Figure 3.1 along with the constant wall heat flux boundary condition, the right hand side of Equation 3.5 becomes a constant value.

$$\frac{dT_b}{dx} = \frac{q_w P}{\dot{m} c_p} = \frac{q_w 2d}{\rho(bd)U_{av} c_p} = \frac{(10)(2)}{(1.225)(0.05)(0.1)(1006.43)} = 3.2444 \text{ K/m} \tag{3.6}$$

where *d* is the depth of the plates. Integrating both sides of Equation 3.6 with respect to *x* results in

$$T_b = 3.2444x + C \tag{3.7}$$

By imposing the boundary condition that at *x*=0m the bulk temperature is equal to the inlet temperature ($T_b = T_\infty = 283$K), Equation 3.7 becomes

$$T_b = 3.2444x + 283 \tag{3.8}$$

Equation 3.8 will be used to verify that bulk temperatures calculated from Fluent data are consistent with the analytical equations.

3.2. Analytical Heat Transfer Coefficients

The heat transfer coefficient may be obtained from analytically derived values of the Nusselt number, which should be constant for thermally developed flow between parallel plates. The values will differ slightly based upon the heating conditions as follows (Lienhard and Lienhard 2006):

$$Nu_{Dh} = \frac{h_c D_h}{k} = \begin{cases} 7.541 & \textit{for fixed plate temperatures} \\ 8.235 & \textit{for fixed wall heat fluxes} \end{cases} \tag{3.9}$$

where D_h is the hydraulic diameter (typically twice the distance between parallel plates) and k is the thermal conductivity of air. The parameters may then be input to yield the following analytical values for h_c:

$$h_c = \frac{Nu_{Dh}k}{D_h} = \begin{cases} 1.825 & \textit{for fixed plate temperatures} \\ 1.993 & \textit{for fixed wall heat fluxes} \end{cases} \quad \text{W/m}^2\text{K} \qquad (3.10)$$

3.3. MESH AND BOUNDARY CONDITIONS

The geometry shown in Figure 3.1 was reproduced with a mesh that was generated from a preliminary mesh sensitivity analysis. Mesh refinement was applied exponentially towards the wall surfaces. A uniformly spaced mesh was used in the streamwise direction. The initial mesh used for the Constant Heat Flux (CHF) and Constant Wall Temperature (CWT) cases had a total of 19,800 cells (33 in the vertical direction, 600 in the horizontal). A portion of the initial mesh is shown in Figure 3.2 below.

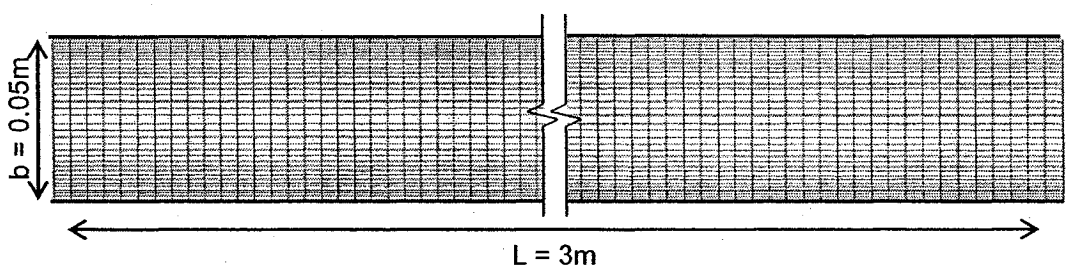

Figure 3.2. Initial mesh used for the CFD simulations.

The boundary conditions for the simulations were input as shown in Figure 3.3 and Figure 3.4. A sample set of the *Fluent* solution parameters and model information for laminar forced convection are provided in Appendix A.

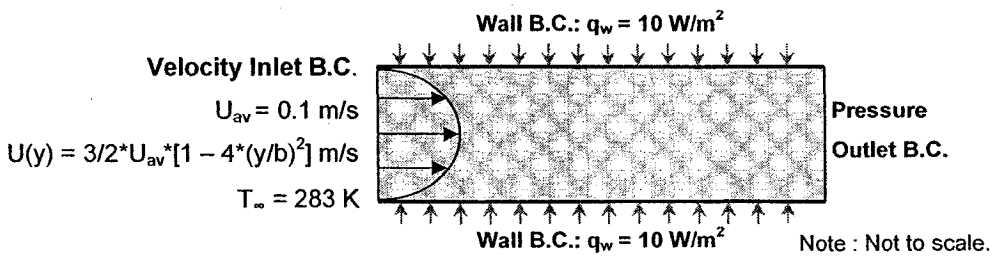

Figure 3.3. Boundary Conditions (B.C.) – CHF Case

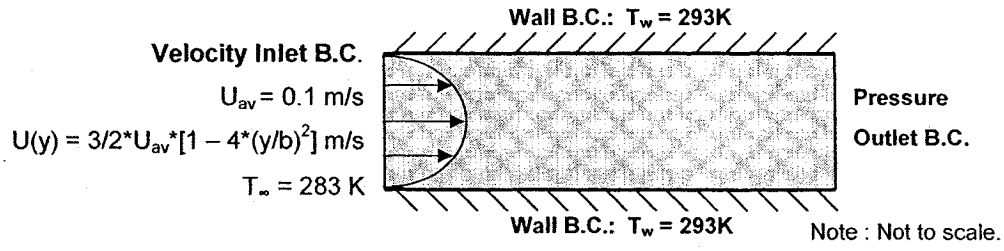

Figure 3.4. Boundary Conditions (B.C.) – CWT Case

The velocity profile used as the inlet condition is a parabolic profile commonly used to describe the flow between parallel plates (e.g. Lienhard and Lienhard 2006). When comparing the inlet and outlet profiles from the simulation results, the difference in velocity at a given height is on the order of 10^{-4} m/s. Therefore, it can be assumed that the flow is indeed already fully developed at the inlet.

The flow field was initialized to the inlet conditions (described in Figure 3.4). The simulations were iterated until a scaled residual of 10^{-7} (Fluent Inc. 2003) was achieved for all the solution parameters involved.

3.4. RESULTS

Once the simulations were completed, the bulk temperatures were calculated with Equation 3.4 using the cell temperature and velocity data. For the case of constant heat flux, the simulation data can be compared to the analytical equation derived in Equation 3.8. The results from *Fluent* are plotted in Figure 3.5, and the resulting trendline equation is very close to the expected equation.

Analytical Bulk Temperatures: $T_b = 3.2444x + 283$

Fluent Bulk Temperatures: $T_b = 3.2423x + 283$

The error increases slightly along the length of the plate. After 3m, the difference between the analytical and *Fluent* bulk temperatures is on the order of 10^{-3} %.

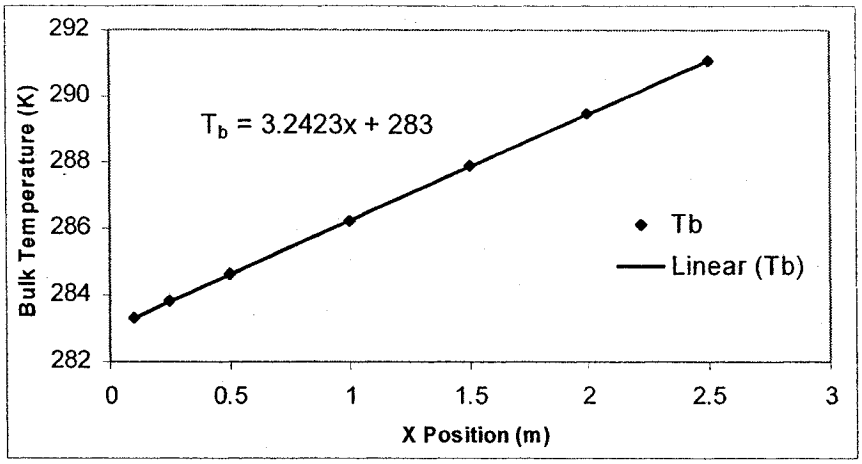

Figure 3.5. Bulk temperatures calculated from Fluent output data

The convective heat transfer coefficients were calculated with Equation 3.2, using the three different fluid reference temperatures previously mentioned. The parameters used to solve Equation 3.2 are outlined in Table 3.2 below.

The convective heat transfer coefficients calculated from the simulation data are shown below in Figure 3.6 and Figure 3.7. The results indicate that the temperature value used to describe the fluid (T_f from Equation 3.2) can have a significant effect on the result. The chosen reference temperature must match the one used in the derivation of the equation or correlation used for comparison. The reported values in *Fluent* are calculated based on a user specified constant reference value, which results in non-constant convective coefficients after the flow is thermally developed (Fluent Inc. 2003). Correlations that were developed using any other fluid temperature as a reference will not match the results from *Fluent*, which could lead to the incorrect conclusion that CFD is not suitable for the calculation of convective heat transfer coefficients. Therefore, care must be taken on which values are used when reporting information from *Fluent*.

The convective coefficients calculated from the centerline temperatures are more consistent with the expected trend, but they under-predict the h_c values by about 20% for the CHF solution and by about 24% for the CWT solution.

The bulk temperature appeared to be the reference temperature for which the analytical equations were derived, resulting in an error margin of less than 0.5% for both cases (after thermal development). Since the bulk temperature calculation is dependent on the grid used, a grid sensitivity and discretization error analysis was performed to determine what the grid independent solution would be.

Table 3.2. Convective heat transfer coefficient solution parameters

	CHF – Case (a)	CWT – Case (b)
$q_w(x)$	q_w = 10 W/m^2	$q_w(x)$ → From Fluent
$T_w(x)$	$T_W(x)$ → From Fluent	T_w = 293 K
$T_f(x)$	$h_{cx} = \frac{q_w(x)}{T_w(x) - T_f(x)}$	
$T_f(x) = T_{ref}$ = 283 K (Constant value specified in Fluent (Fluent Inc. 2003))	$h_{cRef}(x) = \frac{10}{T_w(x) - 283}$	$h_{cRef}(x) = \frac{q_w(x)}{293 - 283}$
$T_f(x) = T_c(x)$ (Horizontal temperature profile at the center of the flow (y = 0))	$h_{cc}(x) = \frac{10}{T_w(x) - T_c(x)}$	$h_{cc}(x) = \frac{q_w(x)}{293 - T_c(x)}$
$T_f(x) = T_b(x)$ (Horizontal bulk temperature profile at different x positions from the Fluent Data)	$h_{cb}(x) = \frac{10}{T_w(x) - T_b(x)}$	$h_{cb}(x) = \frac{q_w(x)}{293 - T_b(x)}$

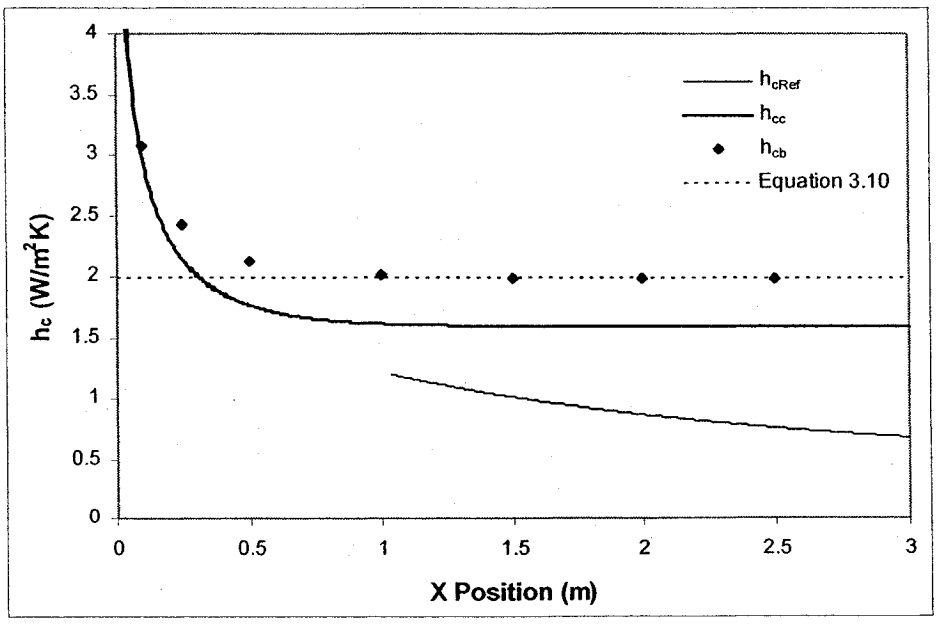

Figure 3.6. Convective heat transfer coefficients for constant wall heat flux

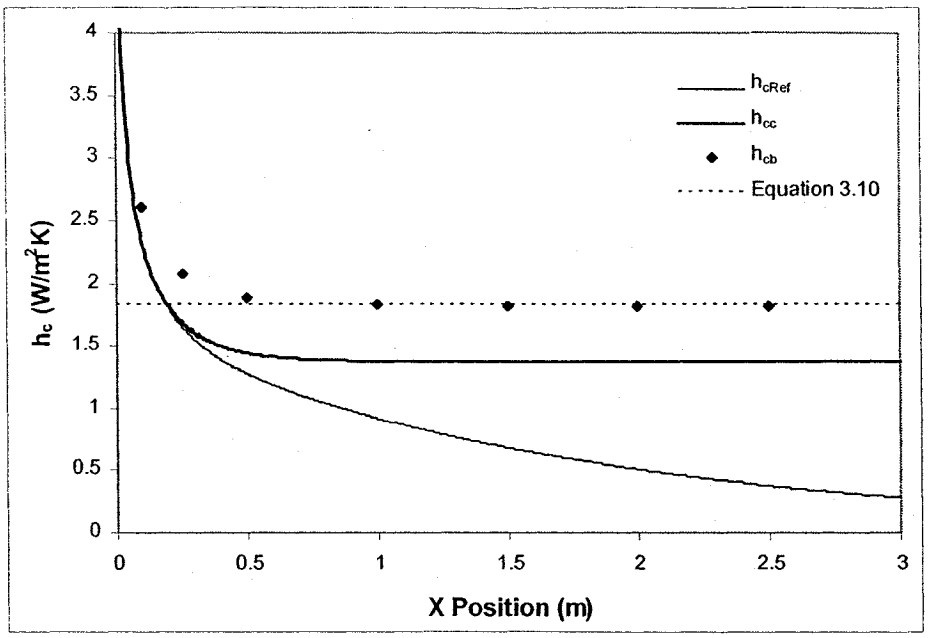

Figure 3.7. Convective heat transfer coefficients for constant wall temperature

3.5. GRID SENSITIVITY ANALYSIS

For the purpose of the grid sensitivity analysis, the calculated convective heat transfer coefficients are compared for different grid densities at x = 2.5 m, which was selected since it is located in the thermally developed region of the flow. The process was repeated for both the CHF and CWT cases to compare the grid dependency for the two different boundary conditions. Only the coefficients calculated from the bulk temperature are part of this comparison.

The initial grid used for the simulations had a total of 19,800 cells. It was decided to proceed with several coarser grids and one finer mesh. The details of the different meshes are presented in Table 3.3. The second column of the table represents the mesh used for the simulations from the previous section. The notation ϕ_h is adopted to describe the solution for the finest mesh. The subsequent meshes are all notated with respect to the finest mesh. The next grid size has cell dimensions doubled in both directions, hence the notation ϕ_{2h}.

Table 3.3. Mesh Dimensions

	ϕ_h (80400)	ϕ_{2h} (19800)*	ϕ_{4h} (5100)	ϕ_{8h} (1200)	ϕ_{16h} (300)
Number of cells in the Y Direction	67	33	17	8	4
Number of cells in the X Direction	1200	600	300	150	75
Smallest cell height (m)	4.202E-04	8.749E-04	1.775E-03	3.948E-03	9.147E-03
Smallest cell width (m)	0.0025	0.005	0.01	0.02	0.04
Total number of cells	80400	19800	5100	1200	300

*** Original mesh**

It can be shown (Ferziger and Peric 1997) that the discretization error of a grid is approximately

$$\varepsilon_h^d \approx \frac{\phi_h - \phi_{2h}}{2^a - 1} \tag{3.11}$$

where *a* is the order of the scheme and is given by

$$a = \frac{\log\left(\frac{\phi_{2h} - \phi_{4h}}{\phi_h - \phi_{2h}}\right)}{\log(2)} \tag{3.12}$$

In both equations, the "2" refers to the increase in resolution of the mesh. From Equation 3.12, it follows that a minimum of three meshes are required to determine the discretization error. In order to prevent a calculation error from the logarithm of a negative number, the three solutions must be monotonically converging (Ferziger and Peric, 2002).

The theory of Richardson Extrapolation states that the solution from the finest mesh can be added to the discretization error found in Equation 3.11 to attain an approximate grid independent solution. In equation form, this can be stated as:

$$\Phi = \phi_h + \varepsilon_h^d \tag{3.13}$$

where Φ is the grid independent solution. The results from the grid sensitivity analysis are shown in Table 3.4 and plotted below in Figure 3.8 and Figure 3.9.

Table 3.4. Discretization error and Richardson Extrapolation Results

	Order of the scheme a	Discretization Error ε_h^d (W/m^{2}K)	Finest mesh solution ϕ_h (W/m^{2}K)	Richardson Solution Φ (W/m^{2}K)	Analytical solution h_c (W/m^{2}K)
CHF	1.460	2.297×10^{-3}	1.990578	1.992875	1.992875
CWT	1.858	1.001×10^{-3}	1.824089	1.825090	1.824922

The grid sensitivity analysis results indicate that the mesh used to calculate the convective heat transfer coefficients from Section 3.4 was accurate to below 1% relative error for both cases.

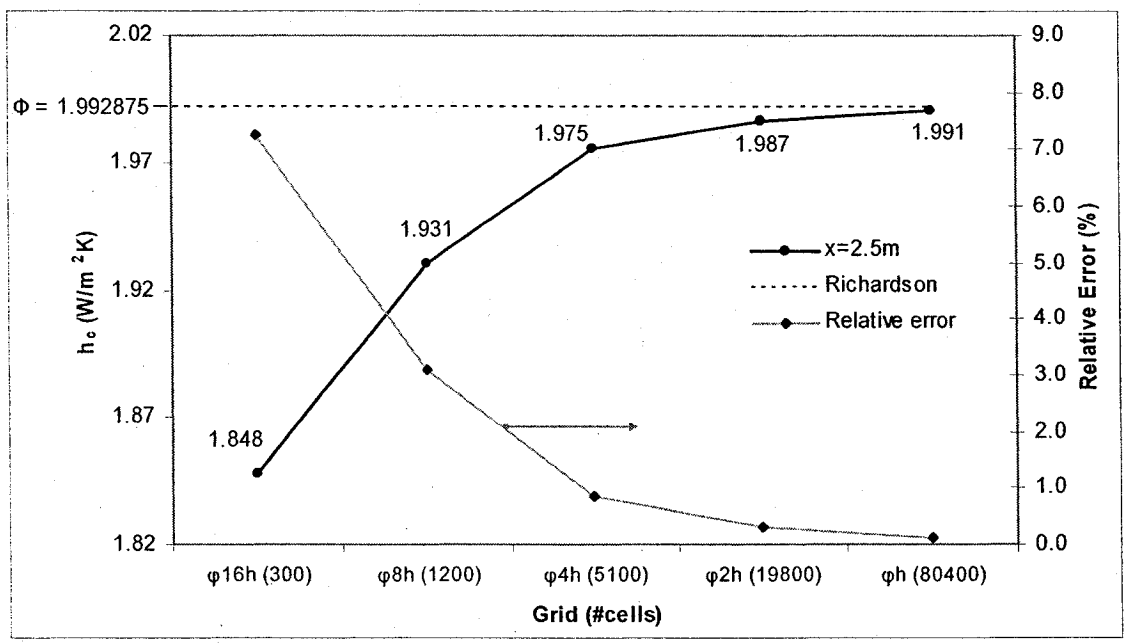

Figure 3.8. Grid convergence of the heat transfer coefficient for constant heat flux and relative error compared with Richardson solution

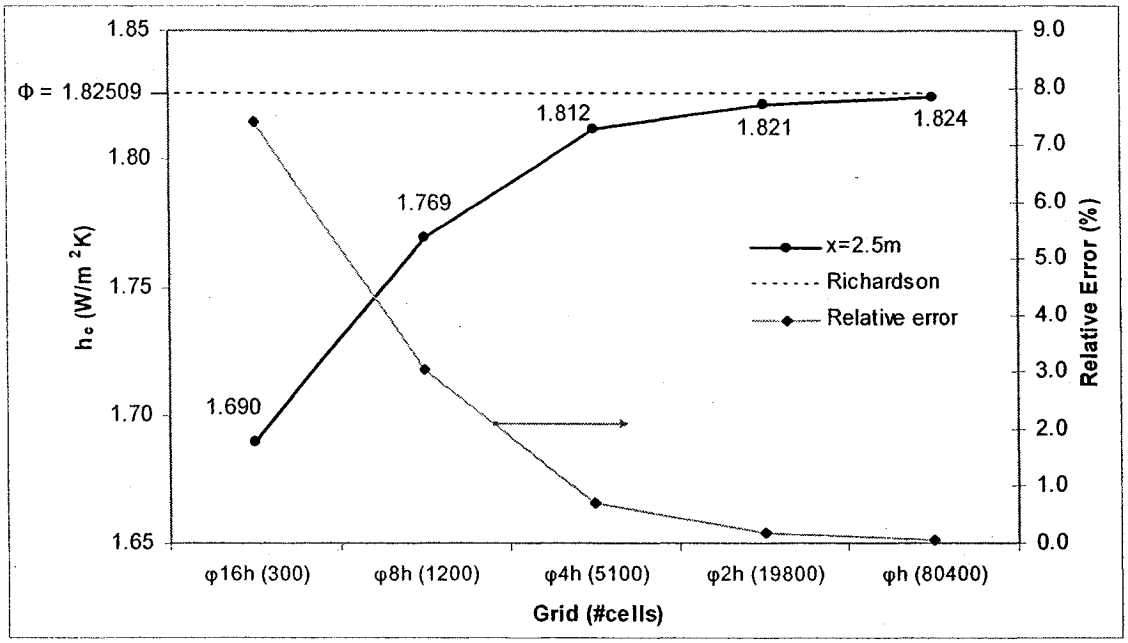

Figure 3.9. Grid convergence of the heat transfer coefficient for constant wall temperature and relative error compared with Richardson solution

Note that in this case the actual order of the scheme (*a*) is higher than the discretization scheme used in the Fluent solver (shown in Appendix A).

3.6. Discussion and Conclusions

In this chapter, a verification exercise was performed by comparing the computed convective heat transfer coefficients (h_c) for laminar air flow between parallel plates by Computational Fluid Dynamics to analytical solutions. An initial mesh was selected based on a preliminary grid sensitivity analysis. The CFD simulations were performed for constant wall temperature and constant heat flux conditions. The importance of a correct reference temperature was confirmed.

The CFD results showed a good agreement with the analytical solutions, indicating a proper performance of the CFD code, at least for the cases studied.

Finally, a grid sensitivity analysis was performed on the mesh for both wall boundary conditions. The discretization error for h_c was calculated at a given location on the plate and Richardson extrapolation was used to compute the grid independent solution. The resulting h_c values had good agreement with analytical values from

literature. The percentage error between the analytical and the grid independent solutions for h_c is on the order of 10^{-2} %.

The laminar viscous flow and heat transfer model for CFD has been confirmed to be accurate for the cases studied. The next chapter will focus on turbulent forced convection cases and additional CFD model validation.

CHAPTER 4. TURBULENT FORCED CONVECTION

This chapter is a comparative study of heat transfer coefficients calculated using different turbulence models implemented in *Fluent*. The validation methodology is presented, followed by a brief overview of wall function theory. Note that the magnitudes of the turbulence quantities, such as the turbulent kinetic energy and the turbulence dissipation rate, are not considered in this study.

4.1. VALIDATION TECHNIQUE

In the interest of validating the turbulence models for forced convection within *Fluent*, it was necessary to obtain experimental data to use as a basis for comparison. While experiments have been performed in this area, it is often difficult to establish whether the simulation truly matches all of the experimental parameters. However, one area of research that has been focused on extensively in the past is the universal "law-of-the-wall" that describes turbulent boundary layer flow. Through analytical derivations of equations and experimental data fitting, the boundary layer velocity profile (and temperature profile, if applicable) has been subdivided into three regions: the laminar sublayer, the buffer region, and log-law region (Chen and Jaw 1998, Blocken 2004). Semi-empirical relationships have been developed for the laminar sublayer and log-law regions, and empirical equations exist for the buffer region as well (e.g. Spalding 1961). The (semi-) empirical equations will be used to validate the simulation results from *Fluent*.

4.2. MESH AND BOUNDARY CONDITIONS

As explained in Section 2.3.3, the Low-Re modelling approach recommends that the first mesh cell has a dimensionless height of $y^+ \approx 1$, which means that it is submerged in the laminar sublayer (Fluent Inc. 2003). For simulations with Wall Functions (WF), a y^+ between 30 and 60 is recommended. The y^+ value is based on the flow conditions at the surface (see Equation 4.1) and therefore requires an iterative procedure to properly size the first cell. After a number of mesh adjustments, the mesh fulfilled the requirements for Low-Re modelling, and is shown below in Figure 4.1. The mesh used for wall function cases is shown in Figure 4.2. In both cases, an exponential relationship was used to mesh the vertical direction and a uniform spacing was used for the horizontal direction. The grid dimensions are shown in Table 4.1.

Table 4.1. Mesh parameters and dimensions – forced convection case

Mesh	#Cells in X-direction	#Cells in Y-direction	Smallest Cell Width	Smallest Cell Height	Total number of cells
Low-Re	500	100	0.01 m	1.285×10^{-3} m	50000
WF	100	13	0.05 m	4.653×10^{-2} m	1300

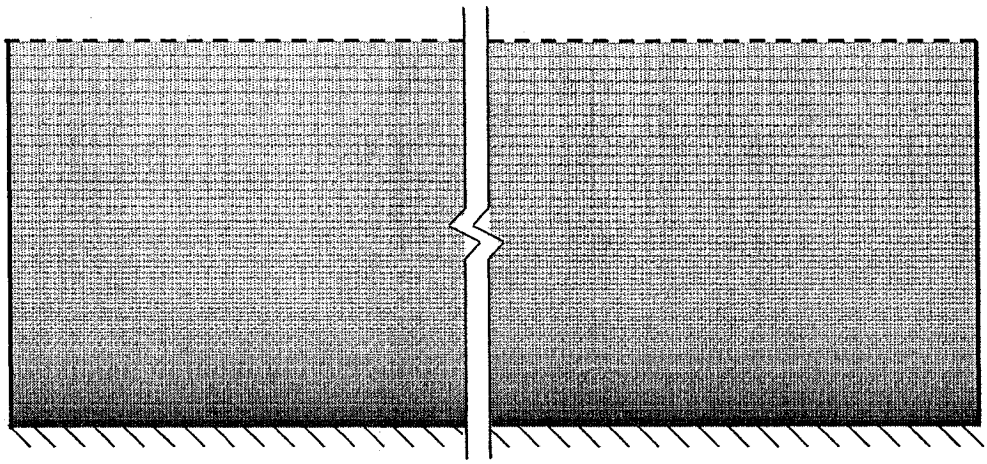

Figure 4.1. Mesh used for simulations with low-Reynolds-number modelling

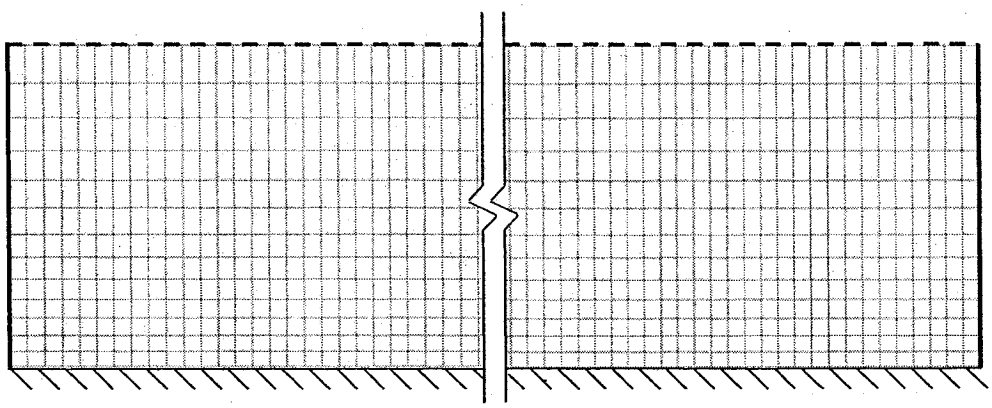

Figure 4.2. Mesh used for simulations with wall functions

Note that the meshes for the Low-Re modelling and wall function cases can have the same spacing near the symmetry boundary, since the boundary layer resolution is not affected by the top region of the domain. In addition, the horizontal spacing of the cells can be the same for both types of meshes, but for the Low-Re mesh a smaller

spacing was selected to have an aspect ratio closer to 1.0 near the wall surface. Aspect ratio is the ratio of the cell height to the cell width.

The domain used to represent the fluid flow over a flat plate is shown in Figure 4.3. The boundary condition (BC) for the top of the domain was chosen to be a symmetry condition in order to reduce the computation time of the simulation. If a pressure outlet BC is chosen instead of symmetry, it can lead to convergence problems when modelling turbulence. The height of the domain was selected to be high enough to reduce the influence of the symmetry condition on the boundary layer.

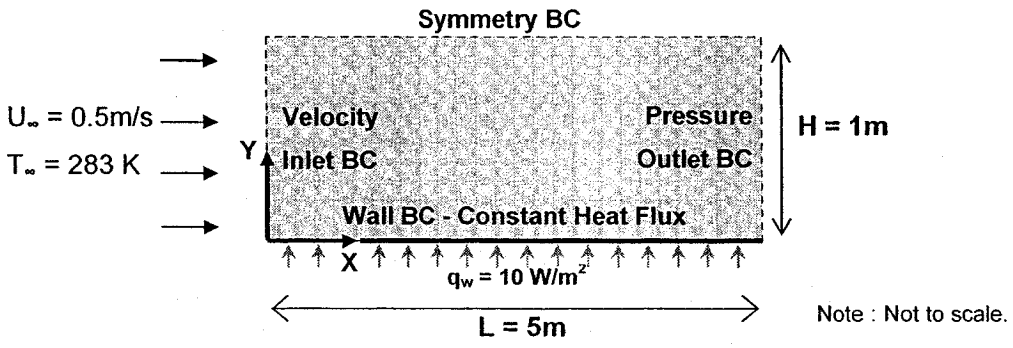

Figure 4.3. Computational domain and boundary conditions (BC)

The simulations were all initialized with a uniform velocity profile of 0.5 m/s. The simulations were iterated until the scaled residuals for all parameters were below 10^{-7}. The outlet velocity profile and turbulence conditions were then used as the new inlet conditions and the simulation was repeated. The thermal conditions were not saved from one simulation to the next, and consequently the flow was always thermally developing from the start of the domain. This procedure was continued until the inlet and outlet velocity profiles were approximately the same, resulting in a fully developed flow profile. The original uniform velocity profile ensured that the bulk velocity was 0.5 m/s for all cases. A sample of the *Fluent* solution parameters for turbulent forced convection is provided in Appendix A. Note that the properties of air used in the simulations were the same as those for laminar forced convection, shown in Table 3.1.

4.3. RESULTS

The simulation results are compared at x = 4.5m for all cases. The location was selected due to its position within the thermally developed region. Simulations were performed with the following turbulence models with Low-Re Modelling:

1) *Spalart-Allmaras Model*
2) *Standard k-ε Model*
3) *RNG k-ε Model*
4) *Realizable k-ε Model*
5) *Standard k-ω Model*
6) *SST k-ω Model*
7) *Reynolds Stress Model (RSM)*

Simulations were performed with the following models with Wall Functions (WF):

1) *Standard k-ε Model*
2) *Standard k-ω Model*

Note that the *Standard k-ω Model* will automatically interpret whether Low-Re or WF will be used based on the y^+ of the first cell. The default settings for each model were used for all cases unless otherwise specified.

The calculated dimensionless velocity and temperature profiles are shown in Figure 4.4 and Figure 4.5, respectively. The convective heat transfer coefficient results are shown in Figure 4.6.

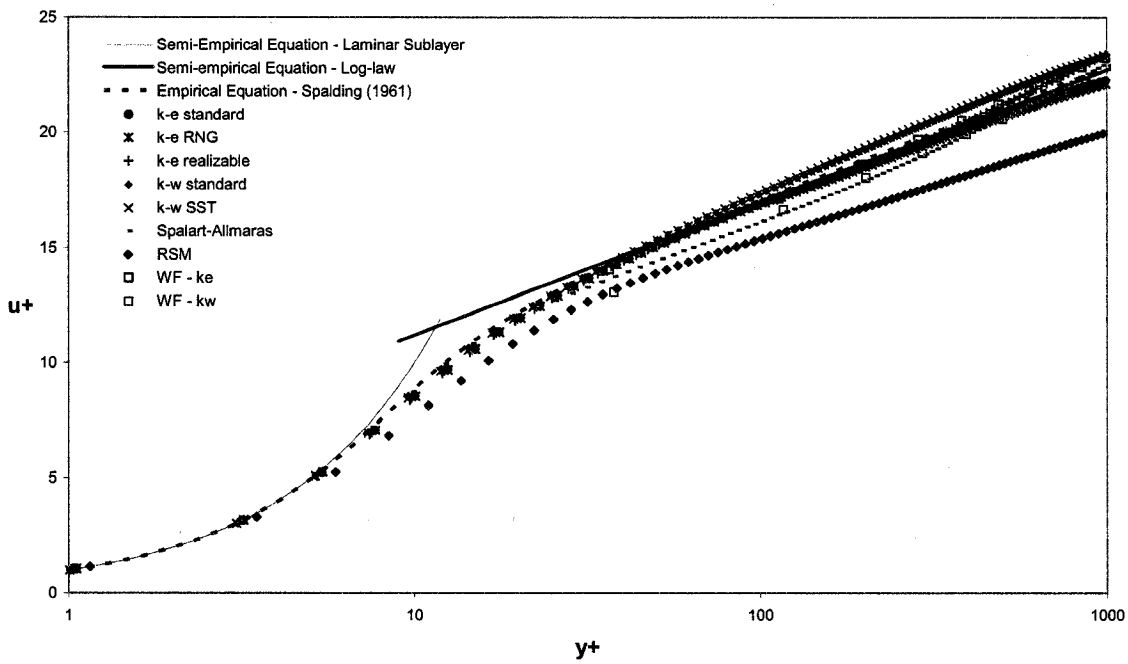

Figure 4.4. Dimensionless velocity profile results for the turbulent simulations

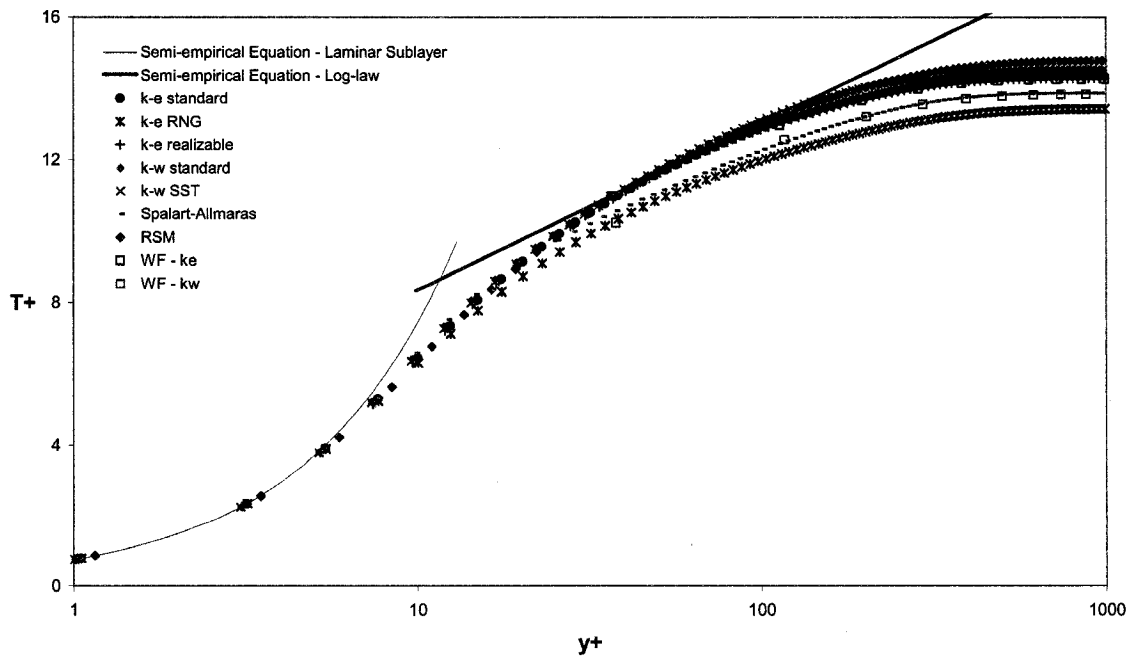

Figure 4.5. Dimensionless temperature profile results for the turbulent simulations

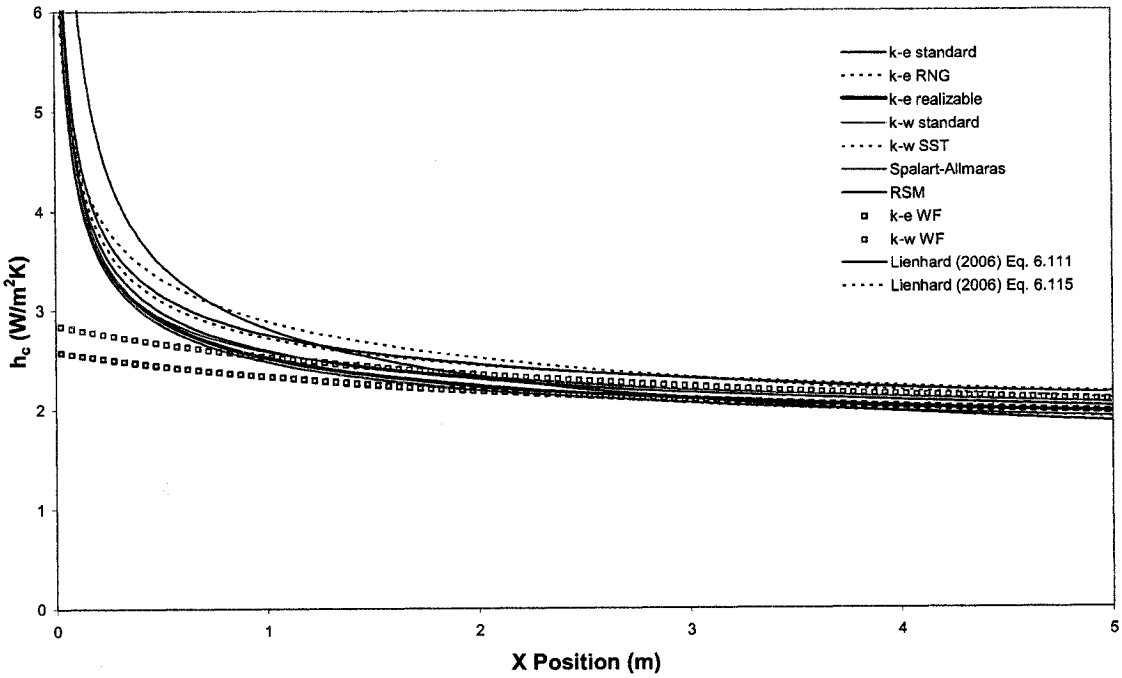

Figure 4.6. Convective heat transfer coefficient results for the turbulent simulations

4.4. DISCUSSION AND CONCLUSIONS

The velocity profiles shown in Figure 4.4 indicate a good agreement with the "universal" law-of-the-wall relationships and the "universal" Spalding curve, which were both developed based on experimental data. The laminar sublayer and the log-law region are well defined for all of the turbulence models, though some models (RSM) tend to under predict the velocity near the upper boundary (for large values of y^+). This can be explained by the fact that the law-of-the-wall relationship ceases to be valid beyond a certain point (roughly $y^+ > 500$) (Blocken 2004).

The temperature profiles in Figure 4.5 are also consistent with the expected boundary layer profile, though at upper regions of y^+ (>200) the curves begin to diverge from the log-law equation. The same remark can be made for the region beyond $y^+ > 500$ where law-of-the-wall theory begins to fail.

The correlations for heat transfer are shown in red on Figure 4.6. The heat transfer coefficients are consistent between the turbulence models and the correlations, including the solutions using wall functions. However, in the thermally developing region (approximately 0m < x < 1m), the wall function solutions differ from the other curves.

The result is an important underprediction of heat transfer for cases where there is thermally developing flow. This is due to the fact that the wall function approach is not valid under these conditions.

Now that laminar and turbulent forced convection have been simulated successfully with CFD, the next chapter will focus on natural convection simulations and results.

CHAPTER 5. NATURAL CONVECTION

In addition to laminar and turbulent forced convection, it was desired to study the accuracy of convective heat transfer coefficients calculated by CFD for natural convection cases. While laminar natural convection cases exist, only turbulent cases were studied in order to limit the scope of the work for this chapter. The definition of turbulence for natural convection has been previously described in Section 2.2.2. In general, the same methodology was used as in Chapters 3 and 4. The validation technique will be described, the computational domain and mesh will be outlined, and some issues concerning convergence in CFD simulations will be explained.

5.1. VALIDATION TECHNIQUE

Validation for natural convection models is difficult to find in literature. Often, there is not enough information to properly simulate an experiment. In addition, experiments require extensive planning and expensive equipment to obtain results that can be used for validation. Some experiments in natural convection were previously discussed in Section 2.2.2 of the literature review. The experiment of Tian and Karayiannis (2000) was selected to validate the natural convection simulations performed in this chapter. The experiment itself was performed with a high level accuracy, and the experimental set-up is shown below in Figure 5.1.

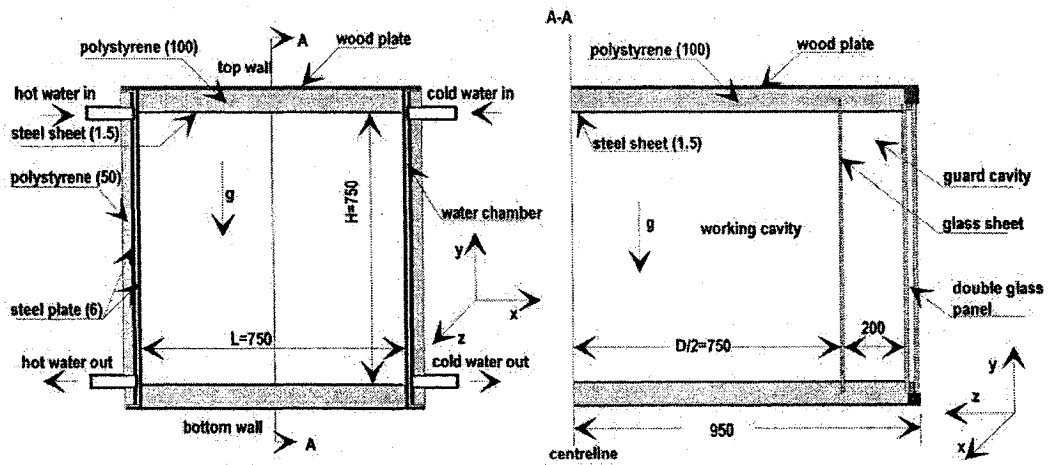

(a) Section across thermally controlled walls

(b) Section across insulated guard wall

Figure 5.1. Experimental set-up by Tian and Karayiannis, all dimensions are in mm. Figure taken from Tian and Karayiannis (2000).

The experimental chamber shown above had two vertical isothermal walls maintained respectively at 50 °C (left hand side) and 10 °C (right hand side). The temperature difference results in a natural convection loop that circulates in a clockwise direction at a given cross-section. The four surfaces of the chamber were insulated to reduce the heat flux through the walls. The experiment was designed to result in purely two-dimensional air movement (in the X-Y plane), which the authors verified in their results. Consequently, only two-dimensional simulations were performed of the cross-section shown above in Figure 5.1(a).

The results from the experiment are used in this chapter in several locations, and are referred to as "Tian and Karayiannis". All results are taken from the paper outlining the experiment.

In addition to the experimental validation, the convective heat transfer coefficients will be compared to an empirical correlation that satisfies the simulation parameters. The convective heat transfer coefficients calculated from the simulations are compared to a correlation developed by Churchill and Chu (1975). This correlation relates Nusselt numbers for a wide range of Rayleigh and Prandtl numbers. The correlation is valid for all Prandtl numbers and for Rayleigh numbers between 10^{-1} and 10^{11}. The reference temperature for the correlation is the free stream air temperature at the edge of the thermal boundary layer.

$$Nu_L = 0.68 + \frac{0.67 Ra_L^{0.25}}{\left[1 + \left(\frac{0.492}{\mathrm{Pr}}\right)^{9/16}\right]^{4/9}} \tag{5.1}$$

where L signifies the characteristic length of the vertical plate being analyzed. The percentage error for the correlation in Equation 5.1 is approximately 5.5% for cases with Rayleigh numbers larger than 10^5 (Lienhard and Lienhard 2006). The Nusselt number found from Equation 5.1 may then be used in a calculation to determine the average convective heat transfer coefficient.

$$h_{cL} = \frac{Nu_L k}{L} \tag{5.2}$$

where h_{cL} is the plate-averaged convective heat transfer coefficient (W/m^{2}K), k is the thermal conductivity of air (=0.026341 W/m-K @ 30°C), and L is the length of the plate (= 0.75 m). Given that Ra = 1.58x10^9 and Pr = 0.7138 for the experiment and

simulations, the Nusselt number was calculated to be 103.27, and the resulting h_{cL} value was found to be 3.627 W/m^{2}K.

5.2. Additional Information for Natural Convection

The basic theory of natural convection has been described previously in Section 2.2.2, including the definition of turbulent natural convection, the Rayleigh number, and other pertinent information. The equations and terms introduced in Section 2.3.3 regarding near-wall modelling are also pertinent to this chapter.

The temperature values for the cases studied in this chapter are expressed in dimensionless terms to facilitate comparison between simulation results and experimental results. The dimensionless temperature can be calculated using the following equation:

$$T^* = \frac{T - T_{COLD}}{T_{HOT} - T_{COLD}} \tag{5.3}$$

where T^* is the dimensionless temperature, T is the air temperature at a certain point in the chamber volume or at surface points of the top or bottom walls (K), and T_{HOT} and T_{COLD} are the previously defined hot and cold temperatures of the vertical walls (K). Similarly, the dimensions of the experiment may be expressed in dimensionless terms using the following equations:

$$X = \frac{x}{L} \tag{5.4}$$

$$Y = \frac{y}{H} \tag{5.5}$$

where X is the dimensionless width, x is the horizontal position (m), L is the width of the chamber (=0.75m for this experiment), Y is the dimensionless height, y is the vertical position (m), and H is the height of the chamber (=0.75m for this experiment). Note that the dimensionless width and height in Equations 5.4 and 5.5 are not to be confused with the dimensionless parameters that were previously described in Section 2.3.3.

5.3. Mesh and Boundary Conditions

The mesh that was selected to represent the computational domain was based on a series of test simulations that formed a grid sensitivity analysis. As will be explained later, the mesh used in natural convection simulations has a very important influence on the convergence of the simulation. This will be explained further in Section

5.4. The end result of the grid sensitivity analysis was a mesh that used a bell-shaped distribution of cells that varies from very fine at the wall surfaces to coarse in the center of the domain. The term "bell-shaped" refers to the magnitude of the cell size increments, which is very fine near the walls and gradually becomes coarse at the center of the domain. The mesh selected for the simulations is shown below in Figure 5.2.

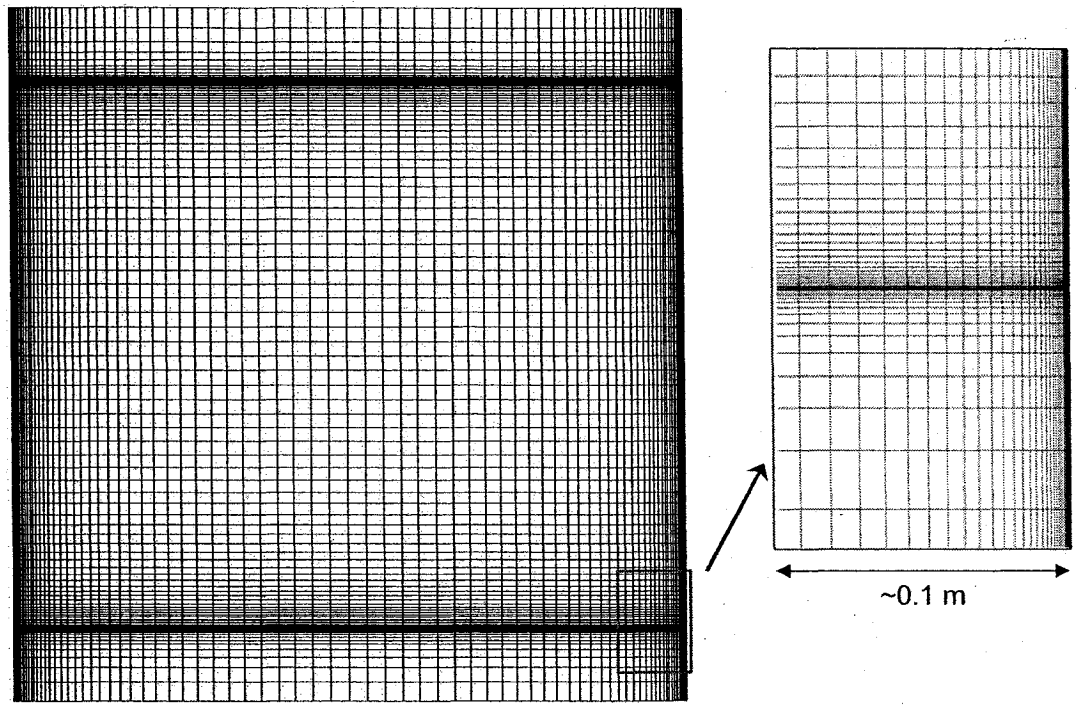

Figure 5.2. Mesh used for the natural convection simulations

The cells adjacent to the wall surfaces had an average dimensionless height of $y^+ \approx 2$. Consequently, the simulations were considered to be in the Low-Re Modelling region previously described in Section 2.3.3.

The computational domain, shown below in Figure 5.3, was selected to represent the experiment of Tian and Karayiannis (2000) as closely as possible. The vertical walls of the chamber were Constant Wall Temperature (CWT) boundary conditions and the horizontal walls were designed to replicate the experimental conditions, which are described in further detail below.

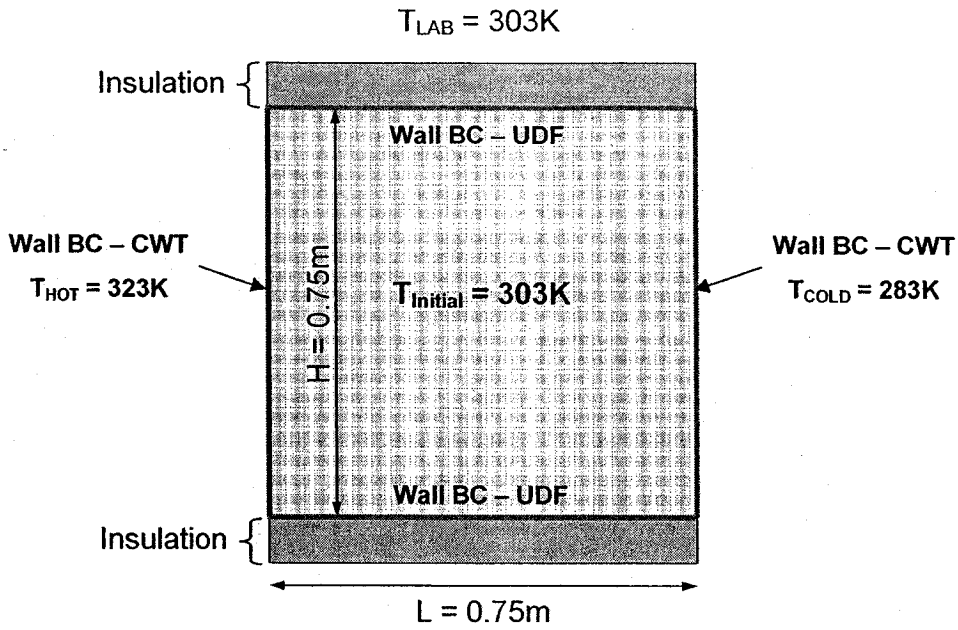

Figure 5.3. Computational Domain and Boundary Conditions (BC) for the natural convection simulations

The temperatures of the hot and cold surfaces were set to be constant temperature boundary conditions throughout the simulations. The top and bottom surfaces of the Tian and Karayiannis experiment, shown in green in Figure 5.3, proved to be difficult to simulate accurately. The authors had designed the experiment to reduce the heat flux through the horizontal surfaces by making the lab temperature equal to the average temperature inside the chamber. The result is effectively a net heat flux across the top and bottom surfaces equal to zero. In theory such a boundary condition can be implemented in *Fluent* rather easily. However, the four primary surfaces of the chamber were covered in steel plates of unknown material properties, and the connection detail illustrated below in Figure 5.4 was not clearly represented in the paper. Whether the steel plates from the vertical (heated) walls are in contact with the horizontal plates or not, the end result would be a rather different temperature profile at the surface. Convection and radiation would no longer be the main driving influences for the surface temperature, it would be the highly conductive steel in contact with the hot and cold surfaces. Also, it was unknown to what extent radiation itself would have an impact on the top and bottom surfaces of the chamber.

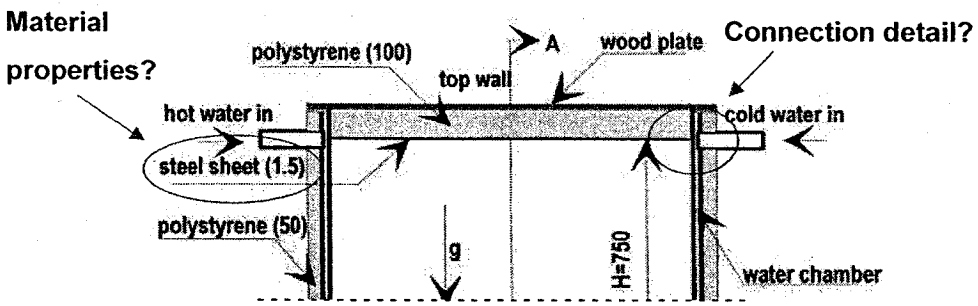

Figure 5.4. Boundary condition unknowns. Figure taken from Tian and Karayiannis (2000).

The various methods that were explored to model the horizontal surfaces of the chamber are shown below in Figure 5.5.

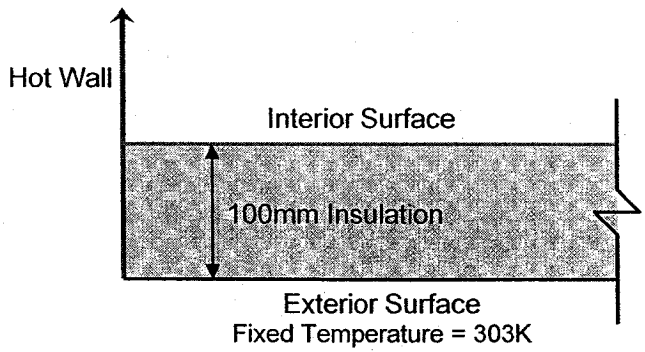

Boundary Conditions Considered:

1) **No radiation, no steel on interior surface**
2) **Radiation, no steel on interior surface**
3) **Radiation, with steel plate on interior surface**
4) **Experimental temperature profiles applied to interior surface**

Figure 5.5. Horizontal surface boundary conditions

Only the lower boundary condition of the chamber is shown in Figure 5.5, but the boundary conditions were always symmetrically applied to the top and bottom surfaces. The first three methods were similar in that the temperature was fixed to 303K at the exterior surface, which corresponds to the temperature of the laboratory and the average temperature within the chamber. The primary difference between each method was the way that the interior surface was modelled. For Case #1, no radiation was modelled within the chamber, and therefore the interior top and bottom surfaces would have been calculated based solely on the conduction through the insulation and convection within

the boundary layer. In Case #2, the effects of radiation were included such that the hot and cold vertical walls would have an impact on the horizontal surface temperatures. The third case added the steel plates described earlier, which were set to be in contact with the hot and cold surfaces. The material properties of the steel were approximated. The fourth case was for a user-defined temperature profile that was created to match the experimentally measured temperatures for the horizontal surfaces. The Standard k-ω model was used for all four cases for consistency, and the discrete transfer radiation model described in Section 2.3.5 was used when radiation was included in the simulations.

The material properties used in the simulations for air, polystyrene (used for the insulated walls), and steel are shown below in Table 5.1.

Table 5.1. Natural convection - Material properties

Property		Air	Polystyrene	Steel
Density (kg/m^3)	ρ	1.1649	15	8030
Dynamic Viscosity (kg/m•s)	μ	1.868x 10^{-5}	N/A	N/A
Thermal Conductivity (W/m•K)	k	0.026341	0.037	16.27
Heat Capacity (J/kg•K)	c_p	1006.5	1500	502.48
Emissivity (-)	ε	N/A	N/A	0.9
Thermal Expansion Coefficient (at 303K) (K^{-1})	β	0.0033	N/A	N/A

5.4. Convergence in Natural Convection Simulations

A number of simulations were performed before any natural convection results could be generated. First of all, numerous meshes were used in a preliminary grid sensitivity analysis until an appropriate distribution of cells was found. Due to the varying velocities found along the wall surfaces and the desire for a structured mesh, it was difficult to maintain an appropriate y^+ value along the entire surface of all four walls. Several cell distribution sizes were attempted; exponential gradients, uniform cell sizes, and bell-shaped gradients were used in test simulations. The bell-shaped distribution was selected because of the necessity for a very fine mesh at the surface, which allowed for coarse cells in the center of the domain where the velocities were expected to be very low. Despite the significant work in selecting a proper mesh for the simulations, convergence issues were encountered for the natural convection simulations.

The first observation made when simulating turbulent natural convection was that there are almost invariably convergence issues with the solution. For example, a steady-state simulation was performed using the Standard k-ω model for the experimental conditions outlined earlier. When the simulation was run for 1000 iterations, the scaled residuals resulted in the graph shown in Figure 5.6.

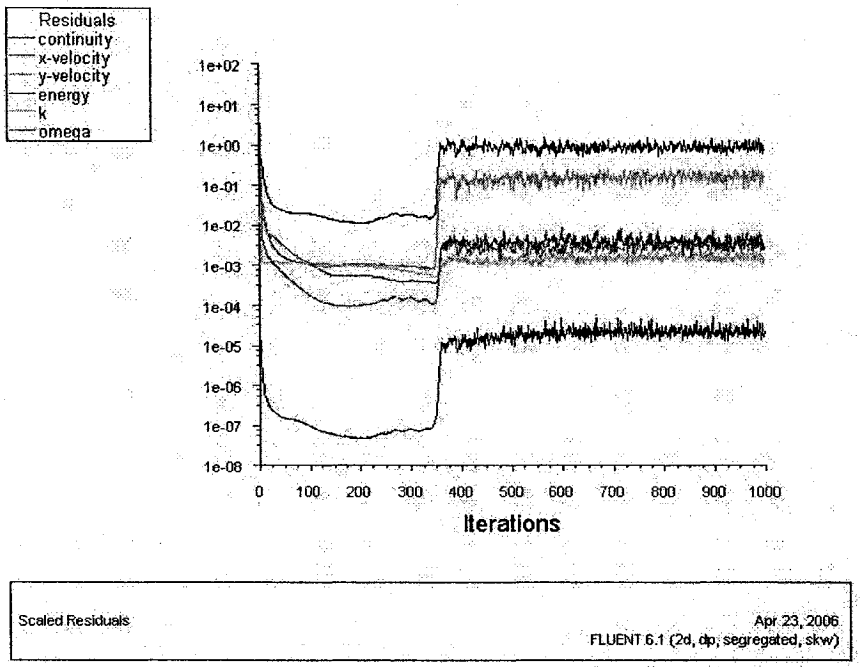

Figure 5.6. Scaled residuals demonstrating convergence problems

The graph shown in Figure 5.6 clearly illustrates a trend that does not monotonically converge. This trend has been documented in CFD literature, in particular for turbulent natural convection (Fluent Inc. 2003).

In Section 2.2.2, natural convection was defined as turbulent (or possibly transitional) when the Rayleigh number of the problem is above 10^8. The experiment shown in Figure 5.1 has a Rayleigh number of 1.58×10^9, which indicates that it is well within the turbulent regime (Tian and Karayiannis 2000). In general, the natural convection simulations should have a steady-state solution where the system reaches equilibrium. However, in practice, the numerical results tend to have no particular solution, which results in residuals such as the ones shown in Figure 5.6. For a given iteration, the CFD code will obtain a solution, but, on the next iteration, the result will be slightly different preventing any stable steady-state solution. In order to correct this issue, a specific solution procedure must be followed to obtain a stable solution.

The first step to reaching a converged (or stable) solution is to run a steady-state simulation of the turbulent problem, but with a Rayleigh number below the turbulence threshold. The easiest way to accomplish this task is by lowering the gravitational constant by one or two orders of magnitude (Fluent Inc., 2003). This process is described below in Figure 5.7.

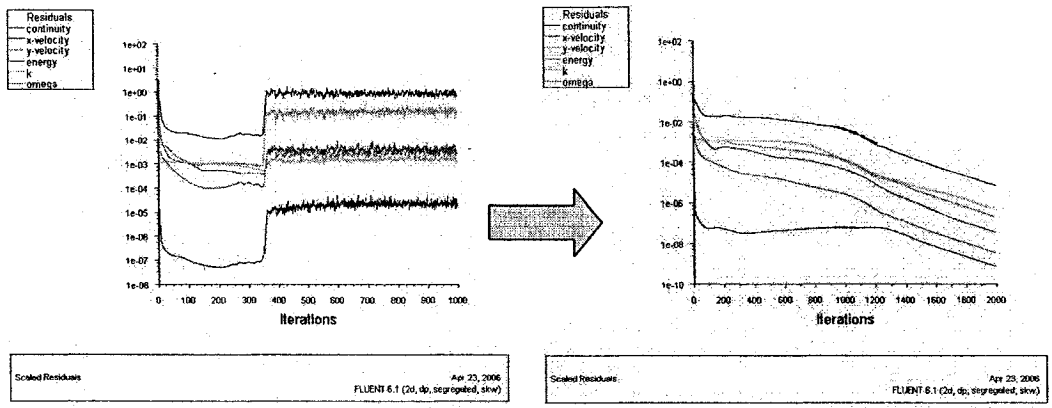

Ra = 1.52 x 10^9
(gravity = 9.81 m/s^2)

Ra = 1.52 x 10^8
(gravity = 0.981 m/s^2)

Figure 5.7. Turbulent natural convection solution procedure

Note that the simulation parameters for the left and right simulations in Figure 5.7 are identical in all aspects except for the gravitational constant. This clearly indicates that there is a well-defined threshold for the Rayleigh number (approximately 10^8) that will define whether a natural convection problem can be simulated as a steady-state problem or a transient problem. Since the gravitational constant can not realistically be left at a value of 0.98 m/s^2, an additional measure must be taken: transforming the simulation to a transient problem.

The converged solution shown on the right of Figure 5.7 was used as an initial condition for a transient solution of the turbulent natural convection problem. The gravitational constant is restored to the appropriate value of 9.81 m/s^2 and the time steps of the transient simulation are determined by the following equation (Fluent Inc., 2003):

$$\Delta t = \frac{L}{4\sqrt{g\beta\Delta TL}} \tag{5.6}$$

where Δt is the time step (s), L is the characteristic length of the problem (=0.75 m for the chamber experiment), g is the gravitational constant (=9.81m/s^2), β is the thermal

expansion coefficient (K^{-1}), and ΔT is the temperature difference between the hot and cold walls (K).

For the cases studied in this chapter, the time step was approximately 0.19 s. The simulation would iterate a user-defined number of times before convergence is reached at any given time step. The simulations performed for this chapter used a maximum of 100 iterations per time steps. If the scaled residuals for the transport variables were all below a specific threshold (10^{-6}), then the simulation would proceed to the next time step. After a predetermined time has elapsed, the overall system will have reached equilibrium and a converged (or stable) turbulent natural convection result can be obtained. The overall simulation duration required to reach a stable solution was found to be approximately 5 minutes. The solutions were compared for longer simulation durations and no change was recorded.

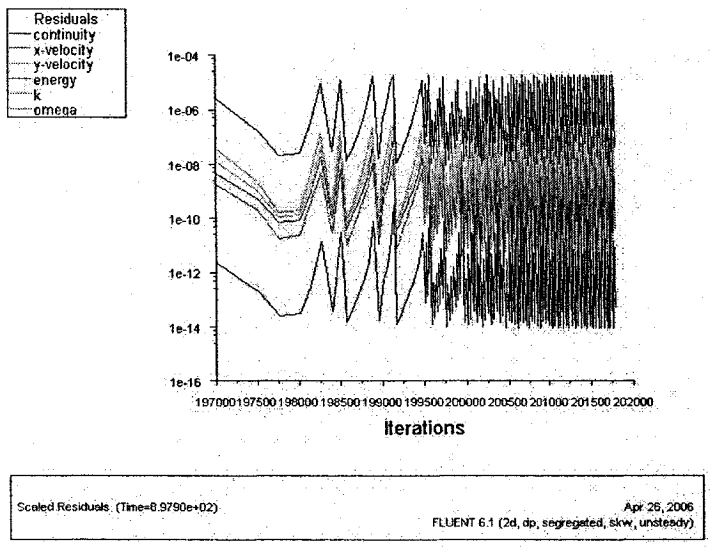

Figure 5.8. Scaled residuals showing convergence for each time step

The solution procedure outlined in this section is very grid dependent and varies based on which turbulence model is used. At times, it was found that the order of the Rayleigh number had to be reduced by several magnitudes below 10^8 in order to obtain a converged solution. However, the solution procedure described in this section was required for all of the turbulence models used to simulate natural convection.

5.5. RESULTS

The four cases related to the horizontal wall boundary conditions were the first simulations performed. The case that represented the top and bottom wall boundary

conditions the most appropriately would be used for all subsequent simulations of the Tian and Karayiannis experiment.

Case #1 results

The experimental results for the temperature profiles at various dimensionless reference heights are compared to the experimental data in Figure 5.9. The range of temperatures for the simulation is between 18 and 41 °C, which does not correspond well with the experimental data (which ranges between approximately 24 and 36 °C). Note that the x-axis for the simulation data is shown in meters, while the experimental data is shown in dimensionless units. They are effectively equivalent though since x = 0.75m is the same location as (dimensionless) X = 1.0.

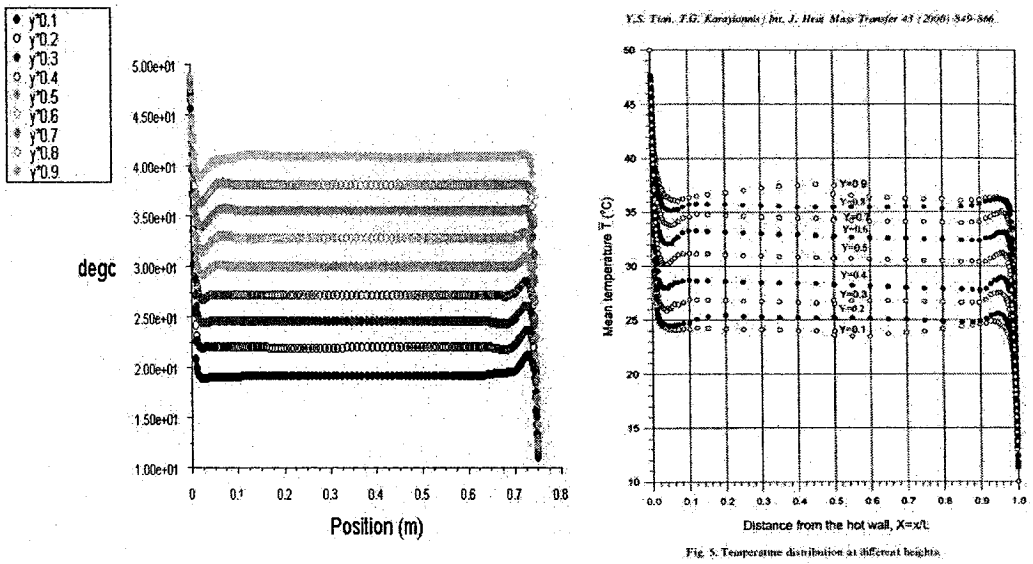

Figure 5.9. Temperature profiles from CFD (left) and experimental data (right) for Case #1

The temperature profiles near the top and bottom plates are shown below in Figure 5.10. As in Figure 5.9, the position axis for the simulation results is not expressed in dimensionless terms, but it represents the same range as the data from the experiment. The left hand side of Figure 5.10 shows the temperature profiles at different cross-sections near the top surface, while the right hand side illustrates the temperature profiles near the bottom wall.

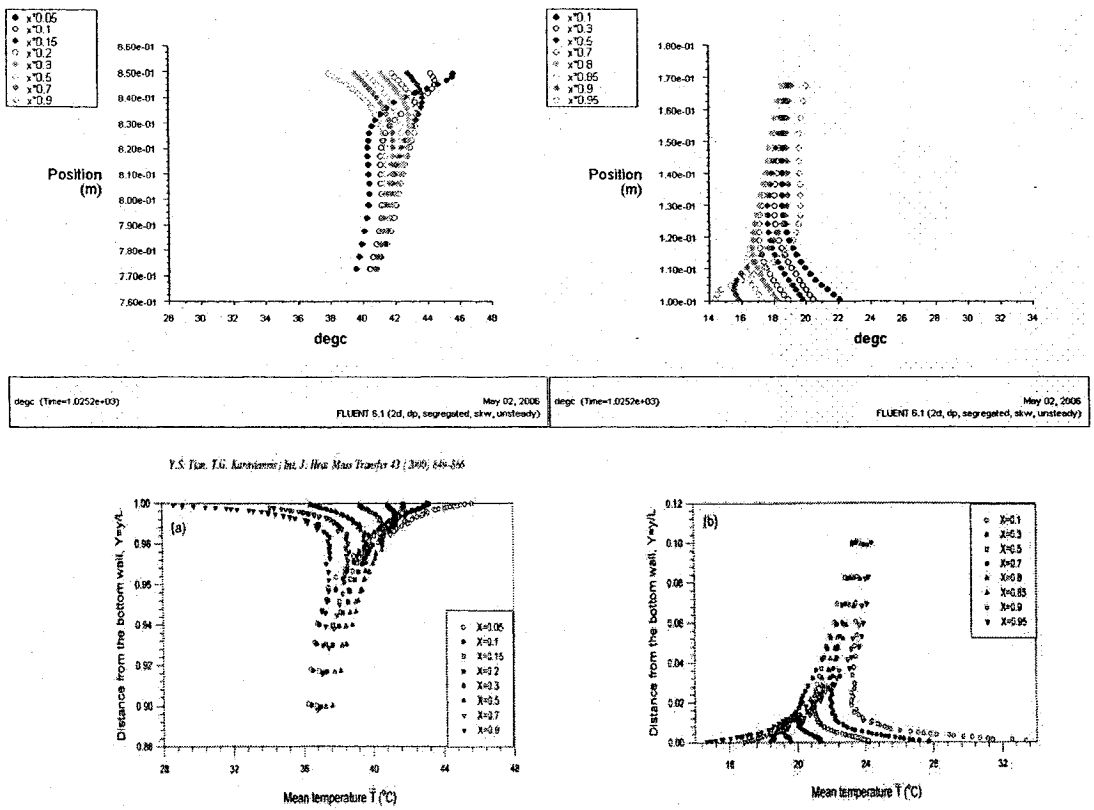

Figure 5.10. Top wall (left) and bottom wall (right) surface temperatures – Case #1

Without radiation enabled, the temperature profiles near the top and bottom wall surfaces appear to be shifted off-center, with respect to the experimental data. For the top surface the average temperature is closer to the hot wall temperature, while the bottom surface is closer to the cold wall temperature. Also, for both surfaces, the temperatures close to the surface have a much smaller range of values than the experimental data.

Case #2 results

The second set of simulations included the effects of radiation on the horizontal surfaces. The Discrete Transfer Radiation model described in Section 2.3.5 was used to model the radiation heat transfer within the experimental chamber. Otherwise, the simulation parameters were identical to those from Case #1, and the results are presented in the same manner. The experimental results for the temperature profiles at various dimensionless reference heights are compared to the experimental data in Figure 5.11.

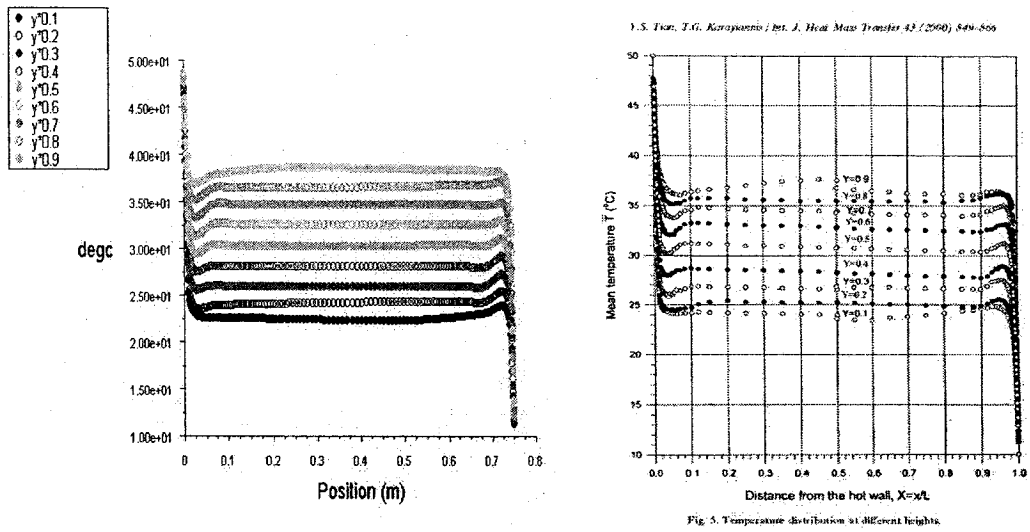

Figure 5.11. Temperature profiles from CFD (left) and experimental data (right) for Case #2

The range of temperatures for the simulation is approximately between 22.5 and 37.5 °C, which corresponds well with experimental data (which ranges between approximately 24 and 36 °C).

The temperature profiles near the top and bottom plates are shown below in Figure 5.12. The left hand side of Figure 5.12 shows the temperature profiles at different cross-sections near the top surface, while the right hand side illustrates the temperature profiles near the bottom wall.

With radiation enabled, the temperature profiles near the top and bottom wall surfaces correspond well with the experimental data. The range of values close to the surface of the wall matches the experimental data range with reasonably good agreement.

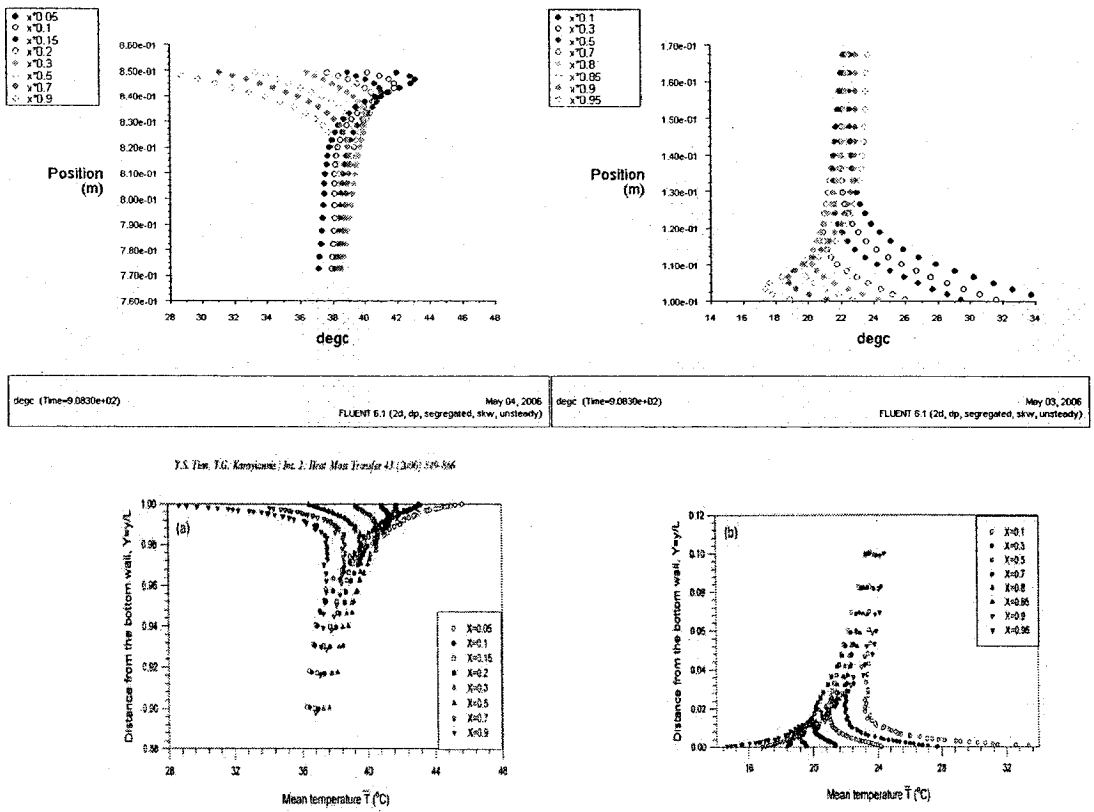

Figure 5.12. Top wall (left) and bottom wall (right) surface temperatures – Case #2

Case #3 results

The third case that was studied for the top and bottom wall boundary condition was similar to Case #2, but with the addition of the steel plate described earlier. The steel was modelled to be in contact with the hot and cold vertical walls. The material properties for the steel were not specified by Tian and Karayiannis, and therefore the default steel properties from *Fluent* were selected for the simulation. Otherwise, the simulation parameters were identical to Case #2. The experimental results for the temperature profiles at various dimensionless reference heights are compared to the experimental data in Figure 5.15. The range of temperatures for the simulation is approximately between 22.5 and 37.5 °C, which is the same range of temperatures seen in Case #2.

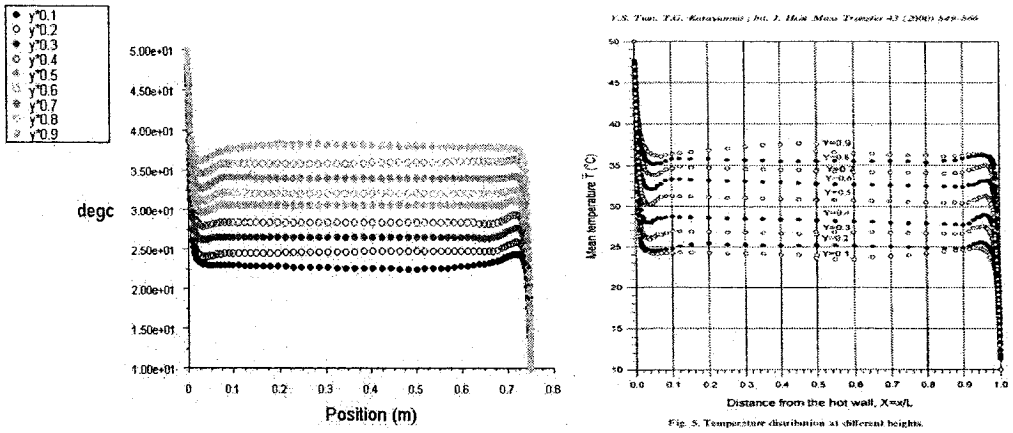

Figure 5.13. Temperature profiles from CFD (left) and experimental data (right) for Case #3

The temperature profiles near the top and bottom plates are shown below in Figure 5.14. The left hand side of Figure 5.14 shows the temperature profiles at different cross-sections near the top surface, while the right hand side illustrates the temperature profiles near the bottom wall.

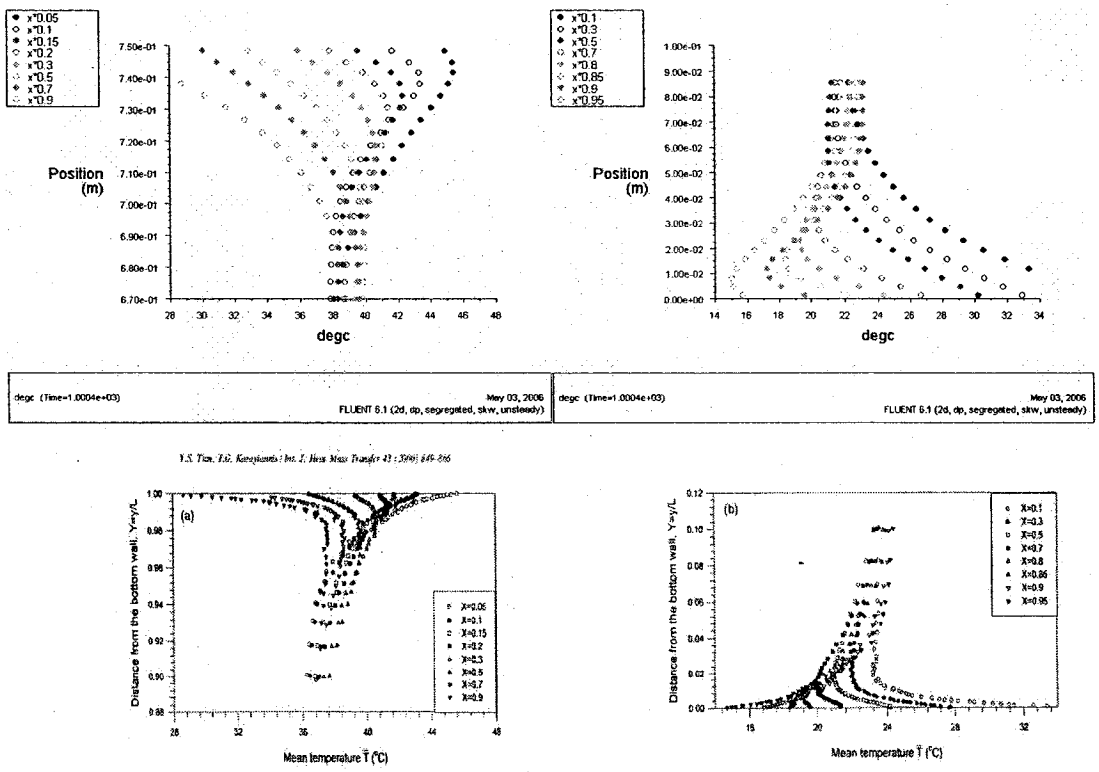

Figure 5.14. Top wall (left) and bottom wall (right) surface temperatures – Case #3

The results for Case #3 were not an improvement over Case #2. The temperature profiles near the wall are not an accurate representation of the experimental conditions, as can be seen in Figure 5.14 above. This could be due to a number of reasons, including the material properties of the steel and the connection detail between the horizontal and vertical walls.

Case #4 results

The fourth case represents the case where the surface temperature measurements from the experiment were applied directly to the top and bottom walls as boundary conditions. The experimental data for the horizontal surface temperatures were used to create user-defined functions that represent fixed boundary conditions, as shown in Figure 5.15. The experimental results are represented by data points, and the user-defined functions are shown as solid lines, which are trend lines fitted to the data points.

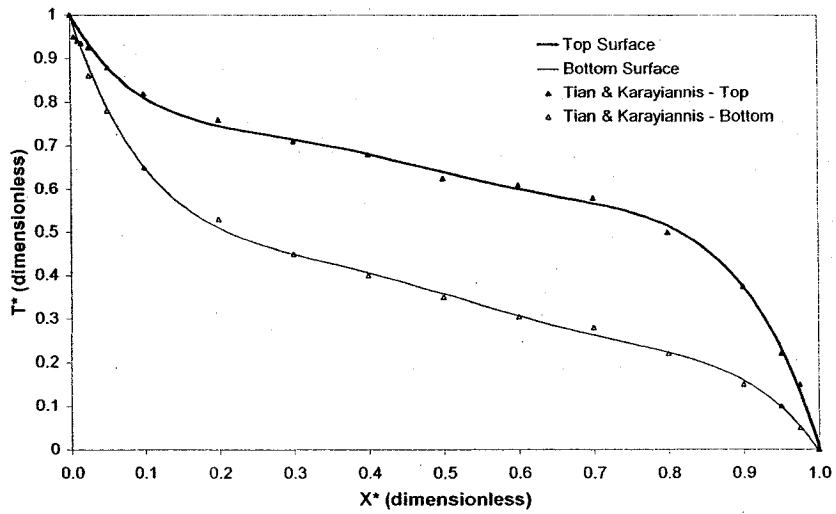

Figure 5.15. Dimensionless temperature profiles for the horizontal wall boundary conditions

It was not necessary to include the effects of radiation in these simulations because of the way the *Fluent* CFD code solves wall temperature boundary conditions. The four wall temperatures were fixed, either to a constant value or to a user-defined function, and therefore even if the radiation model were activated, there would be no net effect on the simulation results. The temperature profiles at various heights are shown in Figure 5.16.

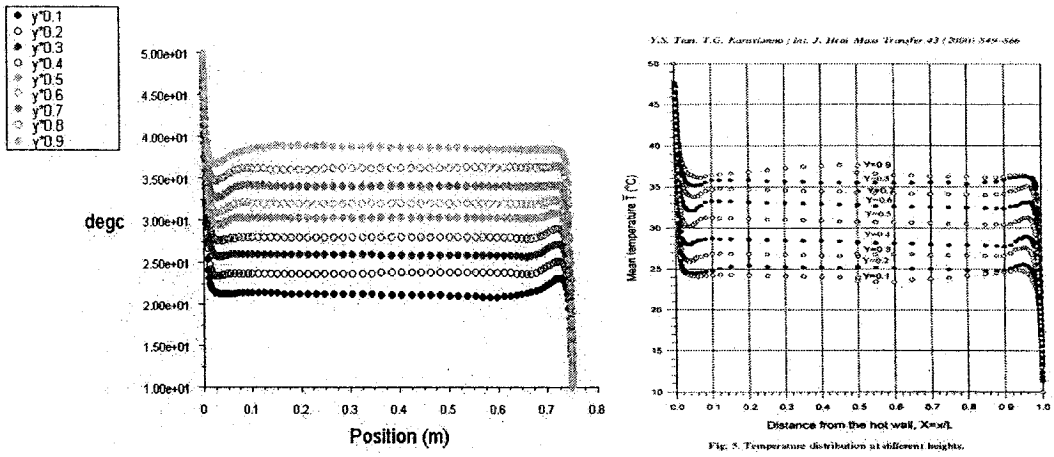

Figure 5.16. Temperature profiles from CFD (left) and experimental data (right) for Case #4

There is a slightly larger margin of temperatures for Case #4 when compared with Case #2 and #3. The temperature curves from the simulation fall between about 21 and 38 °C. The temperatures near the top and bottom walls are shown below in Figure 5.17. The profiles have good agreement with the experimental profiles, and result in a better approximation of the thermal boundary conditions for the top and bottom walls of the experimental chamber.

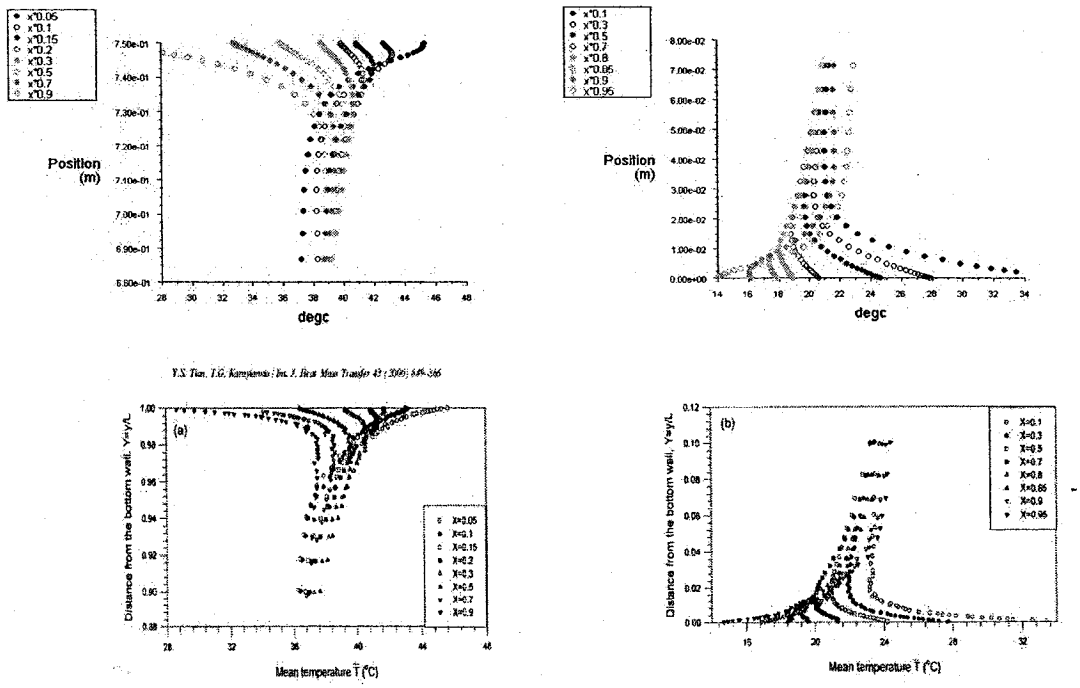

Figure 5.17. Top wall (left) and bottom wall (right) surface temperatures – Case #4

Upon reviewing the results from the four cases for the horizontal boundary conditions, the fourth case was selected to be used for the next series of simulations. The material properties of the steel and the insulation were not known and the connection detail at the corner of the chamber was unclear, and therefore could negatively influence the results without any way to clearly identify the resulting error. Case #4 had the least amount of assumptions required to perform the simulation, and therefore was selected to represent the horizontal wall boundary conditions.

Turbulence Model Comparison

Once the difficulties associated with simulating turbulent natural convection were resolved, the simulations were performed using the mesh and boundary conditions described in Section 5.3. The following turbulence models were used in the simulations:

1) *Spalart-Allmaras Model*
2) *Standard k-ε Model*
3) *RNG k-ε Model*
4) *Realizable k-ε Model*
5) *Standard k-ω Model*
6) *SST k-ω Model*

The results for the experimental measurements and the natural convection simulations are located in Appendix B. In order to compare the simulation results to the data from the Tian and Karayiannis experiment, the simulation data is presented in the same format as the authors used in their paper (Tian and Karayiannis, 2000). The simulation results for the Standard *k-ε* turbulence model are explained below as an example.

The velocity results shown in Figure 5.18 and Figure 5.19 are expressed in dimensionless terms. The horizontal and vertical velocity components, u and v respectively, are divided by the buoyancy velocity, which can be calculated with the following equation (Tian and Karayiannis 2000):

$$V_o = \sqrt{g\beta H \Delta T} \tag{5.7}$$

where V_o is the buoyancy velocity (m/s), g is the gravitational constant (=9.81 m/s^2), β is the thermal expansion coefficient (K^{-1}), H is the characteristic height of the domain (m)

and ΔT is the temperature difference between the heated plates (K). For the natural convection cases studied, V_o is equal to 1 m/s.

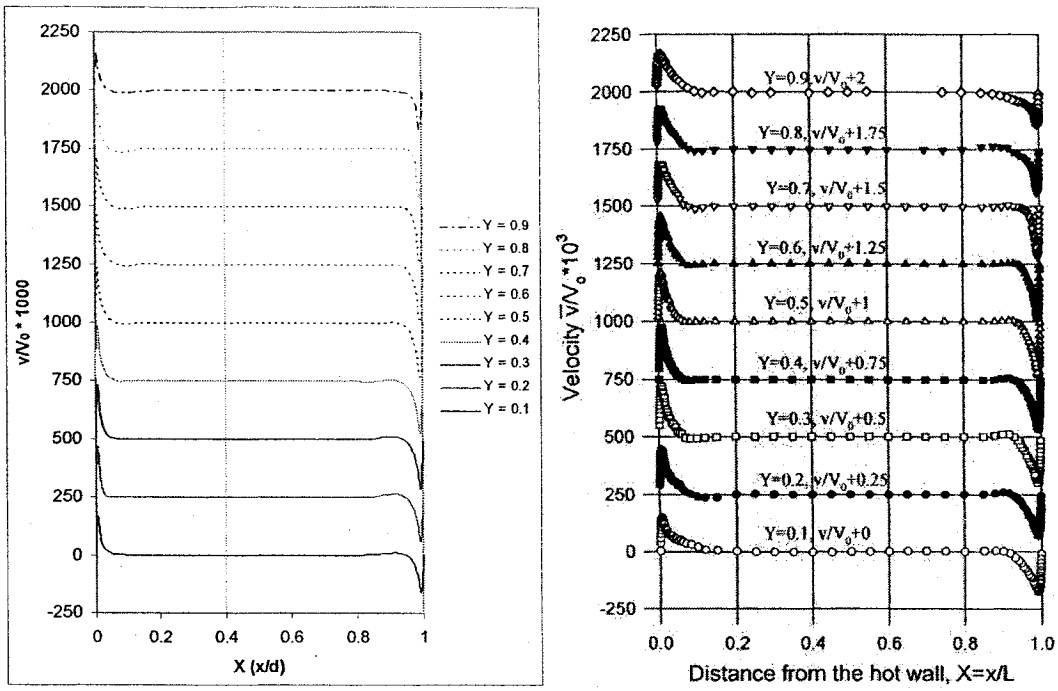

Figure 5.18. Sample vertical velocity from CFD simulations (left) and experiment (right)

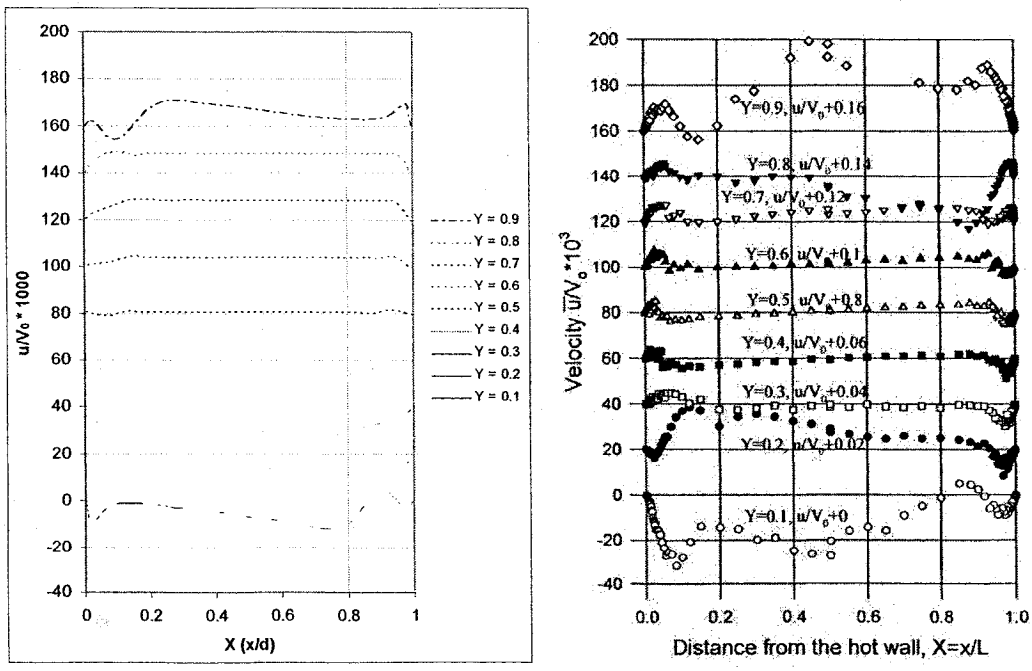

Figure 5.19. Sample horizontal velocity from CFD simulations (left) and experiment (right)

In order to clarify the results, each curve shown in Figure 5.18 and Figure 5.19 is offset by a constant depending on the value of the dimensionless height. For example, for the horizontal velocity results in Figure 5.19 when Y = 0.2 the value of $(u/V_o)*1000$ is offset by +20. When Y = 0.3 the results are offset by +40, and so on. The same holds true for the vertical velocity component, though the magnitude of the constant is larger.

The results from Figure 5.18 and Figure 5.19 indicate a good agreement between the simulation results and the experimental measurements. The vertical velocity peak values are very close to the corresponding experimental curves. The horizontal velocity graphs tend to differ near the top and bottom walls (i.e. Y = 0.1 and Y = 0.9). However, the velocity magnitudes are very low and the positions of flow reversal are generally consistent between experimental and simulation data.

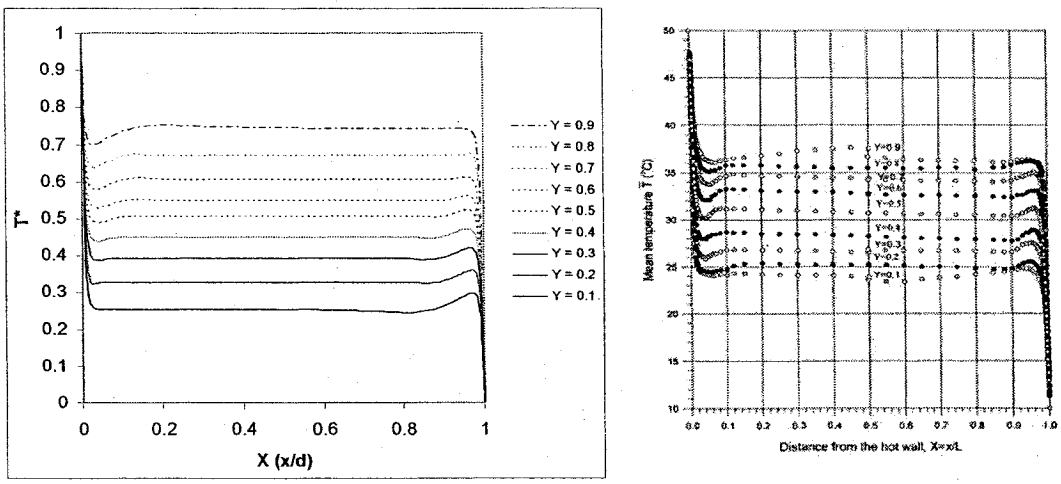

Figure 5.20. Sample dimensionless temperature results for CFD simulations (left) and experiment (right)

The dimensionless temperatures (from Equation 5.3) are shown for different reference heights on the left of Figure 5.20, which are compared to experimental data shown on the right. Note that the vertical scale of the two graphs represents the same range of temperatures for both simulation and experimental results. In addition to plotting the results, the temperature contours were obtained directly from *Fluent*. A sample contour plot is shown below in Figure 5.21. The experimental results of Tian and Karayiannis were plotted using a similar technique.

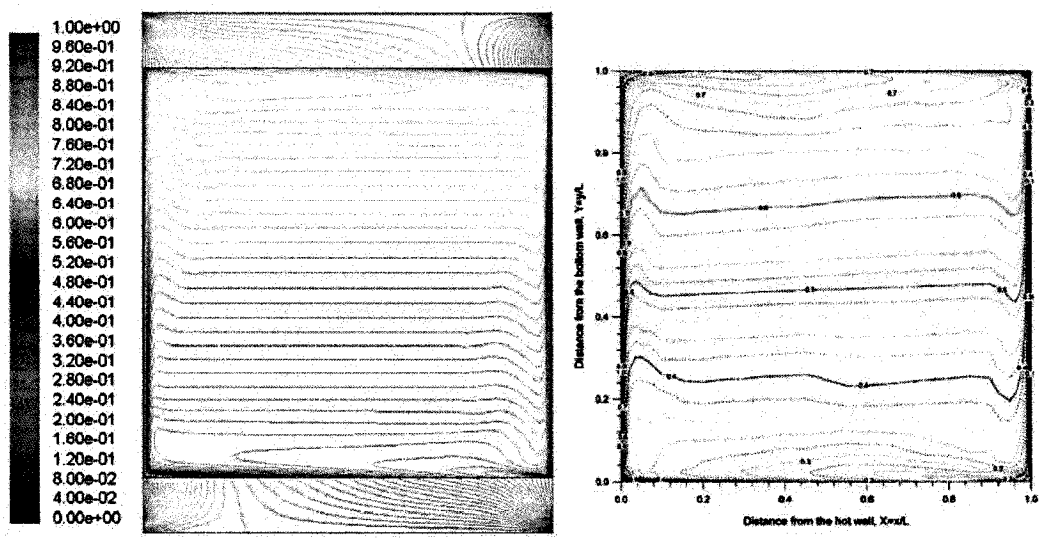

Figure 5.21. Sample dimensionless temperature contour plots for the CFD simulation (left) and experimental data (right)

The temperature contour plot in Figure 5.21 is consistent in pattern and has temperature values for the simulation throughout the domain that are generally in good agreement with the experimental contour plot.

Chapter 2 described how the convective heat and vapour transport are largely dependent upon the boundary layer velocity, temperature, and vapour pressure profiles, among other parameters. The simulation results were compared to the experimental data within the boundary layer at a dimensionless height of Y = 0.5 at the hot wall.

The boundary layer velocity profiles calculated using CFD are illustrated below in Figure 5.22. The different turbulence models resulted in similar profiles within the laminar regime, which is the region approximately between x = 0m and x = 0.003m. The peak velocities vary between about 0.225 m/s for the Standard k-ω turbulence model up to approximately 0.257 m/s for the Spalart-Allmaras and SST k-ω models. In general, the simulation results tend to over-predict the maximum vertical velocity, with a resulting error between 8.7% and 24.2%. The Standard k-ω model had the best overall fit for the boundary layer vertical velocity. The three k-ε models generated virtually identical velocity profiles. The Spalart-Allmaras model generated the profile with the least agreement with experimental data. This is suspected to be due to the way turbulence viscosity is modelled differently for the different turbulence models, which affects governing equations described earlier in Section 2.3.4.

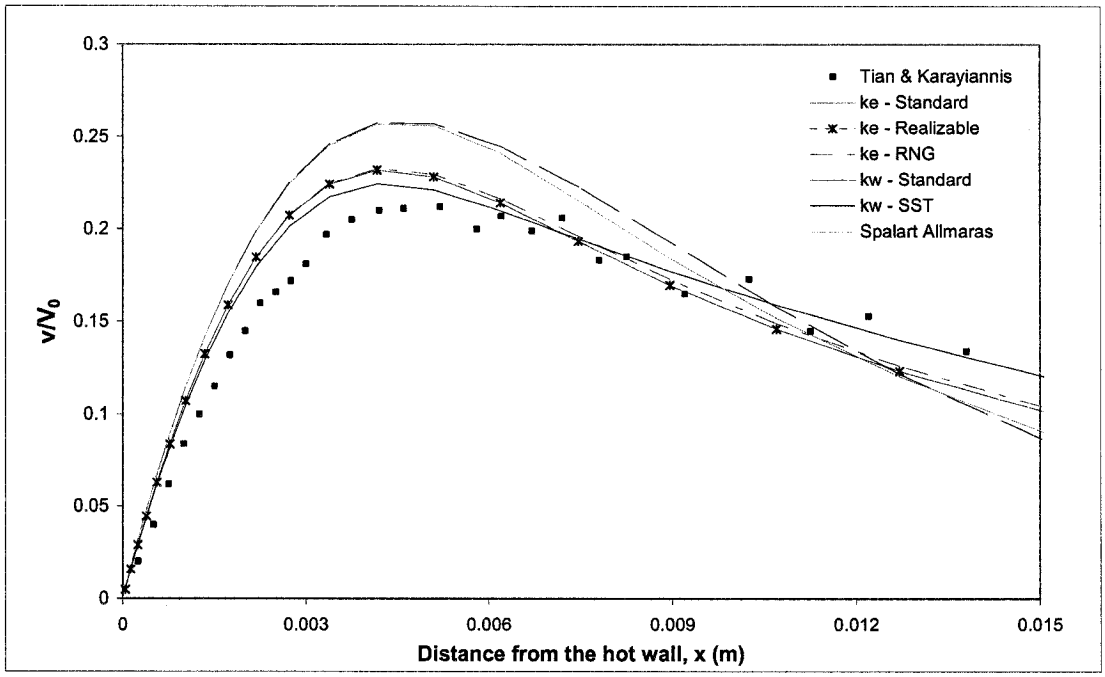

Figure 5.22. Boundary layer velocity profile results

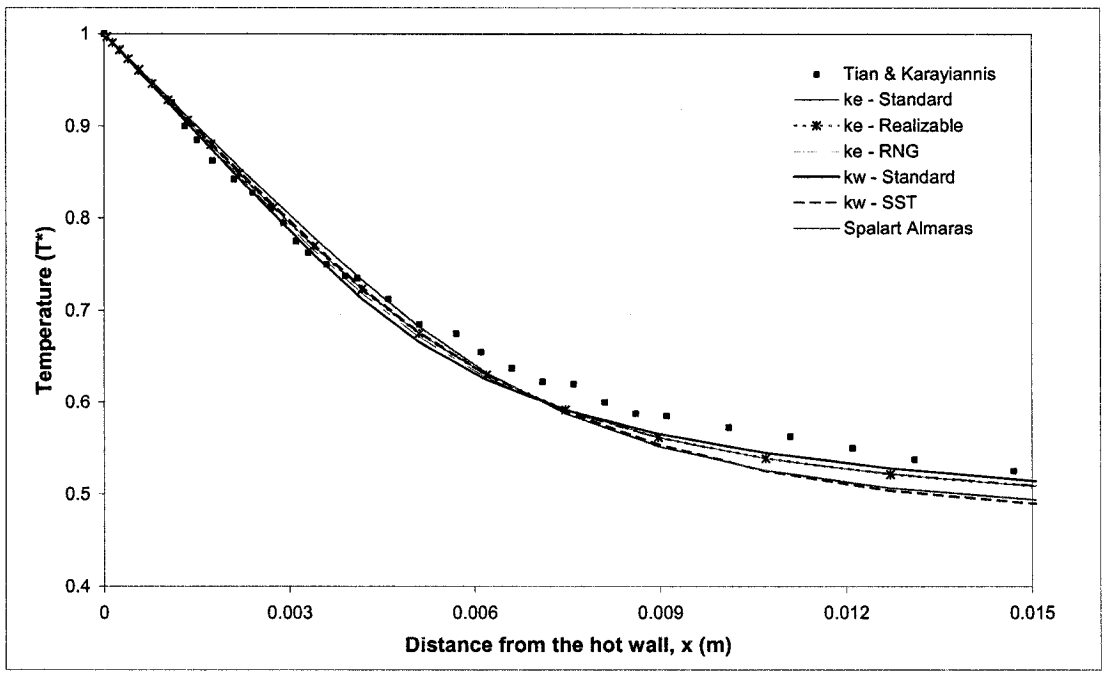

Figure 5.23. Boundary layer temperature profile results

The boundary layer temperature profiles are shown above in Figure 5.23. The six different turbulence models provided very similar results for temperature, particularly

within the laminar sublayer. The maximum error between the simulation and experimental results was between 2.0% and 6.7%. The Standard k-ω model had the best overall fit for boundary layer temperature when compared with the experimental data. As with the velocity profiles, the k-ε models generated identical temperature profiles with slight differences within the laminar region. The Spalart-Allmaras and SST k-ω models generated the profiles with the least agreement with experimental data. This is suspected to be due to the way turbulence viscosity affects the effective conductivity in the energy equation (refer to Section 2.3.4).

The convective heat transfer coefficients were obtained using an area-weighted average value of the local heat transfer coefficients for both the hot and cold walls of the simulation. The simulation results were compared to the convective heat transfer coefficient calculated from the correlation presented in Section 5.2. The results are presented below in Table 5.2. The percentage error was calculated based on the convective heat transfer coefficient from the correlation:

$$\%Error = \left(\frac{h_{cL} - h_{cA}}{h_{cA}} \right) * 100 \tag{5.8}$$

where h_{cL} are the simulation convective heat transfer coefficients (W/m^{2}K) and h_{cA} is the correlation convective heat transfer coefficient value (W/m^{2}K).

Table 5.2. Convective heat transfer coefficients for natural convection

Turbulence Model	Hot Wall h_{cL}(W/m^{2}K)	Cold Wall h_{cL} (W/m^{2}K)	% Error Hot Wall	% Error Cold Wall
Spalart-Allmaras	3.734	3.744	2.95%	3.23%
k-ε Standard	3.838	3.848	5.82%	6.09%
k-ε Realizable	3.838	3.848	5.82%	6.09%
k-ε RNG	3.882	3.890	7.03%	7.25%
k-ω Standard	3.918	3.929	8.02%	8.33%
k-ω SST	3.809	3.818	5.02%	5.27%

The degree of accuracy for the correlation in Equation 5.1 was previously stated to be approximately 5.5% for Rayleigh numbers above 10^5. For Rayleigh numbers above 10^8, the correlation under-predicts the plate-averaged Nusselt numbers, which

indicates that the simulation results are closer to reality than indicated in Table 5.2 (Lienhard and Lienhard 2006).

5.6. Discussion and Conclusions

A natural convection experiment performed by Tian and Karayiannis (2000) was simulated using CFD. A methodology to overcome convergence issues associated with simulating turbulent natural convection was presented and applied successfully to a number of simulations.

The boundary conditions of the experiment were simulated by varying a number of simulation parameters, which did not result in good agreement between the temperature profiles of the experiment and the simulation. The unknown properties of the steel plate along the horizontal and vertical walls, and the lack of information regarding the connection detail at the corners of the chamber contributed to the error. Finally, the temperature profiles along the horizontal surfaces from the experiment were used as boundary conditions.

The boundary layer profiles along the hot wall had very good agreement with experimental profiles. The maximum error for the different turbulence models varied between 8.7% and 24.2% for the velocity profile and between 2.0% and 6.6% for the temperature profile.

The convective heat transfer coefficients averaged over the vertical walls were compared to a correlation developed for natural convection over vertical plates. The experimental situations matched the requirements for which the correlation was developed. The error between experimental and correlation values for the convective heat transfer coefficients varied between 2.95% and 8.33%. In general, the simulation results slightly over predicted the convective heat transfer for all of the turbulence models studied.

CHAPTER 6. HEAT AND VAPOUR TRANSPORT

A number of simulations were performed for forced and natural convection, and the results compared with analytical, semi-empirical or empirical formulae. The convective heat transfer coefficients calculated with CFD have been shown to have very good agreement with validation data. Consequently, it was decided to use CFD to perform simulations of coupled heat and vapour transport.

This chapter presents the coupled model developed to calculate convective heat and vapour transfer coefficients. First, the limitations of CFD with respect to vapour transport are presented in Section 6.1. Next, the theory required for the model is presented in Section 6.2. The details of the coupled model are outlined in Section 6.3, and an application of the model is presented in Section 6.4. Finally, the results are discussed in Section 6.5.

6.1. LIMITATIONS OF CFD

This section will focus on the limitations of general-purpose CFD codes for calculating convective heat and vapour transfer coefficients. The *Fluent 6.2.16* CFD commercial software was used for all of the simulations in this thesis. *Fluent* has the capability to model vapour transport within fluid regions with Species Modelling. However, this capability does not extend to solid regions. This restriction prevents the modelling of diffusive vapour transport within a porous material directly in *Fluent*. As shown in Sections 2.4.1 and 2.4.2 of the literature review, experiments and modelling have indicated discrepancies between the Chilton-Colburn analogy and numerical or experimental values of surface coefficients for cases involving porous materials such as wood. Therefore, if CFD is to be used for modelling of combined heat and vapour transport, the models must be modified to include vapour diffusion within the porous materials (Fluent Inc. 2003).

Another limitation of CFD is the limited number of boundary conditions that can be specified for species modelling. The transport variable for species modelling is called mass fraction. The mass fraction for vapour transport in air can be expressed in terms of vapour pressure by using the ideal gas law:

$$X' = \frac{p_v}{\rho_a R_v T} \tag{6.1}$$

where X' is the mass fraction (kg_{vapour}/kg_{air}), p_v is the vapour pressure (Pa), ρ_a is the density of the air (kg/m^3), R_v is the ideal gas constant for water vapour (=461.52 J/kg-K), and T is the temperature of the air (K).

At the surface of a wall, the mass fraction can be specified as one of two boundary conditions (Fluent Inc. 2003):

1) Zero flux condition: the diffusive vapour flux at the surface of wall is set to zero. This is the default condition for *Fluent*.
2) Specified mass fraction: The user can specify either a constant value that is fixed at the wall surface, which will remain unchanged throughout the simulation, or a user-defined mass fraction boundary profile. The user-defined profile can be based on a user-defined function (for example, an equation that yields mass fraction as a function of position) or a boundary profile that is input from a formatted data file.

The boundary conditions are considered a limitation because a user-defined flux condition different from zero cannot be specified, and a fixed mass fraction boundary condition is not practical for most cases.

6.2. THEORY

The case that was selected for modelling of heat and vapour transport was for air flow over a porous material. Wood was selected as the material for the porous zones of the model. The general geometry of the case studied is presented in Figure 6.1.

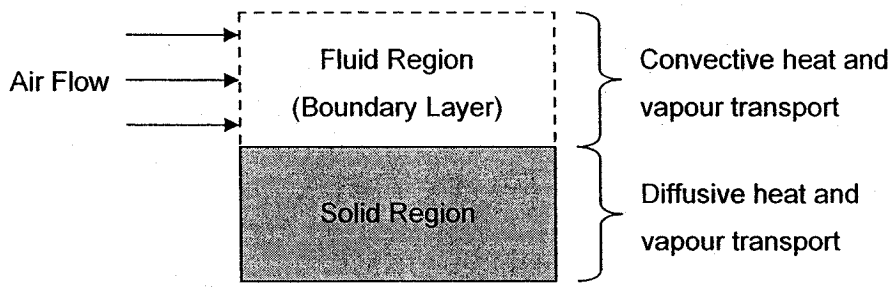

Figure 6.1. Domain for convective and diffusive heat and vapour transport

The heat and vapour transfer shown in Figure 6.1 can be divided into convective and diffusive transfer processes. The theory for convective and conductive (diffusive) heat transport has been previously described in Section 2.1.1. Convective vapour

transport theory was presented in Section 2.1.2. Radiation heat transfer, while not shown in Figure 6.1, will be considered as well and has been described in Section 2.1.1 and 2.3.5.

The equation for diffusive vapour flux within a solid material was expressed in Equation 2.6 as:

$$G = -\delta A \frac{\partial p_v}{\partial x} \tag{6.2}$$

When considering diffusion in a porous material, the storage of moisture must be considered. If one considers vapour transport between two points, the resulting equation can be expressed as:

$$A \frac{\partial w}{\partial t} = \frac{\partial}{\partial x}\left[-\delta A \frac{\partial p_v}{\partial x} \right] \tag{6.3}$$

where w is the moisture content (kg_{vapour}/m^3), δ is the vapour permeability of the material (s), A is the area perpendicular to the vapour flow, p_v is the partial vapour pressure (Pa), and x is the direction of the vapour flow (m). The gradient $\partial w/\partial t$ represents the vapour storage within the material. Material properties for wood are often expressed in terms of relative humidity, and therefore Equation 6.3 can be transformed as:

$$A \frac{\partial w}{\partial \phi} \frac{\partial \phi}{\partial t} = \frac{\partial}{\partial x}\left[\delta A p_{vsat} \frac{\partial \phi}{\partial x} + \delta A \phi \frac{\partial p_{vsat}}{\partial T} \frac{\partial T}{\partial x} \right] \tag{6.4}$$

where ϕ is the relative humidity, p_{vsat} is the saturation vapour pressure (Pa), and the gradient $\partial w/\partial \phi$ represents the slope of the sorption isotherm for the wood.

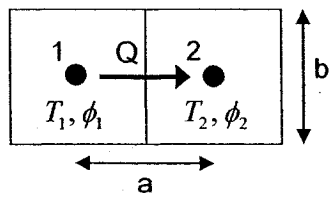

Figure 6.2. Flux from one volume to an adjacent volume

Equation 6.4 can be used to describe the total vapour flux from one volume to an adjacent volume, as illustrated in Figure 6.2. If the temperature of the two volumes is different, Equation 6.4 must be modified to account for the temperature dependent properties of the water vapour. Before the temperature dependence of the materials can

be implemented, the total vapour flux from volume 1 to volume 2 can be spatially discretised as:

$$Q_{1\to 2} = b\delta p_{vsat}\frac{(\phi_1-\phi_2)}{a} + b\delta\phi\frac{(T_1-T_2)}{a}\frac{\partial p_{vsat}}{\partial T} \tag{6.5}$$

where $Q_{1\to 2}$ is the vapour flux from point 1 to point 2 in Figure 6.2 (kg/s), *a* is the distance between points 1 and 2, *b* is the cross-sectional area perpendicular to the flux (for the one-dimensional case presented, the depth is assumed to be equal to 1) (m^2), T_1 and T_2 are the temperatures of the two volumes (K), and ϕ_1 and ϕ_1 are the relative humidity values of the two volumes. Note that Equation 6.5 does not take into account the variable properties for permeability and saturated vapour pressure for the two volumes, and therefore a modified model for diffusion is used, as shown in Figure 6.3.

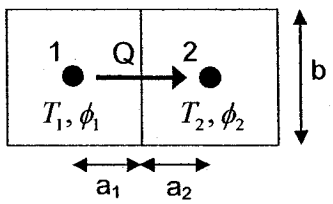

Figure 6.3. Modified vapour flux diagram

The diagram in Figure 6.3 divides the distance between the volume centers into two parts, and the properties found in Equation 6.5 will be evaluated at the appropriate temperature and relative humidity values for the two volumes. In equation form the flux can then be expressed as:

$$Q_{1\to 2} = \frac{b(\phi_1-\phi_2)}{\left(\dfrac{a_1}{\delta\{\phi_1\}p_{VSAT}\{T_1\}} + \dfrac{a_2}{\delta\{\phi_2\}p_{VSAT}\{T_2\}}\right)} + \frac{b(T_1-T_2)}{\left(\dfrac{a_1}{\delta\{\phi_1\}\phi_1\dfrac{\partial p_{VSAT}\{T_1\}}{\partial T}} + \dfrac{a_2}{\delta\{\phi_2\}\phi_2\dfrac{\partial p_{VSAT}\{T_2\}}{\partial T}}\right)} \tag{6.6}$$

Equation 6.6 uses curled braces { } to describe when a property is to be evaluated at a certain temperature or relative humidity. For example, $\delta\{\phi_1\}$ indicates that the permeability should be evaluated at the relative humidity for Volume 1.

Equation 6.6 was used as the basis for a control-volume model that calculates the diffusion within wood, and couples the solution with a CFD simulation of convective drying of saturated wood samples.

In order to numerically solve the equations presented in Section 6.2, a control-volume technique is used to discretise the computational domain. A solid region can be divided into a discrete number of volumes, and the relative humidity for a given volume can be expressed as a function of the fluxes from adjacent volumes and the vapour stored or released within the volume. An example of the discretization of a two-dimensional domain is shown in Figure 6.4.

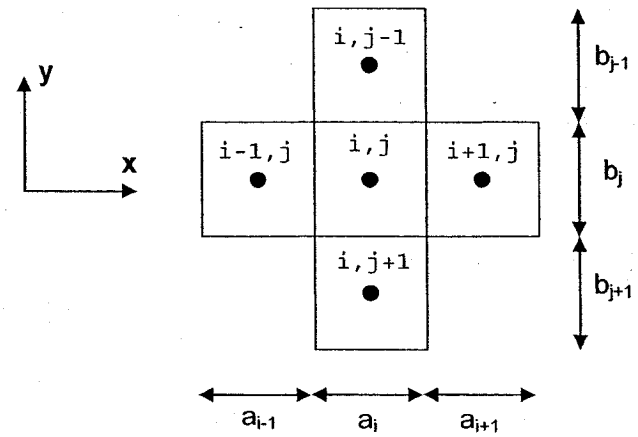

Figure 6.4. Control volumes for a given domain

The volume denoted by (i,j) in Figure 6.4 represents the cell for which the relative humidity is being solved. The adjacent nodes are labelled based upon their position relative to the central node. The convention chosen is similar to positions in a matrix; the *i*-direction is positive from left to right and *j*-direction is positive from top to bottom. This convention simplifies the programming of the solution, which is discussed later.

Equation 6.6 is used to describe the vapour flux from an adjacent volume to the central volume. Given that the vapour storage within a material is time dependent, Equation 6.6 is modified to include time-dependent properties. An implicit time stepping scheme is chosen, which means that the properties for the variables such as permeability and saturated vapour pressure are evaluated for the current time step conditions, instead of the conditions from the previous time step. The resulting equation can be derived as:

$$Q^{t+\Delta t}_{(i-1,j)\to(i,j)} = \frac{b_j\left(\phi^{t+\Delta t}_{i-1,j} - \phi^{t+\Delta t}_{i,j}\right)}{\left(\delta_{i-1,j}\left\{\phi^{t+\Delta t}_{i-1,j}\right\}p_{VSAT}\left\{\theta^{t+\Delta t}_{i-1,j}\right\}^{\frac{0.5a_{i-1}}{}} + \delta_{i,j}\left\{\phi^{t+\Delta t}_{i,j}\right\}p_{VSAT}\left\{\theta^{t+\Delta t}_{i,j}\right\}^{\frac{0.5a_i}{}}\right)}$$
$$+ \frac{b_j\left(\theta^{t+\Delta t}_{i-1,j} - \theta^{t+\Delta t}_{i,j}\right)}{\left(\delta_{i-1,j}\left\{\phi^{t+\Delta t}_{i-1,j}\right\}\phi^{t+\Delta t}_{i-1,j}\frac{\partial p_{VSAT}\left\{\theta^{t+\Delta t}_{i-1,j}\right\}}{\partial\theta}^{\frac{0.5a_{i-1}}{}} + \delta_{i,j}\left\{\phi^{t+\Delta t}_{i,j}\right\}\phi^{t+\Delta t}_{i,j}\frac{\partial p_{VSAT}\left\{\theta^{t+\Delta t}_{i,j}\right\}}{\partial\theta}^{\frac{0.5a_i}{}}\right)} \quad (6.7)$$

where $Q^{t+\Delta t}_{(i-1,j)\to(i,j)}$ is the vapour flux from volume (i-1,j) to (i,j), θ is the temperature within the designated volume (K), the superscript $t+\Delta t$ indicates that the values of the designated parameters are to be evaluated for the current time step. The remainder of the parameters are as described in Equation 6.6. The equations for the three other adjacent cells are presented in Appendix C.

The total change of moisture within the central volume (i,j) can be expressed as the sum of the fluxes from the adjacent cells, which is equal to the vapour stored (or released) over time:

$$Q^{t+\Delta t}_{(i-1,j)\to(i,j)} + Q^{t+\Delta t}_{(i+1,j)\to(i,j)} + Q^{t+\Delta t}_{(i,j-1)\to(i,j)} + Q^{t+\Delta t}_{(i,j+1)\to(i,j)} = \xi\left(\frac{\phi^{t+\Delta t}_{i,j} - \phi^{t}_{i,j}}{\Delta t}\right)a_i b_j \quad (6.8)$$

where ξ is the slope of the sorption curve (previously described as $\partial w/\partial\phi$), the superscript t denotes a parameter evaluated at the previous time step, and Δt is the time step duration (s). Equation 6.8 can be rearranged to be in terms of the relative humidity values for the five relevant volumes (central and four adjacent):

$$C_1\phi^{t+\Delta t}_{i-1,j} + C_2\phi^{t+\Delta t}_{i+1,j} + C_3\phi^{t+\Delta t}_{i,j-1} + C_4\phi^{t+\Delta t}_{i,j+1} + C_5\phi^{t+\Delta t}_{i,j} = C_6 \quad (6.9)$$

where C_1 to C_6 are coefficients that are described in Appendix C.

If the procedure outlined above is repeated for every cell in a domain with *m* cells in the x-direction and *n* cells in the y-direction, the result will be a system of linear equations that can be expressed as a matrix equation:

$$[C]\{\phi\} = \{C_6\} \quad (6.10)$$

where C is a matrix of size (m*n)x(m*n) that contains the coefficients C_1 to C_5, $\{\phi\}$ is a vector of size (m*n)x(1) that contains the unknown relative humidity values for each volume, and $\{C_6\}$ is a vector of size (m*n)x(1) that contains the coefficients C_6

described in Equation 6.9. The results from Equation 6.9 (and thus 6.10) should be iterated several times in order to reach a converged solution, primarily because the properties found in Equation 6.7 must be evaluated for the current time step properties, which are unknown for the first iteration.

6.3. MODEL COUPLING

CFD has the capability to solve heat and vapour transport in fluid regions, and heat transport within solid regions. Chapters 3, 4, and 5 demonstrated the accuracy of the convective heat transfer solutions for a number of flow situations. Section 6.2 presented the equations governing the vapour diffusion process in a porous material such as wood. In order to simulate the coupled heat and vapour transport for air flowing over a porous material, CFD simulation results were coupled with a vapour diffusion model developed based on the equations presented in Section 6.2.

The equations for vapour diffusion were implemented in *Matlab 7.0*, which is a commercial software used for solving complex mathematical problems. *Matlab* contains integrated solvers for matrix equations, which were particularly useful for solving Equation 6.10 to determine the relative humidity values for each volume within the domain. Once the routine was programmed into *Matlab*, the procedure to couple the vapour diffusion model with the CFD simulation from *Fluent* was investigated.

Matlab has the capability of calling external programs using a command line operator (denoted with an exclamation mark "!"), and, for this reason, it was selected as the controller for the coupled model. An example of a program being called from the *Matlab* command line would be:

```
!Fluent.exe
```

Even though the command above will run the *Fluent* software, there are still a number of manual steps required to perform a simulation that cannot be accomplished from within *Matlab*. For example, a case and data file would have to be opened, the simulation initialized, the number of iterations specified, etc. Such commands cannot be performed directly from *Matlab*. However, they can be automated within *Fluent* through the use of a journal file, which is essentially a list of commands that will be performed sequentially until the end of the file. Given that journal files can automate a simulation and that *Fluent* can be opened from the command line within *Matlab*, all that remained was finding a way to open *Fluent* and directly run a journal file, thus avoiding any manual intervention within *Fluent*.

It was found that the `Fluent.exe` command can be opened with a number of conditional parameters that will automate the program startup. For example, the program can be opened and run in the background of the computer, or can open and run a journal file directly from the command line. As an example, the following command line, when executed within *Matlab*, will open *Fluent* in the double precision mode (`2ddp`), run it in the background (`-g`), and immediately run the journal file entitled *initialize* (`-i initialize`):

```
!Fluent.exe 2ddp -g -i initialize
```

By using the command line above, *Fluent* simulations can be performed from within *Matlab* using journal files, without ever having to interact with the *Fluent* software during the simulation. However, the simulation parameters must be carefully prepared before this can function properly, and the journal files must contain a number of important commands that prevent the need for user interaction. For example, all dialogue commands that require file-overwrite confirmation must be disabled.

When *Matlab* runs an external program via the command line, it does not recognize whether or not that command has been completed. Programs are executed on a line-by-line basis. The simulations performed in *Fluent* are not instantaneous, and *Matlab* has no built-in method of determining if the simulation was completed or still in progress. The program must either be told to wait for a fixed duration to allow the CFD simulation to reach completion, or it must be told when the program has ended. Due to the variable simulation durations, pausing for a fixed amount of time is prohibitively expensive in terms of computation time. To account for this problem, an external program called `Tasklist.exe` is utilized. `Tasklist` is a system tool that can verify whether a particular process is running on a *Windows* operating system. *Matlab* was programmed to call the `Tasklist` command periodically (every 5 seconds) to verify that the *Fluent* program was still running on the operating system. Once the check was performed and returned a negative result, the program would recognize that the *Fluent* simulation was complete and would proceed with the vapour diffusion calculation.

Another issue that was encountered within *Matlab* was the memory requirements for storing the matrix C from Equation 6.10. The first simulation performed with the model was for a wood region that was subdivided into 38 vertical elements and 100 horizontal elements. The number of elements was equal to the number of control volumes in the mesh that was created for the CFD simulation. Given that the matrix C

has dimensions equal to (m*n)x(m*n), the resulting matrix is 3800x3800 cells, which requires storage of 14.44 million data points. Since the matrix C is a sparse banded matrix, the vast majority of the elements are zero. *Matlab* has the capability to transform a matrix into a sparse matrix, which will only store the non-zero values within the matrix. Through this method, the memory requirements were reduced by an order of about 770, requiring the storage of only 18,724 elements for that particular example.

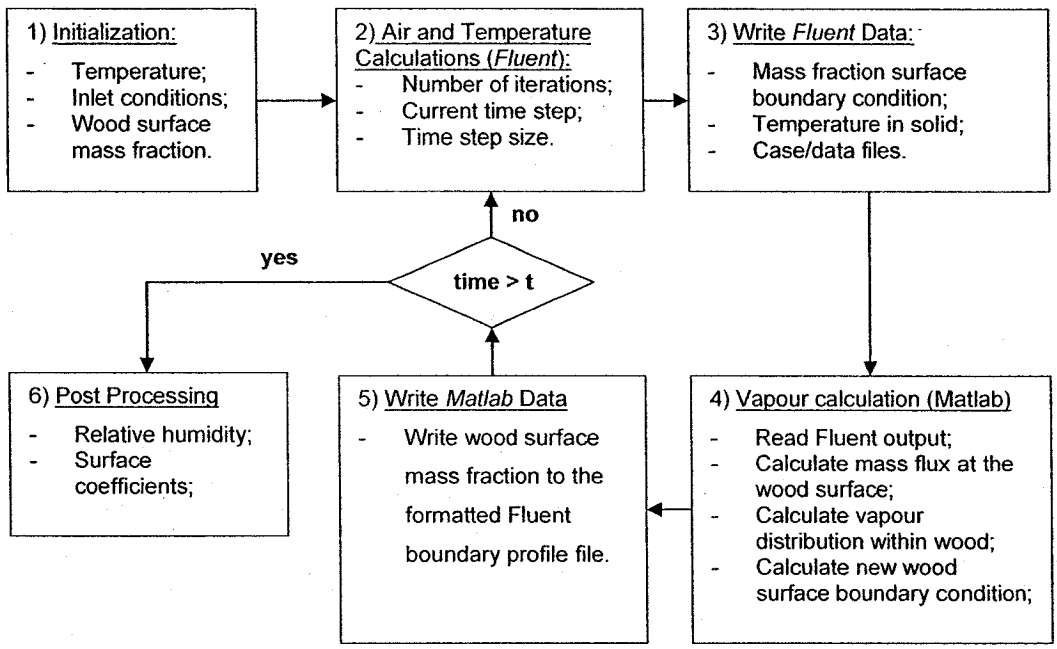

Figure 6.5. Coupled model flowchart

The flowchart for the solution process for the coupled heat and vapour transfer model is shown above in Figure 6.5. The data is transferred between each program using data files that are imported and overwritten within *Fluent* and *Matlab*. For example, the mass fraction boundary condition at the surface of the porous material is stored in a file read by *Fluent*, which has a particular format. After the vapour diffusion calculation within *Matlab*, the mass fraction boundary condition for the next time step is written to the same boundary profile file. The program within *Matlab* was designed to write the file in the exact format required by *Fluent*, and, in the case of any errors within the formatting, *Fluent* would return an error and the simulation would end. The six steps shown in Figure 6.5 are described in further detail below.

1) **Initialization**. The *Fluent* simulation is initialized based on a predetermined journal file. The variables for the general dimensions of the porous material are created and stored in memory.
2) **Air flow and temperature calculation - *Fluent***. A CFD simulation is performed for a single time step for air flow and temperature in the air and wood regions. The exact length of the time step is determined in advance by the program or the user. *Matlab* pauses until the CFD simulation is complete and the application is closed via a command in the journal file.
3) **Write data - *Fluent***. The relevant mass fraction and temperature profiles are saved to data files. The case and data files are also saved. The *Fluent* application is terminated with the *exit* command.
4) **Vapour calculation - *Matlab***. *Matlab* detects the absence of the *Fluent* application and proceeds to the next part of the program. The output files from *Fluent* that were produced in Step #3 are read into *Matlab*. The mass flux at the surface of the porous region is calculated based upon the difference between the surface boundary condition and the mass fraction at the center of the first cell near the wall. Based upon the mass flux boundary condition, the relative humidity calculation is iterated until a residual of less than 10^{-7} is obtained. Once the relative humidity values are obtained for the current time step, a new mass fraction boundary condition is calculated for the surface of the porous region.
5) **Write data – *Matlab***. The boundary condition for mass fraction is written to a profile file in a format that can be input to *Fluent*. The program then verifies that the total simulation duration has not been exceeded. If it has, then the program moves to Step #6, otherwise the program will return to Step #2 and perform additional simulations.
6) **Post Processing**. The post processing stage of the model is still under development. In the present state, the relative humidity profiles at specific cross-sections are stored in a matrix for every time step. In the future, it is hoped that the convective heat and vapour coefficients will be calculated directly within the model.

6.4. APPLICATION OF THE COUPLED MODEL

The coupled heat and vapour transport model was used to simulate the experimental setup of Nabhani *et al* (2003). The experiment involved the drying of green wood samples at a variety of conditions, and the data was made available for model validation. One set of experimental conditions was reproduced with the model to study the vapour gradients within the material. A sensitivity study was performed for a number of parameters including the permeability of the wood, flow conditions, such as laminar or turbulent, and relative humidity of the air. Some of the simulation parameters had to be inferred from the description of the experiment.

6.4.1. TUNNEL EXPERIMENT

The tunnel by Nabhani *et al* (2003) was designed to measure drying rates of wood specimens. The tunnel itself consists of three layers of wood that are separated by 19 mm air layers. The middle layer of wood contains the samples being tested, and the upper and lower wood layers are in place for symmetry. The air flow over the wood varied in temperature (30, 60 or 90 °C) and velocity (1.2, 2.2 or 5.0 m/s). The vapour concentration of the air was maintained at an equilibrium moisture content of 8% for the wood selected, namely 52% relative humidity at 59.5 °C. A diagram of the experiment is shown in Figure 6.6.

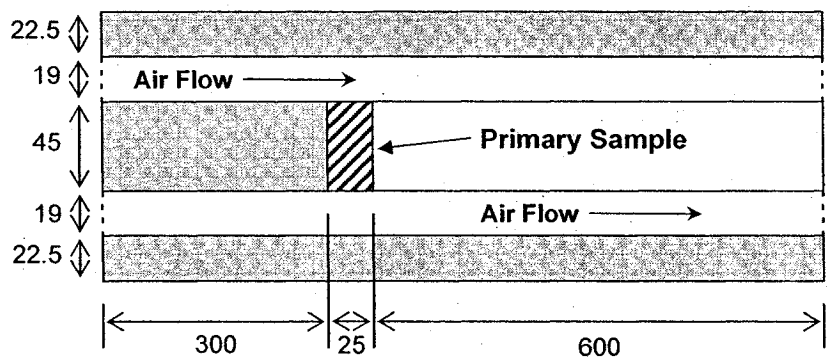

Figure 6.6. Drying tunnel experiment. All dimensions are in mm.

The computational domain for the simulation was created based upon the experiment shown in Figure 6.6. A number of assumptions were made to reproduce the experimental conditions. First, the flow and entrance conditions were not specified in the outline of the experiment. It was difficult to determine exactly how to model the inlet condition. In addition, the symmetry specimens allowed for the simplification of the

domain, which helped to reduce overall computation time. The domain and the boundary conditions that were selected to represent the experimental conditions are presented below in Figure 6.7.

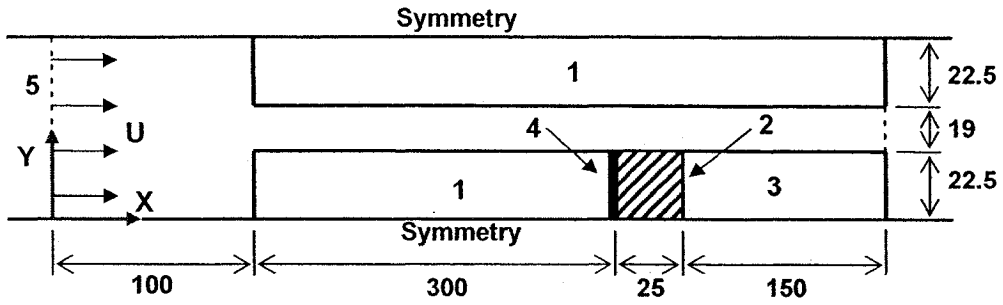

1) Symmetry specimens (wood). T_i = 332.5 K
2) Primary sample (wood). T_i = 320.7 K, X_i = experimental data profile
3) Sample (wood). T_i = 320.7 K, X'_i = (calculated outside of Fluent)
4) Rubber gasket. Insulated sample from symmetry specimen, assumed to have zero thickness. No heat or vapour flux through the gasket.
5) Velocity inlet. Constant velocity boundary condition, U = 1.4844 m/s, X' = 0.0687, T = 332.5 K.

Figure 6.7. Computational domain. All dimensions are in mm.

The computational domain was implemented in *Fluent* and the simulations were prepared in the manner described in Section 6.3. The portion of the mesh representing the primary sample (shown as #2 in Figure 6.7) is shown below in Figure 6.8. The y^+ value for the center of the first cell in the air layer was equal to approximately 1.44, indicating Low-Re modelling. The vapour diffusion model and Fluent use the same mesh dimensions and number of cells in the two directions.

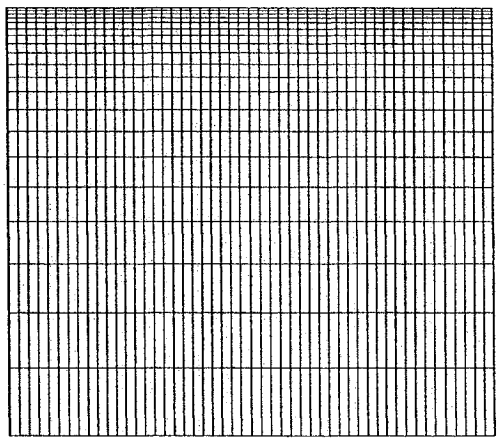

Figure 6.8. Mesh for the primary sample.

The initial moisture content gradient within the wood was adapted from experimental data from Nabhani *et al* (2003). The moisture content profile after 27 hours of drying for air at 61 °C and approximately 55% relative humidity was selected as the initial condition. The moisture content profiles before 27 hours contained very high moisture content values (up to 200%), for which the relative humidity is almost 100%. At these moisture contents, the moisture transport will be mainly in the liquid phase and the vapour diffusion approach is less accurate. The sorption isotherm is not accurate within the higher range of moisture contents, and consequently the data at 27 hours was used as the initial condition instead. The next set of experimental data was measured at 57 hours, and therefore the total simulation duration was set to be 30 hours. The initial and final moisture content gradients from the experiment are shown below in Figure 6.9.

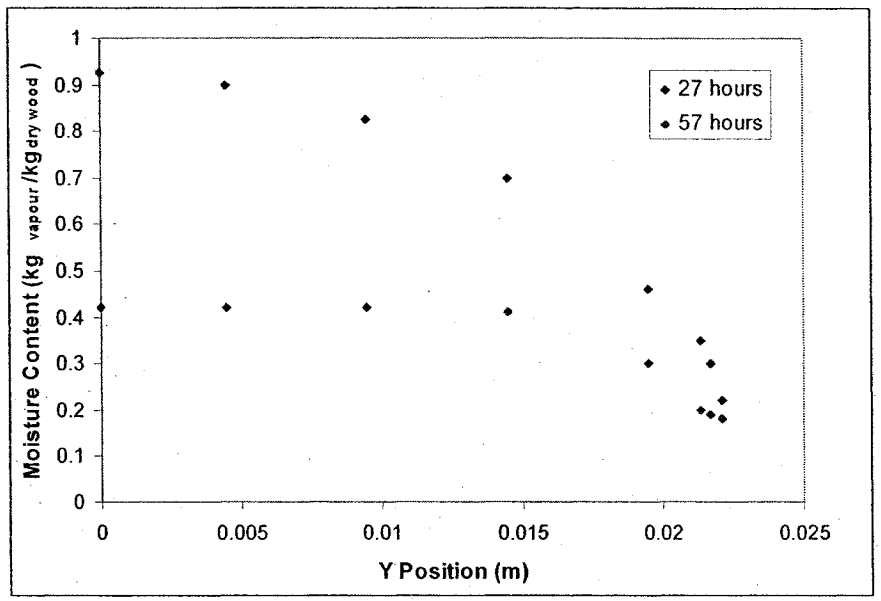

Figure 6.9. Moisture content profiles adapted from Nabhani *et al* (2003)

The equations used for the permeability and moisture content of wood are described below in terms of relative humidity, which were derived from experimental data for pine at the Katholieke Universiteit Leuven:

$$\delta = 1.474x10^{-12} \qquad \phi < 0.33$$
$$\delta = 4.372x10^{-13} e^{(3.683\phi)} \qquad \phi \geq 0.33 \tag{6.11a}$$

$$u = 0.3\left(1 - \frac{\ln(\phi)}{0.2}\right)^{-1} \tag{6.11b}$$

The 30 hour simulation duration was divided into 29 time steps that gradually increased in duration, from a minimum of 10 seconds to a maximum of two hours per time step. The flow within the cavity was modelled with several viscous models. The moisture content profiles for each time step were compared for the cross-section at the center of the primary sample, or at x = 412.5 mm in Figure 6.7.

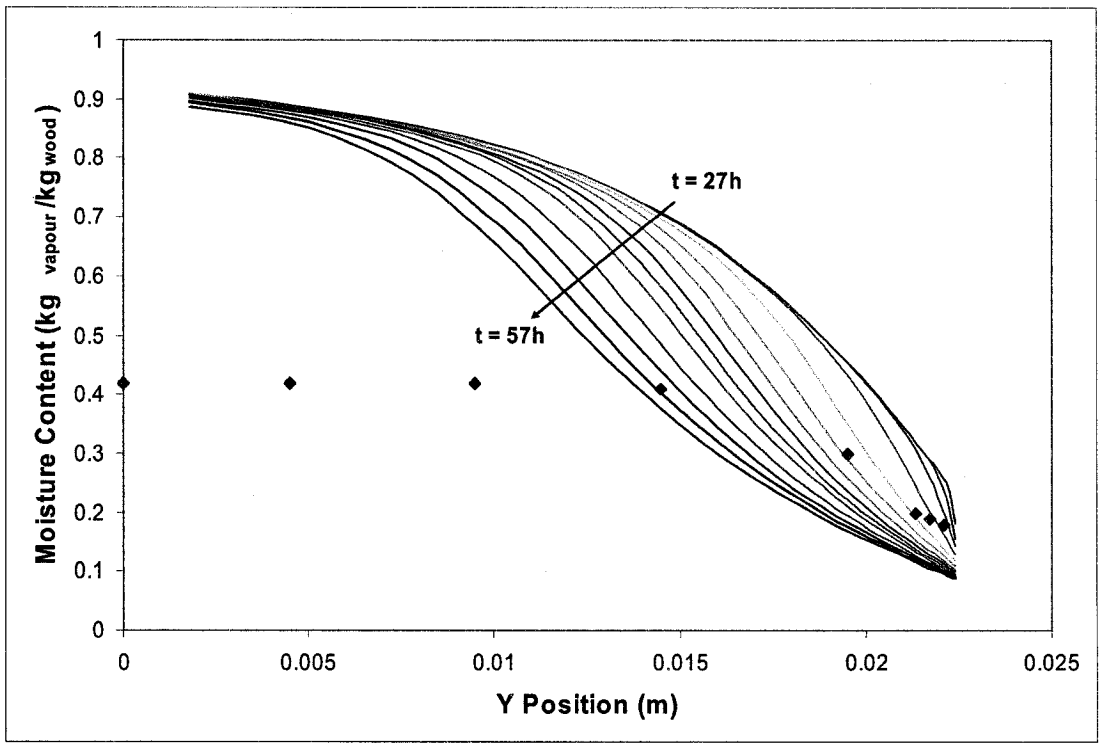

Figure 6.10. Moisture content profiles

Figure 6.10 illustrates the moisture content profiles after each time step, compared with the experimental data points recorded at 57h (shown in red). Only every second time step is shown for clarity. With the adopted material properties, there was no good agreement with experimental data.

6.4.2. SENSITIVITY STUDY

A preliminary parametric study was performed to observe the impact that varying properties has on the calculated moisture content gradients. The properties that were varied include: vapour permeability of the wood, relative humidity of the air, and regime of the flow conditions. The moisture content profiles at 57 hours are compared for three sets of permeability equations, which are shown below in Figure 6.11. Note that the notation "(5)*delta" indicates that the permeability from Equation 6.11a is increased by a

factor of 5. Since the vapour permeability of wood is temperature dependent, anisotropic and variable by species, it was considered to be a likely source for error.

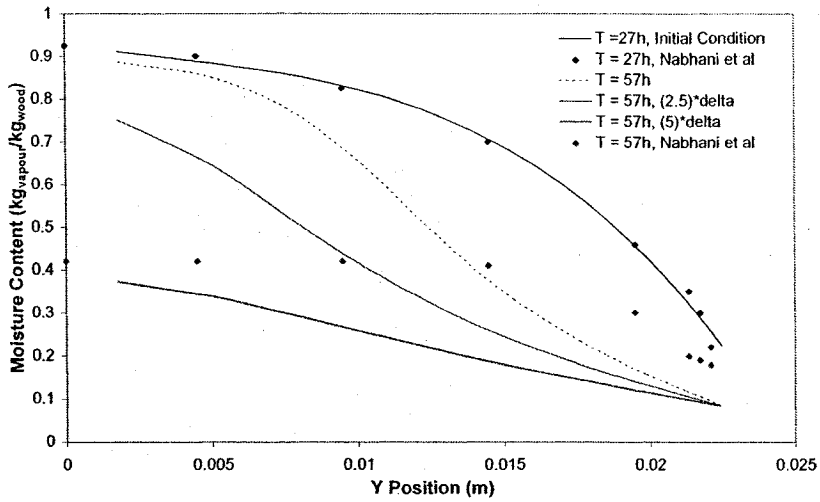

Figure 6.11. Moisture content profiles for several wood permeability values

The complete moisture content profile results for the "(2.5)*delta" and "(5)*delta" curves from Figure 6.11 are provided in Appendix D. The next parameter that was tested for influence on the moisture content results was the relative humidity of the air. The inlet air was previously stated to be at an equilibrium moisture content value of 8%, which corresponds to a relative humidity of 52% at 59.5 °C. In order to test the influence of humidity in the air, the relative humidity was varied by ±5%. The results are shown below in Figure 6.12.

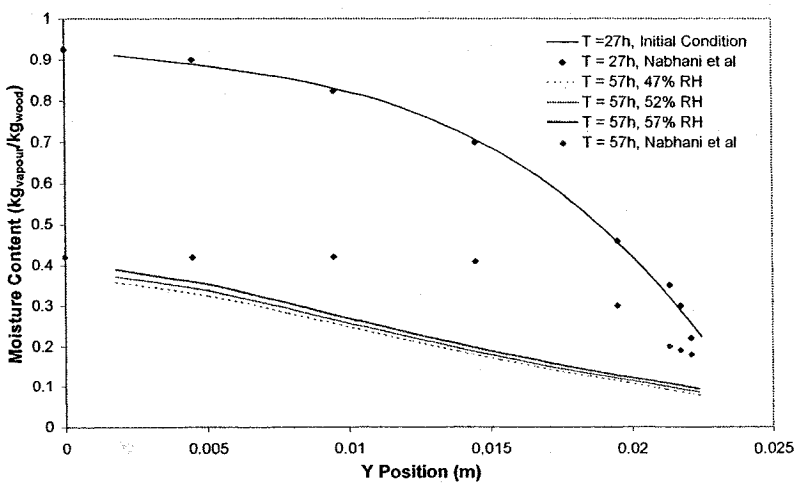

Figure 6.12. Moisture content profiles for several relative humidity values

The relative humidity of the air did not appear to have a significant impact on the moisture content profiles within the wood. Note that the permeability used for the simulations above was the "(5)*delta" equation, primarily due to the fact that it yielded the results closest to the experimental moisture content profile.

The final parameter to be varied was the viscous model selected for the simulation. The Laminar, Standard k-ε and Standard k-ω models were used to test the influence of the viscous model on the moisture content profile within the wood. The results are presented below in Figure 6.13.

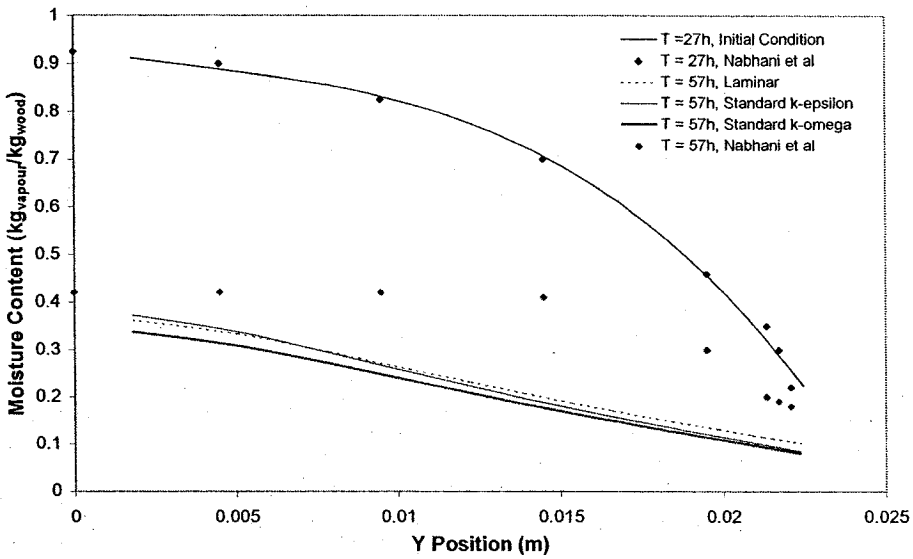

Figure 6.13. Moisture content profiles for several viscous models

The model selected for the simulation did not appear to have a large influence on the moisture content within the wood. Note that the permeability used for the simulations above was also the "(5)*delta" equation, for the same reason stated earlier.

6.4.3. Convective Heat and Vapour Transfer Coefficients

In the interest of comparing the model results to the Chilton-Colburn analogy, the convective heat and vapour coefficients were calculated for one of the cases simulated. The case selected for comparison was the "(5)*delta" simulation described in the previous section, where the permeability equations shown in Equation 6.11(a) were multiplied by a constant value of 5. The surface coefficients are compared at the cross-section at x = 0.4125 m, which corresponds to the center of the primary sample shown in

Figure 6.7. In order to calculate the convective heat transfer coefficient, Equation 2.4 is rearranged into the following form:

$$h_c = \frac{k(T_w - T_s)}{y_{ws}(T_s - T_b)} \tag{6.12}$$

where h_c is the convective heat transfer coefficient (W/m^{2}K), k is the thermal conductivity (=0.028517 W/m-K), y_{ws} is the distance between the center of the wood cell directly below the surface and the surface itself (=0.000155 m), T_w, T_s and T_b are the temperatures of the wood cell, the surface, and the bulk temperature (= 333.477 K, 333.497 K, and 334.016 K, respectively). The convective heat transfer coefficient calculated from the parameters above is equal to 7.09 W/m^{2}K.

The convective vapour transfer coefficient can be calculated from the analogy presented in Equation 2.69. If the permeability of air is taken to be 1.87x10^{-10} s and the conductivity of air is 0.028517 W/m-K, the convective vapour transfer coefficient is equal to 4.649x10^{-8} s/m.

The convective vapour transfer coefficient can also be calculated from the simulation data by using Equation 2.8 in combination with Equation 6.5. The vapour flux at the surface of the wood can be calculated with Equation 6.5, which was calculated to be 2.26x10^{-8} kg/s. The convective vapour flux can then be equated to the diffusive flux at the surface of the wood:

$$G_{conv} = h_m A(p_{vs} - p_{vb}) = 2.26x10^{-8}\ kg/s \tag{6.13}$$

where A is the cross-sectional area perpendicular to the flux direction (=0.0005 m^2), p_{vb} is the bulk vapour pressure in the air (= 10126.6 Pa), and p_{vs} is the wood surface vapour pressure (= 11881 Pa). Rearranging Equation 6.13 allows for the calculation of the convective vapour transfer coefficient, which was calculated to be 2.576x10^{-8} s/m.

The Chilton-Colburn analogy resulted in a convective vapour transfer coefficient roughly 80% larger than the calculated value.

6.5. Discussion and Conclusion

A coupling procedure that externally combines CFD simulations with an external model to calculate vapour diffusion within a porous medium was presented in this chapter. A methodology for controlling CFD remotely was combined with a vapour diffusion model developed by the author. The diffusion of moisture is solved with a control volume approach where relative humidity is the driving potential and variations of moisture content follow the desorption-sorption curve.

The solution to a number of difficult aspects related to external coupling was outlined and the methodology behind the data transfer between CFD and the external model was presented. The coupled CFD and vapour diffusion models were used to simulate the experimental set-up and conditions of a wet wood specimen exposed to constrained air flow. A sensitivity analysis using experimental conditions was performed for the coupled model. The vapour permeability of the porous medium was shown to have an important influence on the vapour diffusion process. Varying the relative humidity of the air or the viscous model selected for the simulation did appear to have a significant influence on the moisture content gradients.

The results emphasized the need for extensive and accurate experimental data required for accurate modelling of combined heat and vapour transport in an anisotropic material such as wood. A preliminary analysis of the calculated results indicates that the Chilton-Colburn analogy overestimates the convective vapour transfer coefficients for the case studied, but additional simulations are required to verify and extend this conclusion.

CHAPTER 7. CONCLUSIONS

Convective heat and mass transfer coefficients are required to simulate the hygrothermal performance of building envelope systems. The principle goal of this research was to study the feasibility and the accuracy of using Computational Fluid Dynamics to calculate convective and vapour transfer coefficients. Convective heat transfer coefficients were calculated for cases of laminar forced convection, turbulent forced convection and turbulent natural convection. The results were compared in each case with analytical, semi-empirical or empirical data for the purpose of validation. In order to determine convective vapour transfer coefficients, a coupling methodology was developed to combine CFD simulations with a vapour diffusion model developed for porous materials. A methodology for controlling CFD simulations with an external program was presented. The coupled model was tested to recreate the conditions and results of an experimental set-up and a sensitivity study was performed.

7.1. Discussion of Results

The heat transfer coefficients for laminar forced convection were calculated for low-velocity air flow between parallel plates. Two thermal boundary conditions were compared with corresponding analytical convective heat transfer coefficients. A study of reference temperatures indicated that, for the cases studied, the bulk temperature was appropriate for calculation of convective heat transfer coefficients. A grid sensitivity analysis was performed and the grid independent solution was calculated. The results indicate that CFD can calculate convective heat transfer coefficients for laminar forced convection with an error of less than 0.1%. The grid sensitivity analysis illustrated how the accuracy of results is dependent on the mesh used for the simulation.

Turbulent forced convection was simulated using seven turbulence models combined with Low-Re number modelling of the near-wall region and two turbulence models combined with wall function modelling of the near-wall region. The convective heat transfer for free turbulent flow over a flat plate was studied. The velocity and temperature profiles within the boundary layer were compared with the profiles derived from the universal law-of-the-wall theory. Results showed very good agreement between the turbulence model results and the semi-empirical equations for the laminar sublayer and log-law regions. The convective heat transfer coefficients were compared with correlations from literature and very good agreement was observed. Wall functions

were demonstrated to be inaccurate for the thermally developing regions of the simulations.

Simulations of turbulent natural convection were performed with six turbulence models. The results of the simulations were compared with experimental data. The effects of radiation and other boundary condition unknowns illustrated the need for detailed information for proper simulation of experimental set-up conditions. The calculated boundary layer velocity and temperature profiles were compared to experimental measurements with good agreement. The vertical velocity profiles exceeded the experimental results by up to 24% at certain locations, but the temperature and convective heat transfer coefficients showed a maximum error of about 8%. The discrepancy in the vertical velocity is believed to have a small effect on the convective heat transfer due to the overall low speeds shown in both the experiment and the simulations. The turbulence models with the best fit for the boundary layer velocity and temperature profiles showed the largest error (approximately 8%) when their results were used to determine the convective heat transfer coefficients. This error is found by comparing with the results of a correlation from literature. However, experimental data used to develop the correlation indicate that the correlation under-predicts the convective heat transfer coefficients by approximately 5.5% for conditions matching the case studied, which accounts for the discrepancy shown in the results.

A coupling procedure that externally combines CFD simulations with an external model to calculate vapour diffusion within a porous medium is presented. A methodology for controlling CFD remotely was combined with a vapour diffusion model developed by the author. The diffusion of moisture is solved with a control volume approach where relative humidity is the driving potential and variations of moisture content follow the desorption-sorption curve. The solution to a number of difficult aspects related to external coupling was outlined and the methodology behind the data transfer between CFD and the external model was presented. The coupled CFD and vapour diffusion models were used to simulate the experimental set-up and conditions of a wet wood specimen exposed to constrained air flow. A sensitivity analysis using experimental conditions was performed for the coupled model. The vapour permeability of the porous medium was shown to have an important influence on the vapour diffusion process. The results emphasized the need for extensive and accurate experimental data required for accurate modelling of combined heat and vapour transport. A preliminary analysis of the calculated results indicates an overestimation of the

convective vapour transfer coefficients derived by the Chilton-Colburn analogy when compared to values calculated directly from the moisture content data in the wood and air layers.

7.2. Recommendation for Future Work

The laminar and turbulent forced convection CFD simulations gave satisfactory results for convective heat transfer coefficients. Additional possible work could be to test different geometries for laminar and turbulent flows for both indoor and outdoor conditions.

The natural convection simulations have a number of possible avenues for further study. The experimental work by Tian and Karayiannis was divided into two parts: 1) velocity and temperature measurements (Tian and Karayiannis 2000a) and 2) turbulence quantities (Tian and Karayiannis 2000b). For the moment, only Part 1 was simulated. Further work could be performed in comparing turbulence intensity for experimental and simulation data for the turbulence models used in this thesis. Another course of action would be to perform further studies on the convergence issues found for natural convection simulations. It is suspected that a link could be established between mesh density, Rayleigh number and convergence related problems.

The coupled model can be improved in a number of ways. The actual model uses relative humidity as the driving potential, which makes analysis at high moisture content difficult. The model should be modified to use capillary pressure (similar to the water potential, Ψ, used, for example, by Tremblay *et al* (2000)). Equations for the moisture capacity and permeability of wood need to be implemented for a number of temperature ranges and wood species for the full range of moisture contents. With these changes, the experimental data of Nabhani *et al* (2003) could be used for a more complete validation study of the proposed externally coupled model. Such analysis would also serve to determine the exact experimental data required for complete model validation. The next step would then be to design an experiment for such validation. Careful consideration must be taken in the design of the experimental parameters: measurement of velocity profiles, measurement of the relative humidity gradient in air, control of entrance conditions, determination of all properties for the wood species used, measurement of moisture gradients in wood, measurement of temperature gradients in wood and in air, and determination of experimental parameters.

Convective vapour transfer coefficients still require some guidelines to be used in practice. At this point in time, the primary means of determining a vapour transfer coefficient is through the Chilton-Colburn analogy, which has been shown in a number of publications to be inaccurate for some conditions. In addition, hygrothermal performance simulations have been shown to be highly sensitive to convective vapour transfer coefficients (e.g. Janssen *et al* 2006, Blocken *et al* 2006).

PUBLICATIONS AND REFERENCES

Publications:

Neale, A., Derome, D. "Simulation CFD et comparaison avec données expérimentales du coefficient de transfert convectif de chaleur d'un écoulement laminaire au-dessus du bois." VII^{e} Colloque Interuniversitaire Franco-Quebécois sur la Thermique des Systèmes, Saint-Malo, 2005.

Neale, A., Derome, D., Blocken, B., Carmeliet, J., "CFD calculation of convective heat transfer coefficients and validation – Part 1: Laminar Flow." IEA, Annex 41, Kyoto, Japan, 2006.

Neale, A., Derome, D., Blocken, B., Carmeliet, J., "CFD calculation of convective heat transfer coefficients and validation – Part 2: Turbulent Flow." IEA, Annex 41, Kyoto, Japan, 2006.

Neale, A., Derome, D., Blocken, B., Carmeliet, J., "Determination of convective vapour transfer coefficients using CFD." Accepted for Performance of Exterior Envelopes of Whole Buildings X Conference, 2007.

Neale, A., Derome, D., Blocken, B., Carmeliet, J., "Determination of surface convective heat transfer coefficients by CFD." Accepted for 11th Canadian Conference on Building Science and Technology, Banff, Canada, 2007.

Neale, A., Derome, D., Blocken, B., Carmeliet, J., "CFD modelling of turbulent natural convection with validation." Accepted for 12th Symposium for Building Physics, Dresden, Germany, 2007.

Neale, A., Derome, D., Blocken, B., Carmeliet, J., "CFD modelling of turbulent natural convection with validation – Part 1: thermal and fluid flow fields." In preparation for Int. J. Heat Mass Transfer.

Neale, A., Derome, D., Blocken, B., Carmeliet, J., "CFD modelling of turbulent natural convection with validation – Part 2: turbulence quantities." In preparation for Int. J. Heat Mass Transfer.

References

Bejan, A., "Convection Heat Transfer," John Wiley & Sons, Inc., 1984.

Ben Nasrallah, S., Perré, P., "Detailed study of a model of heat and mass transfer during convective drying of porous media." Int. J. Heat Mass Transfer 31, 957-967, 1988.

Blocken, B., "Wind-driven rain on buildings," Ph.D. thesis, Leuven: K.U.Leuven., 2004.

Blocken, B., Janssen, H., Roels, S., Derome, D., Carmeliet, J., "A discussion on the formulae for heat and mass surface coefficients in building research." In preparation for Int. J. Heat Mass Transfer, 2006.

Chen, C.-J., Jaw, S.-Y., "Fundamentals of Turbulence Modeling," Taylor & Francis, 1998.

Chilton, T.H., Colburn, A.P., "Mass transfer (absorption) coefficients." Industrial and engineering chemistry 26, 1183-1187, 1934.

Churchill, S.W., Chu, H.H.S., "Correlating equations for laminar and turbulent free convection from a vertical plate." Int. J. Heat Mass Transfer 18, 1323-1329, 1975.

De Paepe, M., Willems, A., Zenner, A., "Experimental determination of the heat transfer coefficient of a plate-fin heat exchanger." Heat Transfer Engineering 26(7), 29-35, 2005.

De Paepe, M., Steeman, H-J., "Heat and mass transfer analogy, limitations and applications to buildings." IEA, Annex 41, Montreal, 2005.

Derome, D. "Moisture occurrence in roof assemblies containing moisture storing insulation and its impact on the durability of the building envelope." Ph.D. Thesis, Montreal: Concordia University, 1999.

Derome, D., Fortin, Y., Fazio, P., "Modeling of moisture behavior of wood planks in nonvented flat roofs." J. of Architectural Eng., ASCE, 9:26-40, March 2003.

Ferziger, J.H., Perić, M. "Computational Methods for Fluid Dynamics." Springer, 3rd Edition, 58-60, 2002.

Fluent 6.1 User's Guide, 2003.

Gustavsen, A., "Heat transfer in window frames with internal cavities." Ph.D. Thesis, Trondheim: Norwegian University of Science and Technology, 2001.

Hedegaard, L., Woloszyn, M., Rusaouën, G., "Moisture interactions between air and constructions modelled with CFD." IEA, Annex 41, Glasgow, 2004.

Hukka, A., Oksanen, O., "Convective mass transfer coefficient at wooden surface in jet drying of veneer." Holzforschung 53, 204-208, 1999.

Hutcheon, N.B., Handegord, G.O.P., "Building science for a cold climate." Institute for Research in Construction, NRCC, 1995.

Kreith, F., Bohn, M.S. "Principles of heat transfer." 6th Edition, Brooks/Cole, 2001.

Launder, B.E., Spalding, D.B., "Lectures in Mathematical Models of Turbulence." Academic Press, London, England, 1972.

Lewis, J.S. "Heat transfer predictions from mass transfer measurements around a single cylinder in cross flow." Int. J. Heat Mass Transfer 14, 325-329, 1971.

Lienhard IV, J.H., Lienhard V, J.H. "A Heat Transfer Textbook", Phlogiston Press, 2006.

Masmoudi, W., Prat, M., "Heat and mass transfer between a porous medium and a parallel external flow. Application to drying of capillary porous materials." Int. J. Heat Mass Transfer 34, 1975-1989, 1991.

Nabhani, M., Tremblay, C., Fortin, Y., "Experimental determination of convective heat and mass transfer coefficients during wood drying." 8th Intl. IUFRO Wood Drying Conference, 225-230, 2003.

Olutimayin, S., Simonson, C.J., "Measuring and modeling vapor boundary layer growth during transient diffusion heat and moisture transfer in cellulose insulation." Int. J. Heat Mass Transfer 48, 3319-3330, 2005.

Saelens, D., "Energy performance assessment of single story multiple-skin facades," Ph.D. dissertation, Leuven: K.U.Leuven, 2002.

Salin, J-G. "External heat and mass transfer – some remarks." 8th Int. IUFRO Wood Drying Conference, 343-348, 2003.

Schetz, J.A., "Boundary Layer Analysis." Prentice Hall, 1993.

Schlichting, H., "Boundary-Layer Theory," McGraw-Hill, 7th Edition, 1987.

Spalding, D.B., "A single formula for the law of the wall," J. Appl. Mech., Vol 28, 1961, pp. 455-457.

Tian, Y.S., Karayiannis, T.G., "Low turbulence natural convection in an air filled square cavity, Part 1: the thermal and fluid flow fields." Int. J. of Heat and Mass Transfer 43, 849-866, 2000a.

Tian, Y.S., Karayiannis, T.G., "Low turbulence natural convection in an air filled square cavity, Part 2: the turbulence quantities." Int. J. of Heat Mass Transfer 43, 867-884, 2000b.

Tremblay, C., Cloutier, A., Fortin, Y., "Experimental determination of the convective heat and mass transfer coefficients for wood drying." Wood Science and Technology 34, 253-276, 2000.

Trujillo, F.J., Lovatt, S.J., Harris, M.B., Willix, J., Pham, Q.T., "CFD modeling of the heat and mass transfer process during the evaporation of water from a circular cylinder." 3rd Int. Conference on CFD in the Minerals and Process Ind., CSIRO, 99-104, 2003.

Wadsö, L., "Surface mass transfer coefficients for wood." Drying Technology 11, 1227-1249, 1993.

White, F.M., "A new integral method for analyzing the turbulent boundary layer with arbitrary pressure gradient," J. Basic Engr., 91: 371-378, 1969.

APPENDIX A: SIMULATION PARAMETERS

Sample laminar forced convection simulation parameters:

Model	Settings
Space	2D
Time	Steady
Viscous	Laminar
Heat Transfer	Enabled
Solidification and Melting	Disabled
Radiation	None
Species Transport	Disabled
Coupled Dispersed Phase	Disabled
Pollutants	Disabled
Soot	Disabled

Equation	Solved
Flow	yes
Energy	yes

Numerics	Enabled
Absolute Velocity Formulation	yes

Relaxation:

Variable	Relaxation Factor
Pressure	0.3
Density	1
Body Forces	1
Momentum	0.7
Energy	1

Solver Variable	Termination Type	Residual Criterion	Reduction Tolerance
Pressure	V-Cycle	0.1	
X-Momentum	Flexible	0.1	0.7
Y-Momentum	Flexible	0.1	0.7
Energy	Flexible	0.1	0.7

Discretization Scheme

Variable	Scheme
Pressure	Standard
Pressure-Velocity Coupling	SIMPLE
Momentum	First Order Upwind
Energy	First Order Upwind

Solution Limits

Quantity	Limit
Minimum Absolute Pressure	1
Maximum Absolute Pressure	5000000
Minimum Temperature	1
Maximum Temperature	5000

Sample turbulent forced convection simulation parameters (k-ε Standard Model):

Model	Settings
Space	2D
Time	Steady
Viscous	Standard k-epsilon turbulence model
Wall Treatment	Standard Wall Functions
Heat Transfer	Enabled
Solidification and Melting	Disabled
Radiation	None
Species Transport	Disabled
Coupled Dispersed Phase	Disabled
Pollutants	Disabled
Soot	Disabled

Equation	Solved
Flow	yes
Turbulence	yes
Energy	yes

Numerics	Enabled
Absolute Velocity Formulation	yes

Relaxation:

Variable	Relaxation Factor
Pressure	0.3
Density	1
Body Forces	1
Momentum	0.7
Turbulent kinetic energy	0.8
Turbulent dissipation rate	0.8
Turbulent viscosity	1
Energy	1

Solver Variable	Termination Type	Residual Criterion	Reduction Tolerance
Pressure	V-Cycle	0.1	
X-Momentum	Flexible	0.1	0.7
Y-Momentum	Flexible	0.1	0.7
Turbulence Kinetic Energy	Flexible	0.1	0.7
Turbulence Dissipation Rate	Flexible	0.1	0.7
Energy	Flexible	0.1	0.7

Discretization Scheme

Variable	Scheme
Pressure	Standard
Pressure-Velocity Coupling	SIMPLE
Momentum	First Order Upwind
Turbulence Kinetic Energy	First Order Upwind
Turbulence Dissipation Rate	First Order Upwind
Energy	First Order Upwind

Solution Limits

Quantity	Limit
Minimum Absolute Pressure	1
Maximum Absolute Pressure	5000000
Minimum Temperature	1
Maximum Temperature	5000
Minimum Turb. Kinetic Energy	1e-14
Minimum Turb. Dissipation Rate	1e-20
Maximum Turb. Viscosity Ratio	100000

Sample turbulent natural convection simulation parameters (k-ε Standard Model):

Model	Settings
Space	2D
Time	Steady
Viscous	Standard k-epsilon turbulence model
Wall Treatment	Enhanced wall treatment
Heat Transfer	Enabled
Solidification and Melting	Disabled
Radiation	None
Species Transport	Disabled
Coupled Dispersed Phase	Disabled
Pollutants	Disabled
Soot	Disabled

Equation	Solved
Flow	yes
Turbulence	yes
Energy	yes

Numerics	Enabled
Absolute Velocity Formulation	yes

Relaxation:

Variable	Relaxation Factor
Pressure	0.3
Density	1
Body Forces	1
Momentum	0.7
Turbulent kinetic energy	0.8
Turbulent dissipation rate	0.8
Turbulent viscosity	1
Energy	1

Solver Variable	Termination Type	Residual Criterion	Reduction Tolerance
Pressure	V-Cycle	0.1	
X-Momentum	Flexible	0.1	0.7
Y-Momentum	Flexible	0.1	0.7
Turbulence Kinetic Energy	Flexible	0.1	0.7
Turbulence Dissipation Rate	Flexible	0.1	0.7
Energy	Flexible	0.1	0.7

Discretization Scheme

Variable	Scheme
Pressure	Body Force Weighted
Pressure-Velocity Coupling	SIMPLE
Density	First Order Upwind
Momentum	First Order Upwind
Turbulence Kinetic Energy	First Order Upwind
Turbulence Dissipation Rate	First Order Upwind
Energy	First Order Upwind

Solution Limits

Quantity	Limit
Minimum Absolute Pressure	1
Maximum Absolute Pressure	5000000
Minimum Temperature	1
Maximum Temperature	5000
Minimum Turb. Kinetic Energy	1e-14
Minimum Turb. Dissipation Rate	1e-20
Maximum Turb. Viscosity Ratio	100000

APPENDIX B: NATURAL CONVECTION RESULTS

Experimental Data from Tian and Karayiannis (2000):

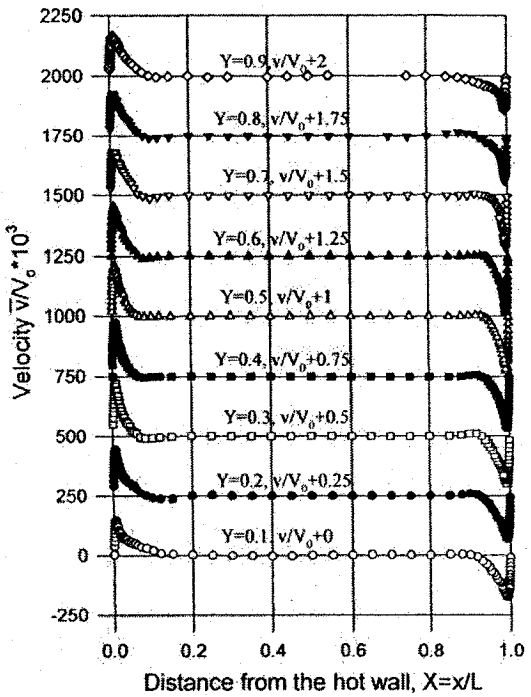

(a) Vertical velocity

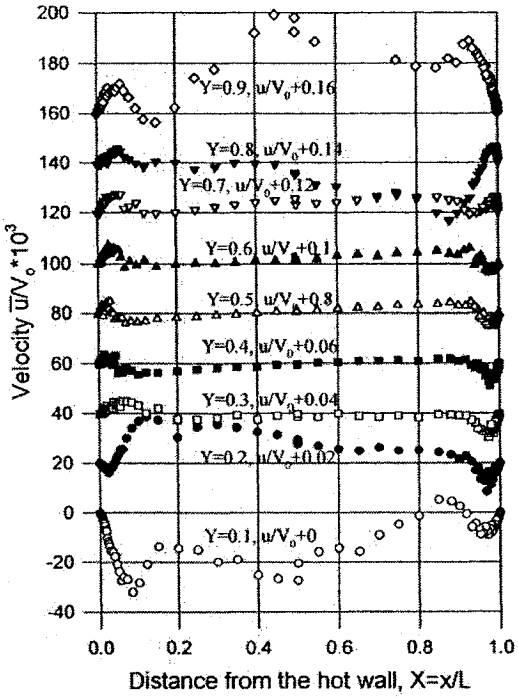

(b) Horizontal velocity

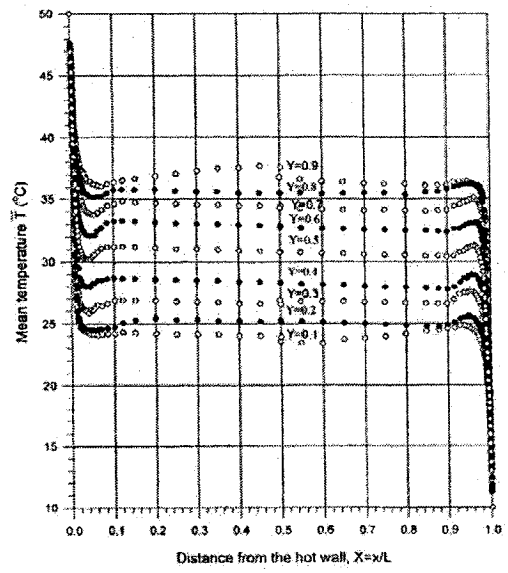

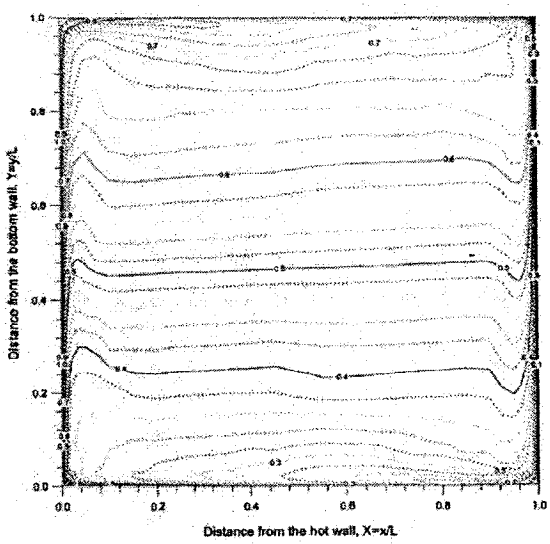

Simulation Data

Standard k-ε model:

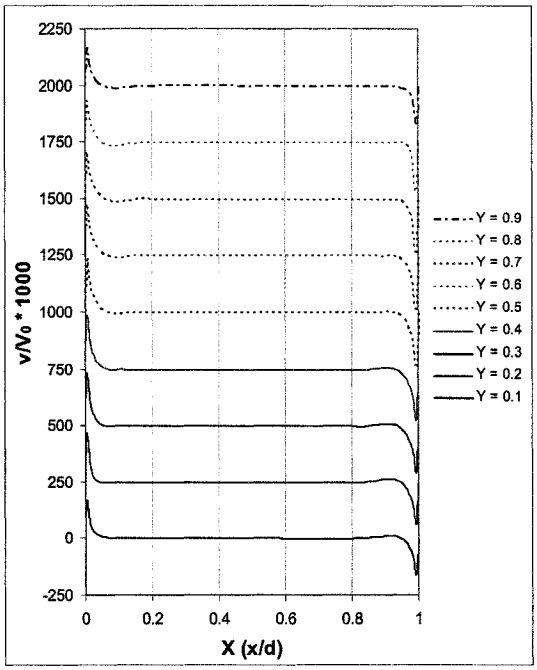

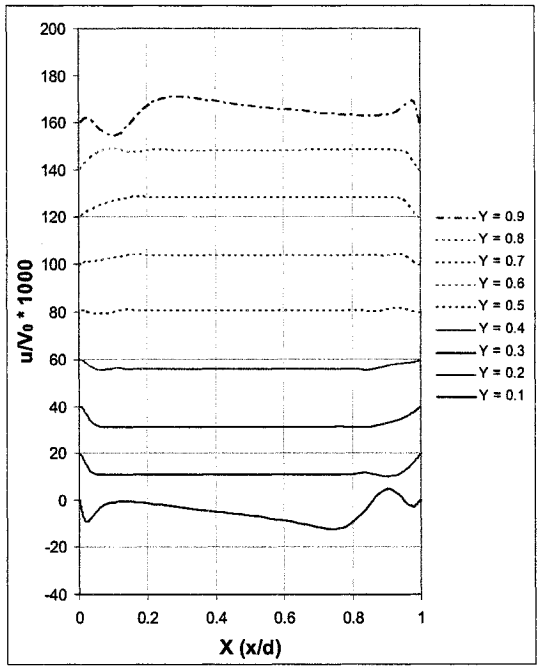

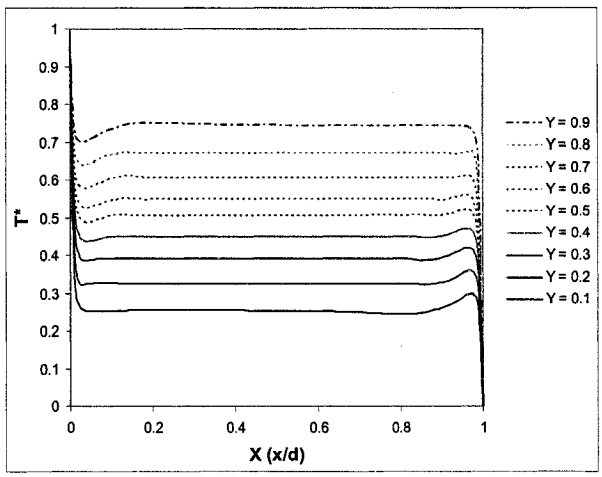

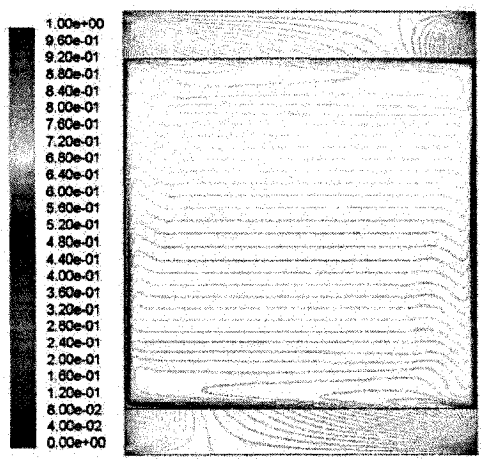

Realizable k-ε model:

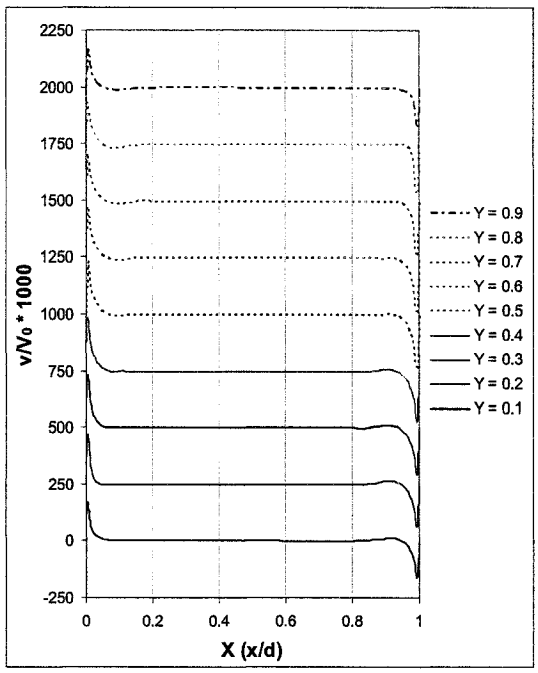

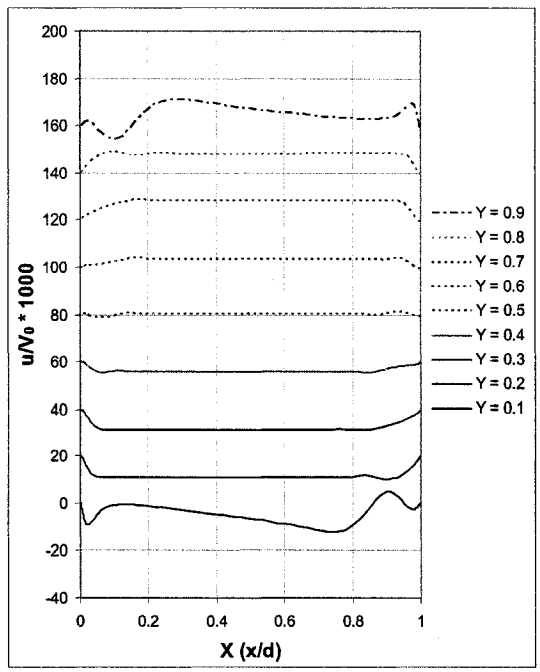

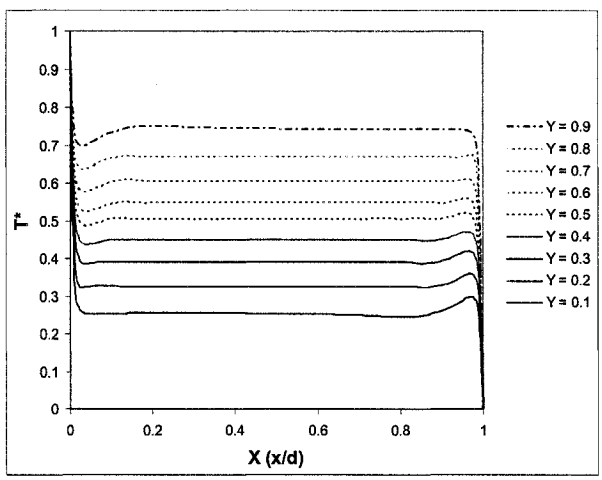

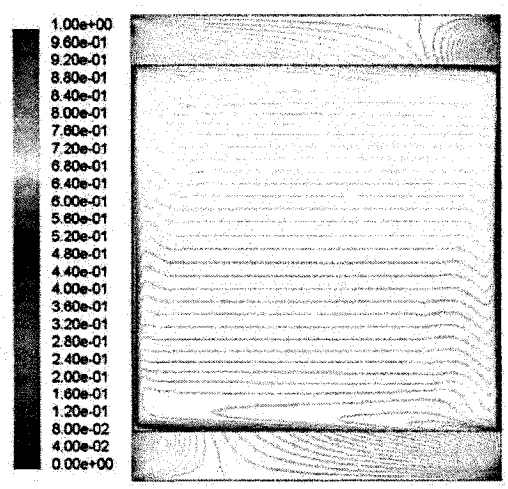

RNG k-ε model:

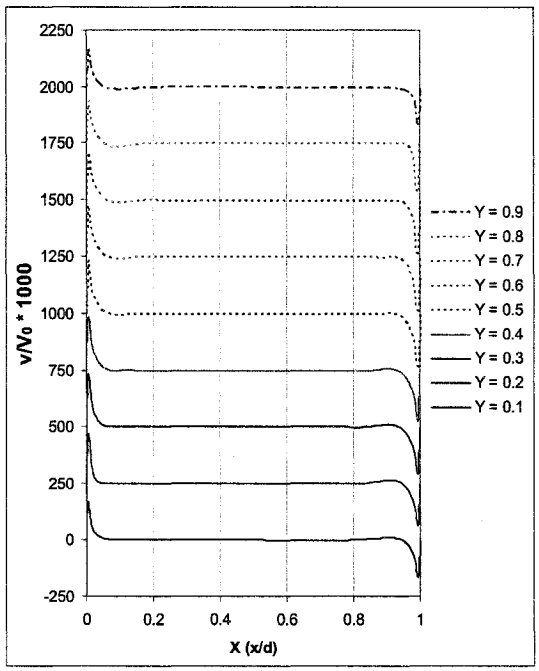

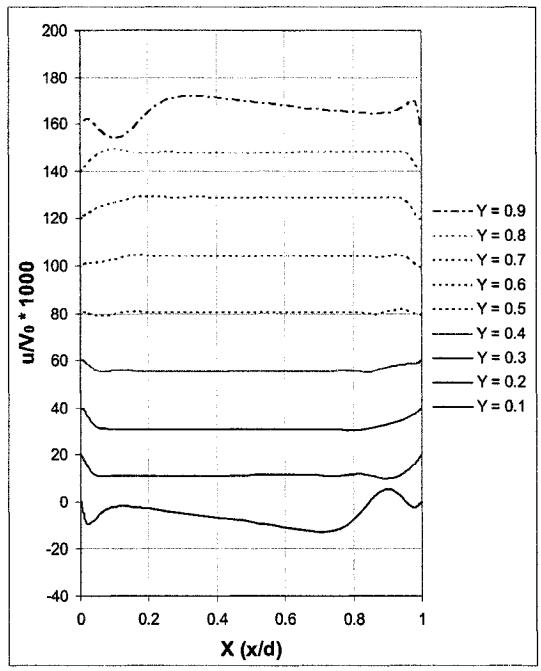

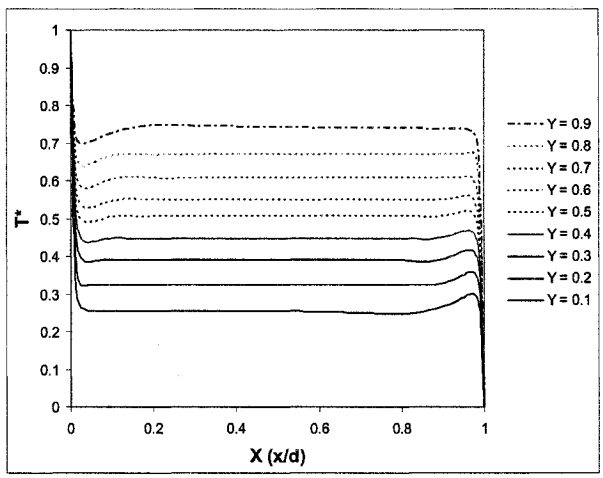

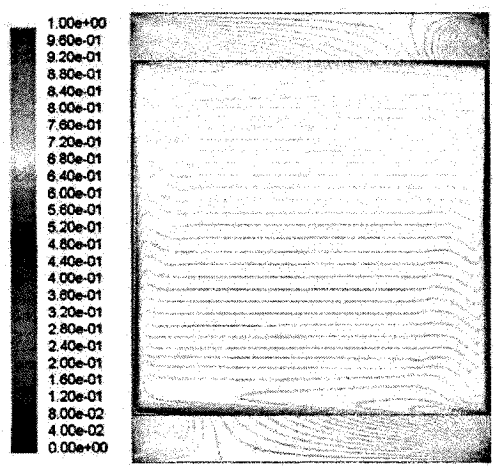

Standard k-ω model:

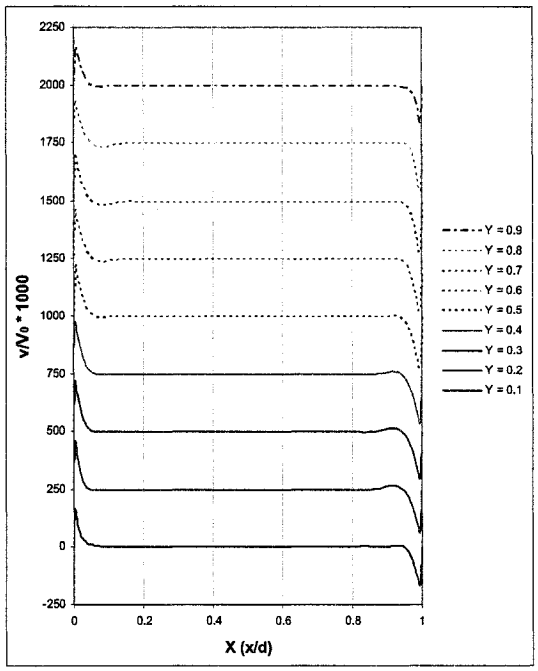

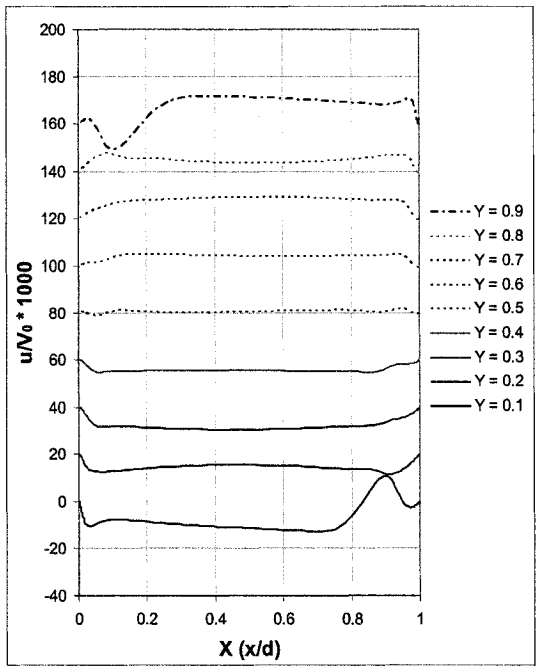

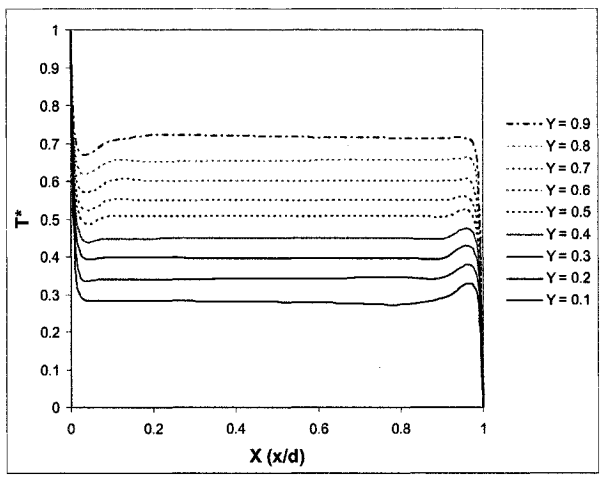

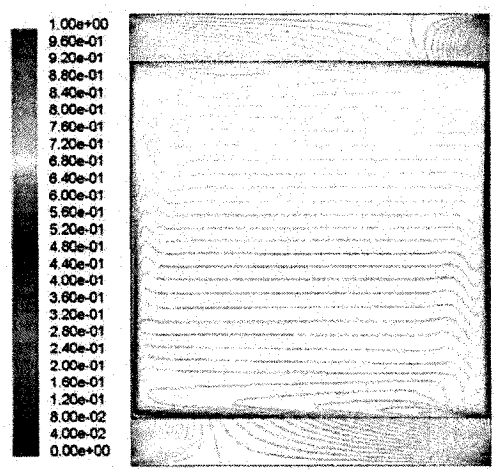

SST k-ω model:

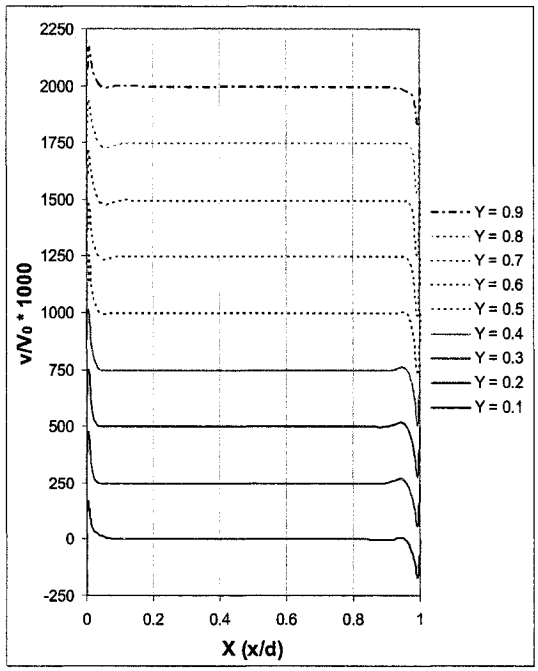

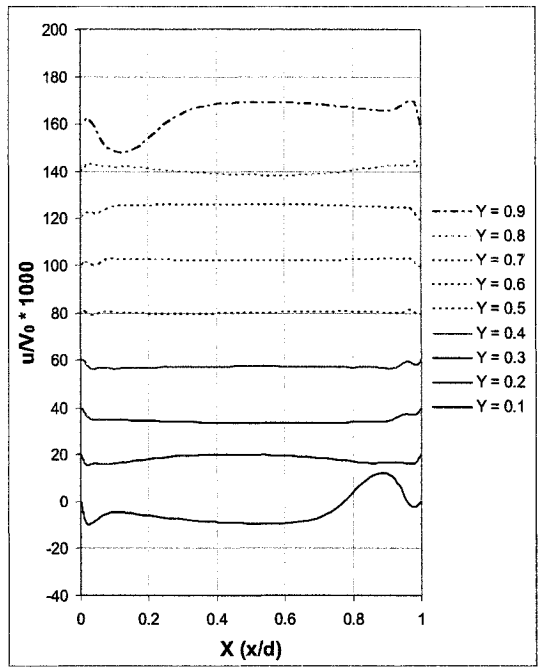

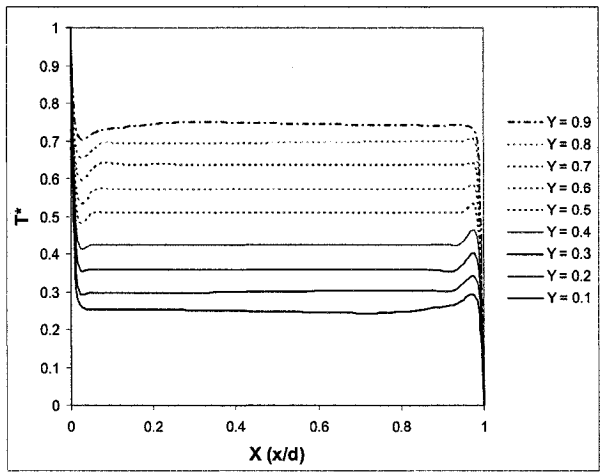

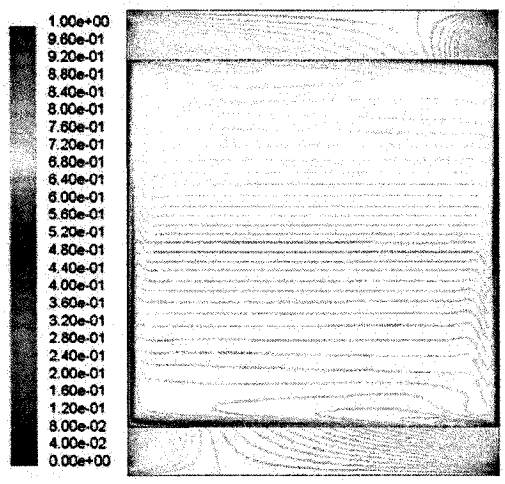

Spalart-Allmaras model

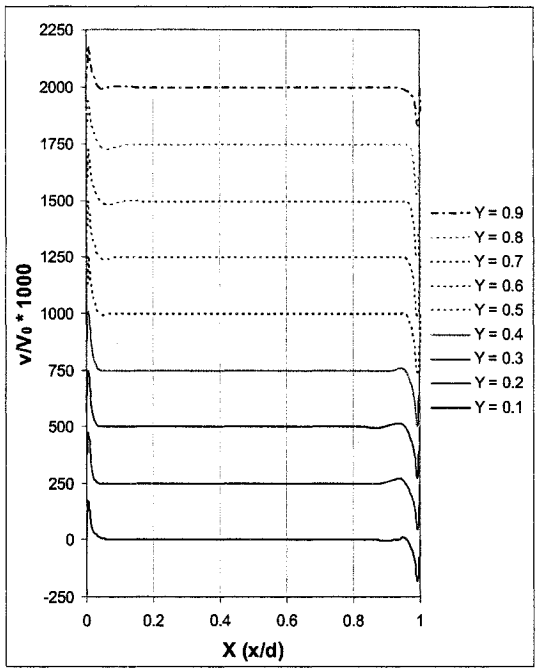

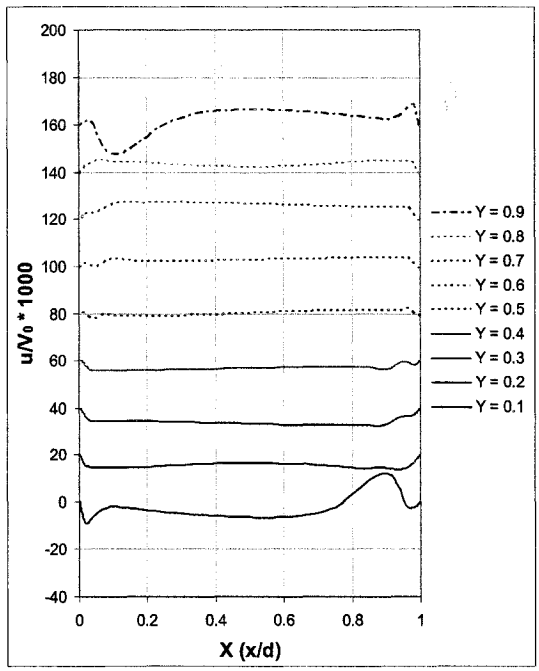

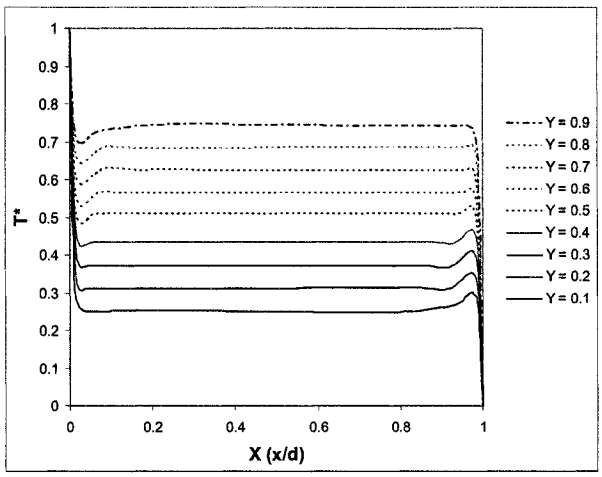

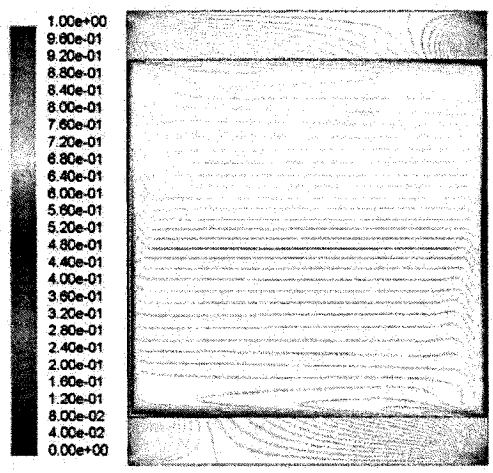

APPENDIX C: VAPOUR DIFFUSION EQUATIONS

$$Q_{(i-1,j)\to(i,j)} = \frac{b_j\left(\phi_{i-1,j}^{t+\Delta t} - \phi_{i,j}^{t+\Delta t}\right)}{\left(\dfrac{0.5a_{i-1}}{\delta_{i-1,j}\left\{\phi_{i-1,j}^{t+\Delta t}\right\}p_{VSAT}\left\{\theta_{i-1,j}^{t+\Delta t}\right\}} + \dfrac{0.5a_i}{\delta_{i,j}\left\{\phi_{i,j}^{t+\Delta t}\right\}p_{VSAT}\left\{\theta_{i,j}^{t+\Delta t}\right\}}\right)} + \frac{b_j\left(\theta_{i-1,j}^{t+\Delta t} - \theta_{i,j}^{t+\Delta t}\right)}{\left(\dfrac{0.5a_{i-1}}{\delta_{i-1,j}\left\{\phi_{i-1,j}^{t+\Delta t}\right\}\phi_{i-1,j}^{t+\Delta t}\dfrac{\partial p_{VSAT}\left\{\theta_{i-1,j}^{t+\Delta t}\right\}}{\partial\theta}} + \dfrac{0.5a_i}{\delta_{i,j}\left\{\phi_{i,j}^{t+\Delta t}\right\}\phi_{i,j}^{t+\Delta t}\dfrac{\partial p_{VSAT}\left\{\theta_{i,j}^{t+\Delta t}\right\}}{\partial\theta}}\right)}$$

$$Q_{(i+1,j)\to(i,j)} = \frac{b_j\left(\phi_{i+1,j}^{t+\Delta t} - \phi_{i,j}^{t+\Delta t}\right)}{\left(\dfrac{0.5a_{i+1}}{\delta_{i+1,j}\left\{\phi_{i+1,j}^{t+\Delta t}\right\}p_{VSAT}\left\{\theta_{i+1,j}^{t+\Delta t}\right\}} + \dfrac{0.5a_i}{\delta_{i,j}\left\{\phi_{i,j}^{t+\Delta t}\right\}p_{VSAT}\left\{\theta_{i,j}^{t+\Delta t}\right\}}\right)} + \frac{b_j\left(\theta_{i+1,j}^{t+\Delta t} - \theta_{i,j}^{t+\Delta t}\right)}{\left(\dfrac{0.5a_{i+1}}{\delta_{i+1,j}\left\{\phi_{i+1,j}^{t+\Delta t}\right\}\phi_{i+1,j}^{t+\Delta t}\dfrac{\partial p_{VSAT}\left\{\theta_{i+1,j}^{t+\Delta t}\right\}}{\partial\theta}} + \dfrac{0.5a_i}{\delta_{i,j}\left\{\phi_{i,j}^{t+\Delta t}\right\}\phi_{i,j}^{t+\Delta t}\dfrac{\partial p_{VSAT}\left\{\theta_{i,j}^{t+\Delta t}\right\}}{\partial\theta}}\right)}$$

$$Q_{(i,j-1)\to(i,j)} = \frac{a_j\left(\phi_{i,j-1}^{t+\Delta t} - \phi_{i,j}^{t+\Delta t}\right)}{\left(\dfrac{0.5b_{j-1}}{\delta_{i,j-1}\left\{\phi_{i,j-1}^{t+\Delta t}\right\}p_{VSAT}\left\{\theta_{i,j-1}^{t+\Delta t}\right\}} + \dfrac{0.5b_j}{\delta_{i,j}\left\{\phi_{i,j}^{t+\Delta t}\right\}p_{VSAT}\left\{\theta_{i,j}^{t+\Delta t}\right\}}\right)} + \frac{a_j\left(\theta_{i,j-1}^{t+\Delta t} - \theta_{i,j}^{t+\Delta t}\right)}{\left(\dfrac{0.5b_{j-1}}{\delta_{i,j-1}\left\{\phi_{i,j-1}^{t+\Delta t}\right\}\phi_{i,j-1}^{t+\Delta t}\dfrac{\partial p_{VSAT}\left\{\theta_{i,j-1}^{t+\Delta t}\right\}}{\partial\theta}} + \dfrac{0.5b_j}{\delta_{i,j}\left\{\phi_{i,j}^{t+\Delta t}\right\}\phi_{i,j}^{t+\Delta t}\dfrac{\partial p_{VSAT}\left\{\theta_{i,j}^{t+\Delta t}\right\}}{\partial\theta}}\right)}$$

$$Q_{(i,j+1)\to(i,j)} = \frac{a_j\left(\phi_{i,j+1}^{t+\Delta t} - \phi_{i,j}^{t+\Delta t}\right)}{\left(\dfrac{0.5b_{j+1}}{\delta_{i,j+1}\left\{\phi_{i,j+1}^{t+\Delta t}\right\}p_{VSAT}\left\{\theta_{i,j+1}^{t+\Delta t}\right\}} + \dfrac{0.5b_j}{\delta_{i,j}\left\{\phi_{i,j}^{t+\Delta t}\right\}p_{VSAT}\left\{\theta_{i,j}^{t+\Delta t}\right\}}\right)} + \frac{a_j\left(\theta_{i,j+1}^{t+\Delta t} - \theta_{i,j}^{t+\Delta t}\right)}{\left(\dfrac{0.5b_{j+1}}{\delta_{i,j+1}\left\{\phi_{i,j+1}^{t+\Delta t}\right\}\phi_{i,j+1}^{t+\Delta t}\dfrac{\partial p_{VSAT}\left\{\theta_{i,j+1}^{t+\Delta t}\right\}}{\partial\theta}} + \dfrac{0.5b_j}{\delta_{i,j}\left\{\phi_{i,j}^{t+\Delta t}\right\}\phi_{i,j}^{t+\Delta t}\dfrac{\partial p_{VSAT}\left\{\theta_{i,j}^{t+\Delta t}\right\}}{\partial\theta}}\right)}$$

$$C_1 = \frac{b_j}{\left(\dfrac{0.5a_{i-1}}{\delta_{i-1,j}\left\{\phi_{i-1,j}^{t+\Delta t}\right\}p_{VSAT}\left\{\theta_{i-1,j}^{t+\Delta t}\right\}} + \dfrac{0.5a_i}{\delta_{i,j}\left\{\phi_{i,j}^{t+\Delta t}\right\}p_{VSAT}\left\{\theta_{i,j}^{t+\Delta t}\right\}}\right)}$$

$$C_3 = \frac{a_i}{\left(\dfrac{0.5b_{j-1}}{\delta_{i,j-1}\left\{\phi_{i,j-1}^{t+\Delta t}\right\}p_{VSAT}\left\{\theta_{i,j-1}^{t+\Delta t}\right\}} + \dfrac{0.5b_j}{\delta_{i,j}\left\{\phi_{i,j}^{t+\Delta t}\right\}p_{VSAT}\left\{\theta_{i,j}^{t+\Delta t}\right\}}\right)}$$

$$C_2 = \frac{b_j}{\left(\dfrac{0.5a_{i+1}}{\delta_{i+1,j}\left\{\phi_{i+1,j}^{t+\Delta t}\right\}p_{VSAT}\left\{\theta_{i+1,j}^{t+\Delta t}\right\}} + \dfrac{0.5a_i}{\delta_{i,j}\left\{\phi_{i,j}^{t+\Delta t}\right\}p_{VSAT}\left\{\theta_{i,j}^{t+\Delta t}\right\}}\right)}$$

$$C_4 = \frac{a_i}{\left(\dfrac{0.5b_{j+1}}{\delta_{i,j+1}\left\{\phi_{i,j+1}^{t+\Delta t}\right\}p_{VSAT}\left\{\theta_{i,j+1}^{t+\Delta t}\right\}} + \dfrac{0.5b_j}{\delta_{i,j}\left\{\phi_{i,j}^{t+\Delta t}\right\}p_{VSAT}\left\{\theta_{i,j}^{t+\Delta t}\right\}}\right)}$$

$$C_5 = -(C_1 + C_2 + C_3 + C_4) - \frac{\xi}{\Delta t}$$

$$C_6 = -\frac{b_j\left(\theta_{i-1,j}^{t+\Delta t} - \theta_{i,j}^{t+\Delta t}\right)}{\left(\frac{0.5a_{i-1}}{\delta_{i-1,j}\left\{\phi_{i-1,j}^{t+\Delta t}\right\}\phi_{i-1,j}^{t+\Delta t}\frac{\partial p_{VSAT}\left\{\theta_{i-1,j}^{t+\Delta t}\right\}}{\partial\theta}} + \frac{0.5a_i}{\delta_{i,j}\left\{\phi_{i,j}^{t+\Delta t}\right\}\phi_{i,j}^{t+\Delta t}\frac{\partial p_{VSAT}\left\{\theta_{i,j}^{t+\Delta t}\right\}}{\partial\theta}}\right)}$$

$$-\frac{b_j\left(\theta_{i+1,j}^{t+\Delta t} - \theta_{i,j}^{t+\Delta t}\right)}{\left(\frac{0.5a_{i+1}}{\delta_{i+1,j}\left\{\phi_{i+1,j}^{t+\Delta t}\right\}\phi_{i+1,j}^{t+\Delta t}\frac{\partial p_{VSAT}\left\{\theta_{i+1,j}^{t+\Delta t}\right\}}{\partial\theta}} + \frac{0.5a_i}{\delta_{i,j}\left\{\phi_{i,j}^{t+\Delta t}\right\}\phi_{i,j}^{t+\Delta t}\frac{\partial p_{VSAT}\left\{\theta_{i,j}^{t+\Delta t}\right\}}{\partial\theta}}\right)}$$

$$-\frac{a_j\left(\theta_{i,j-1}^{t+\Delta t} - \theta_{i,j}^{t+\Delta t}\right)}{\left(\frac{0.5b_{j-1}}{\delta_{i,j-1}\left\{\phi_{i,j-1}^{t+\Delta t}\right\}\phi_{i,j-1}^{t+\Delta t}\frac{\partial p_{VSAT}\left\{\theta_{i,j-1}^{t+\Delta t}\right\}}{\partial\theta}} + \frac{0.5b_j}{\delta_{i,j}\left\{\phi_{i,j}^{t+\Delta t}\right\}\phi_{i,j}^{t+\Delta t}\frac{\partial p_{VSAT}\left\{\theta_{i,j}^{t+\Delta t}\right\}}{\partial\theta}}\right)}$$

$$-\frac{a_j\left(\theta_{i,j+1}^{t+\Delta t} - \theta_{i,j}^{t+\Delta t}\right)}{\left(\frac{0.5b_{j+1}}{\delta_{i,j+1}\left\{\phi_{i,j+1}^{t+\Delta t}\right\}\phi_{i,j+1}^{t+\Delta t}\frac{\partial p_{VSAT}\left\{\theta_{i,j+1}^{t+\Delta t}\right\}}{\partial\theta}} + \frac{0.5b_j}{\delta_{i,j}\left\{\phi_{i,j}^{t+\Delta t}\right\}\phi_{i,j}^{t+\Delta t}\frac{\partial p_{VSAT}\left\{\theta_{i,j}^{t+\Delta t}\right\}}{\partial\theta}}\right)} - \xi\frac{\phi_{i,j}^{t}}{\Delta t}$$

APPENDIX D: MOISTURE CONTENT PROFILES